Transport spectroscopy on novel quantum materials

A thesis submitted for the partial fulfilment of the degree of

Doctor of Philosophy

by

Suman Kamboj

Department of Physical Sciences

Indian Institute of Science Education and Research

Mohali

October, 2020

Dedicated to

my parents

Declaration

The work presented in this thesis has been carried out by me under the guidance of Dr. Goutam Sheet at Indian Institute of Science Education and Research (IISER) Mohali. This work has not been submitted in part or in full for a degree, a diploma, or a fellowship to any other university or institute. Whenever contributions of others are involved, every effort is made to indicate this clearly, with due acknowledgment of collaborative research and discussions. This thesis is a bonafide record of original work done by me and all sources listed within have been detailed in the bibliography.

Date:

Place :

Suman Kamboj

In my capacity as the supervisor of the candidate's thesis work, I certify that the above statements by the candidate are true to the best of my knowledge.

Dr. Goutam Sheet (Supervisor)

Acknowledgement

The work presented in this thesis would never have been possible without any help of my close association with many people. I take this opportunity to extend my sincere gratitude and appreciation to all those who made this Ph.D. thesis possible. First and foremost, I would like to thank my supervisor, Dr. Goutam Sheet, for the guidance, encouragement and advice, he has provided throughout my time as his student. His valuable suggestions, comments and guidance encourage me to learn more day by day. I have been extremely lucky to have a supervisor who cared so much about my work, and who responded to my questions and queries so promptly. He is my mentor and a better advisor for my doctorate study beyond the imagination. His deep insights helped me at various stages of my research. I am also indebted towards his generosity, selfless support and especially for the excellent example that he has provided to me for the last five years.

Besides my advisor, I would like to thank Rajeswari Di, Shilpa di, Gayen da, not only for their insightful comments and encouragement, but also for the hard question which incented me to widen my research from various perspectives.

I would like to thank my doctoral committee members Dr. Yogesh Singh and Dr. Sanjeev Kumar for their invaluable help and regular feedback during my PhD tenure. I thank my collaborators Dr. Satyabrata Patnaik and Vishal Maurya from Jawahar lal Nehru University (JNU) Delhi; Dr. Prabhat Mandal, Susmita Roy from Saha Institute of Nuclear Physics (SINP) Kolkata; Dr. Ravi Prakash Singh, Manasi Mandal, Sourav Marik from Indian Institute of Science Education and Research (IISER), Bhopal for providing high quality samples during scanning tunneling microscopy and point-contact spectroscopy measurements. My sincere thank to Prof. Tanmoy Das, Paratha Sarathi Rana from Indian Intitute of Science (IISc), Bangalore; Dr. Mukul Kabir, Deepak K. Roy from Indian Institute of Science Education and Research (IISER), Pune for providing theoretical explanations to my research ideas. I couldn't have completed my PhD work without the

help and support from the staff of the physics department at IISER Mohali.

I would like to thank all my teachers from high school to graduate school who helped me to reach this phase of my life.

I would always remember my fellow labmates for the fun-time we spent together, sleepless nights that gave us the courage to do lab work and for stimulating the discussions. I would also like to thank my friends Leena, Aslam, Shekhar, Anshu, Ritesh, Mohammad Balal, Soumya Datta, Saumyadip, Sandeep, Aastha, Aashi, Mamta, Shelender, Sham, Anzar, Amit, Ashwini, Kavita, Shama, Deepti, Monika, Lalit, Shivam, Neetu, Aleena, Anmol, Mona. I would like to thank Avtar Bhaiya, Ranjana and Veerpal for constantly supplying liq. helium and other required things on time. I am also grateful to Kanika, Noor, Sunil for making this journey a memorable one.

A Heartfelt Thanks to Rajeswari Di and Aastha for all help and support. Your helping hand paved a way to the completion of this thesis.

I would like to thank my family, my parents, brother for their unconditional support, encouragement and love, and without which I would not have come this far. I can't thank them enough for everything that they have done for making this work a possible one. Special thanks to the new additions to my family, Rohit, my husband as well as his wonderful family who all have been supportive and caring during this period.

List of Publications:

1. Generation of strain-induced pseudo-magnetic field in a doped type-II Weyl semimetal, **Suman Kamboj**, Partha Sarathi Rana, Anshu Sirohi, Aastha Vasdev, Manasi Mandal, Sourav Marik, Ravi Prakash Singh, Tanmoy Das and Goutam Sheet. *Physical Review B* 100, 115105 (2019).

2. Temperature dependent transport spin-polarization in the low Curie temperature complex itinerant ferromagnet $EuTi_{1-x}Nb_xO_3$, **Suman Kamboj**, Deepak K. Roy, Susmita Roy, Rajeswari Roy Chowdhury, Prabhat Mandal, Mukul Kabir and Goutam Sheet. *Journal of Physics: Condensed Matter* 31 415601 (2019).

3. Suppression of transport spin-polarization of surface states with the emergence of ferromagnetism in Mn-doped Bi_2Se_3, **Suman Kamboj**, Shekhar Das, Anshu Sirohi, Rajeswari Roy Chowdhury, Sirshendu Gayen, Vishal K. Maurya, Satyabrata Patnaik and Goutam Sheet, *Journal of Physics: Condensed Matter* 30, 35 (2018).

4. Dynamic surface modification due to effusion of Na in Na_2IrO_3, Aastha Vasdev, Lalit Yadav, **Suman Kamboj**, Kavita Mehlawat, Yogesh Singh & Goutam Sheet, *Journal of Applied Physics* 124, 055102 (2018).

5. Discovery of highly spin-polarized conducting surface states in the strong spin-orbit coupling semiconductor Sb_2Se_3, Shekhar Das, Anshu Sirohi, Gaurav Kumar Gupta, **Suman Kamboj**, AasthaVasdev, Sirshendu Gayen, Prasenjit Guptasarma, Tanmoy Das & Goutam Sheet, *Physical Review B* 97, 235306 (2018).

6. Field induced hysteretic structural phase switching and charge density wave in Re-doped $MoTe_2$, Aastha Vasdev, **Suman Kamboj**, Anshu Sirohi, Manasi Mandal, Sourav Marik , Ravi Prakash Singh, and Goutam Sheet, (to be communicated)

Abstract

Emergence of novel quantum materials like ferromagnets, superconductors, topological non-trivial materials have introduced new possibilities to the condensed matter physics research. Although the discovery of quantum Hall effect (QHE) triggered the notion of the existence of topological non-trivial materials; the primitive idea, however, was highly motivated by the high-energy physics. These systems may accommodate relativistic particles such as Majorana Fermions, Dirac Fermions, Weyl Fermions, etc. Many theoretical proposals suggest the realization of these relativistic particles in exciting condensed-matter systems. Some signatory evidences have already been experimentally seen, like Weyl fermions have long been known in quantum field theory, but have not been observed as a fundamental particle in nature. A Weyl semimetal is a new state of matter that hosts Weyl fermions as emergent quasiparticles. This eventually opens up the opportunity to realize the relativistic particles in a relatively smaller experimental setup. In this thesis we report the emergence of the synthetic gauge field and a consequent pseudomagnetic field in a doped Weyl semimetal.

Further, if we talk about other novel quantum materials like ferromagnets; ferromagnets are well known for spin phenomenon. In conventional electronics, electronic charge is used for device operation, but using electron's other fundamental property, spin, in addition to or at the place of electronic charge, gives rise to a new field called Spintronics. Spintronics is the branch of physics which deals with the transfer, storage and manipulation of information by means of electronic spin. Traditionally spin phenomena have been detected in ferromagnetic metals and alloys, spin generation and spin-orbit coupling in non-magnetic materials has been revealed recently. The recently discovered topological non-trivials materials like topological insulators have presented new possibilities for spintronics. I will discuss measurement of transport spin-polarization on two systems (i) a complex ferromagnet $EuTi_{1-x}Nb_xO_3$ and (ii) a series of doped topological insulators

(Bi_2Se_3).

To justify the above works, we have chosen the following thesis plan:

Chapter I is an introduction to the work presented in the thesis. This thesis deals with the novel quantum properties of topological non-trivial materials and an itinerant ferromagnet. Some brief introduction about Weyl semimetals and topological insulators is included in this chapter. The methods and attempts that have been made for spin-polarization measurements in ferromagnets and topological materials, have been discussed here. This chapter also includes detailed discussion of point-contact spectroscopy (PCS) on mesoscopic NS junctions in different regimes of transport followed by the discussion of theoretical model.

Chapter II describes details of the experimental techniques used in this thesis work. The scanning tunneling microscopy (STM) and point contact Andreev reflection (PCAR) spectroscopy are used in most of the experiments in the work presented here. A scanning tunneling microscope (USM 1300, Unisoku) is used for the transport spectroscopy experiments in the tunneling regime. The experiments are carried out down to 300 mK temperatures and up to 11 T magnetic field. For the transport spectroscopy in the metallic regime, point contact Andreev reflection (PCAR) spectroscopy is employed. A point contact spectroscopy probe is developed in-house to carry out dI/dV measurements at low temperatures down to 1.4 K and high magnetic field of about 6 Tesla. The data acquisition set-up and method developed in house, is discussed in this chapter.

Chapter III shows the emergence of pseudo-magnetic field in type-II Weyl semimetal on inducing strain in the system. It is known that an external magnetic field facilitates realization of a great variety of unique properties like quantum Hall effect, chiral anomaly, magneto-electric effect etc. in certain novel materials. What if we harbour these properties intrinsically in a material! Harbouring these properties can, in principle, make their implementation possible in new generation technology and fundamental research. In this direction, synthetic generation of an intrinsic magnetic field is a viable alternative which, as per quantum field theory, can be achieved in Dirac/Weyl fermionic systems under inho-

mogeneous strain. This effect was earlier observed by scanning tunneling spectroscopy in graphene, a 2D Dirac material, at localized nano-bubbles under strain. Here, I will present the first experimental evidence of an intrinsic strain-induced pseudo-magnetic field (3 Tesla) over a large area in a three-dimensional type-II Weyl semimetal.

Chapter IV In chapter 4, I will present the measurement of the transport spin polarization of $EuTi_{1-x}Nb_xO_3$. It is important to understand temperature evolution of the magnitude of spin polarization in novel quantum materials. $EuTi_{1-x}Nb_xO_3$ is a low Curie temperature complex itinerant ferromagnet. The low T_c of this material enables us to extract the transport spin polarization all the way up to T_c from point contact Andreev reflection spectroscopy using Nb tip. Here I will also show how generically the spin polarization evolves with temperature proportionately with the bulk magnetization even for a complex material with strong correlations.

Chapter V Here I will discuss about evolution of spin-polarization of Bi_2Se_3 on doping with a magnetic element (Mn). The motivation to work on topological materials is due to their extraordinary behaviour like high spin polarization which may lead to a new aspect of quantum physics as well as in the technological world : spintronic devices, the key element for quantum computing which may drive us into a completely new generation world. Perturbations like magnetic dopant, structural distortion, mechanical strain and disorder etc. can be used to realize novel phases of matter out of topological insulators. In chapter 5, we will see that Bi_2Se_3 surface states show a very large magnitude of spin-polarization. And I will show that on doping Bi_2Se_3 with Mn dopants, the effective spin-polarization of the material is reduced.

CONTENTS

1 Introduction

The exotic physical properties that the new generation quantum materials display, originate from the principles of quantum mechanics that the charge carriers follow [1]. Quantum behaviour of such materials leads to novel ground states like conventional/unconventional superconductivity, magnetism, topologically non-trivial states etc. Such ground states are ideal play grounds of various quantum principles in the non-relativistic and the relativistic regime. Many such quantum phenomena governing the exotic physics of the quantum materials can be explored by spectroscopic measurements. This thesis deals with transport spectroscopy on certain novel quantum materials.

Transport spectroscopy exploits the $I - V$ characteristics across a junction between two materials for which the properties of one of the materials is relatively well understood. Most popularly, transport spectroscopy is done either in the tunneling or in the metallic regimes of transport. In the metallic regime, transport spectroscopy is done by forming mesoscopic point contacts between two materials and by probing the transport characteristics of such point contacts. On the other hand, in the tunneling regime, transport spectroscopy can be done either by making planar tunnel junctions or by using a scanning tunneling microscope. In this thesis, I will present experiments done in both these regimes using various scanning tunneling microscopes. In the tunneling regime experiments, I will show the emergence of a synthetic gauge field and a consequent pseudomagnetic field in a doped Weyl semimetal. Using the experiments done in the metallic regime, I will discuss mea- surement of transport spin-polarization on two systems (i) a complex ferromagnet $EuTi_{1-x}Nb_xO_3$ and (ii) a series of doped topological insulators (Bi_2Se_3). This was done by spin-resolved andreev reflection spectroscopy. In this chapter, I will discuss about the basics of these materials and some of the properties of these materials in brief and also discuss about the point contact Andreev reflection spectrscopy to measure spin-polarization in detail.

1.1 Weyl semimetal

A Weyl semimetal is a semimetal that hosts Weyl fermions as emergent quasi-particles. In order to understand the physics of the Weyl semimetals, let us first look at some basics of relativistic quantum mechanics [2–5].

The Dirac equation describing massive spin-1/2 relativistic particles in d spatial dimension is

$$(i\gamma^{\mu}\partial_{\mu} - m)\psi = 0 \tag{1}$$

where $\mu = 0, 1, ..., d$. This equation has 4-component wave functions and 4 x 4 matrices (the γ matrices):

$$\gamma^0 = \begin{pmatrix} \mathbb{1} & 0 \\ 0 & \mathbb{1} \end{pmatrix}; \quad \gamma^{\mu} = \begin{pmatrix} 0 & \sigma_{\mu} \\ \sigma_{\mu} & 0 \end{pmatrix}$$

where $\mathbb{1}$ is 2x 2 matrix and σ_{μ} denotes pauli spin matrices.

$$(i\gamma^0\partial_t + i\gamma^{\mu}\partial_{\mu} - m)\psi = 0 \tag{2}$$

For 1+1 dimension:

$$(i\gamma^0\partial_t - \gamma^1 p - m)\psi = 0 \tag{3}$$

where $p = -i\partial_x$.

$$(i(\gamma^0)^2\partial_t - \gamma^0\gamma^1 p - \gamma^0 m)\psi = 0 \tag{4}$$

As $(\gamma^0)^2 = \mathbb{1}$ & $(\gamma^{\mu})^2 = -\mathbb{1}$

Thus,

$$i\partial_t\psi = (-i\gamma^0\gamma^1\partial_x + \gamma^0 m)\psi \tag{5}$$

If we set $m=0$, this equation can be further simplified by simply picking eigenstates of the Hermitian matrix $\gamma^5=(\gamma^0)(\gamma^1)=\sigma_x$, if $\gamma^5\psi_\pm=\pm\psi_\pm$, then 1D Weyl equation will be

$$i\partial_t\psi_\pm=\pm p\psi_\pm \tag{6}$$

The + and - signs represent objects moving either to the left or to the right.

In 3+1 dimensions,

$\gamma^0=\mathbb{1}\otimes\tau_x, \quad \gamma^\mu=\sigma_\mu\otimes\tau_y, \quad \gamma^5=-\mathbb{1}\otimes\tau_z$

where

$$\tau_x=\begin{pmatrix}1 & 0\\ 0 & -1\end{pmatrix}; \quad \tau_y=\begin{pmatrix}0 & -i\\ i & 0\end{pmatrix}; \quad \tau_z=\begin{pmatrix}0 & 1\\ 1 & 0\end{pmatrix}$$

Therefore,

$$i\partial_t\psi_\pm=H_\pm\psi_\pm \tag{7}$$

$$H_\pm=\mp\boldsymbol{p}.\boldsymbol{\sigma} \tag{8}$$

The three linearly independent momenta couple to all the three Pauli matrices in the Hamiltonian, hence perturbations can shift the position of the nodes in momentum space but cannot open a gap. Here +ve sign denotes that the Weyl fermions are propagaing parallel to their spin and -ve sign denotes that the Weyl fermions propagate antiparallel to their spin. Weyl fermions propagate parallel (or antiparallel) to their spin, defines their chirality. Let us discuss about the chirality of Weyl fermions.

From equation (2)

$$(\gamma^0p^0-\boldsymbol{\gamma}.\mathbf{p}-m)\psi=0 \tag{9}$$

Let us represent the four component spinor as:

$$\psi=\begin{pmatrix}u_1(p)\\ u_2(p)\end{pmatrix} \tag{10}$$

Here $u_1(p)$ and $u_2(p)$ are two component spinors. In matrix form, equation (9) can be

written as

$$\begin{pmatrix} (p^0-m)\mathbb{1} & -\boldsymbol{\sigma}.\mathbf{p} \\ \boldsymbol{\sigma}.\mathbf{p} & -(p^0-m)\mathbb{1} \end{pmatrix} \begin{pmatrix} u_1(p) \\ u_2(p) \end{pmatrix} = 0 \tag{11}$$

$$(p^0-m)u_1(p) - \boldsymbol{\sigma}.\mathbf{p}u_2(p) = 0 \tag{12}$$

$$\boldsymbol{\sigma}.\mathbf{p}u_1(p) - (p^0+m)u_2(p) = 0 \tag{13}$$

Taking sum and difference of the above equations (equation (12) and (13))

$$(p^0 - \boldsymbol{\sigma}.\mathbf{p})(u_1(p)+u_2(p)) = m(u_1(p)-u_2(p)) \tag{14}$$

$$(p^0 + \boldsymbol{\sigma}.\mathbf{p})(u_1(p)-u_2(p)) = m(u_1(p)+u_2(p)) \tag{15}$$

$$u_L(p) = \frac{1}{2}(u_1(p) - u_2(p) \tag{16}$$

$$u_R(p) = \frac{1}{2}(u_1(p) + u_2(p) \tag{17}$$

$$p^0 u_R(p) - \boldsymbol{\sigma}.\mathbf{p}u_R(p) = mu_L(p) \tag{18}$$

$$p^0 u_L(p) + \boldsymbol{\sigma}.\mathbf{p}u_L(p) = mu_R(p) \tag{19}$$

For m=0;

$$p^0 u_R(p) = \boldsymbol{\sigma}.\mathbf{p}u_R(p) \tag{20}$$

$$p^0 u_L(p) = -\boldsymbol{\sigma}.\mathbf{p}u_L(p) \tag{21}$$

$$p^{0^2}u_R(p) = \boldsymbol{\sigma}.\mathbf{p}p^0u_R(p) = (\boldsymbol{\sigma}.\mathbf{p})(\boldsymbol{\sigma}.\mathbf{p})u_R(p) = \mathbf{p}^2u_R(p) \tag{22}$$

$$(p^0)^2 - \mathbf{p}^2)u_R(p) = 0 \tag{23}$$

For non-trivial solution

$$(p^0)^2 - \mathbf{p}^2) = 0 \tag{24}$$

$$p^0 = \pm|\mathbf{p}| \tag{25}$$

For positive energy solutions, i.e., for $p^0 = |\mathbf{p}|$;

From eqaution (20), we get

$$\frac{\boldsymbol{\sigma}.\mathbf{p}}{|\mathbf{p}|}u_R(p) = u_R(p) \tag{26}$$

And for negative energy solutions, i.e., for $p^0 = -|\mathbf{p}|$, we get

$$\frac{\boldsymbol{\sigma}.\mathbf{p}}{|\mathbf{p}|}u_L(p) = -u_L(p) \tag{27}$$

Thus, from the above expressions, one can see that it is possible to find particles with definite chirality for m = 0. It can be seen that a single chirality of Weyl fermions can not be realized alone in 3D, but momentum separated pairs of two Weyl fermions of opposite chirality can arise.

In the standard model of particle physics, all fermions are Dirac fermions, except possibly neutrinos. It was initially believed that neutrinos could be Weyl fermions. In fact, all neutrinos are left handed whereas antineutrinos are right handed. However, neutrinos were later found to have non-zero mass, therefore they are not regarded as Weyl fermions any longer.

Recently, the possibility of Weyl fermions with definite chirality appeared in certain

condensed matter systems where the Weyl particles could emerge as relativistic quasi-particles [6]. We first try to theoretically understand how a Weyl Hamiltonian can be realized in condensed matter systems.

Consider two non-degenerate bands touching each other at (or near) the Fermi energy. There is degeneracy at the bands touching point. This is an accidental degeneracy and not a consequence of symmetry. If both time reversal symmetry and inversion symmetry are present, then the bands will be totally degenerate. On the other hand, if only time reversal symmetry is present, bands are generally non-degenerate since crystal momentum is reversed under its action, only except at the points where Kramers degeneracy is present. These points are time reversal invariant momenta, where $\vec{k} \equiv$ -$\vec{k}$. Similarly, if time reversal symmetry is broken, and only inversion symmetry is present, the bands are usually non-degenerate. These bands can be brought into degeneracy by tuning some tunable parameter in the Hamiltonian. The generic expression of Hamiltonian for such a system is $H(\mathbf{k}) = f_0(\mathbf{k})\mathbb{1} + f_1(\mathbf{k})\sigma_x + f_2(\mathbf{k})\sigma_y + f_3(\mathbf{k})\sigma_z$, here f_0, f_1, f_2, f_3 are the energy functions. For accidental degeneracy, the requirement is that$f_1 = f_2 = f_3 = 0$. Also, we have imposed one condition in the beginning of this discussion that the bands touching point be close to the Fermi energy, so this requires that we find a system for which $f_0(\mathbf{k})$ is nearly zero.

Now let us discuss the generic dispersion near the band touching point, by expanding the Hamiltonian around $\mathbf{k} = \mathbf{k}_0 + \delta\mathbf{k}$. This gives $H(\mathbf{k}) = f_0(\mathbf{k}_0)\mathbb{1} + \mathbf{v}_0.\delta\mathbf{k}\mathbb{1} + \Sigma_{a=x,y,z}\mathbf{v}_a.\delta\mathbf{k}\sigma^a$, where $\mathbf{v}_\mu = \nabla_k f_\mu(\mathbf{k})|_{\mathbf{k}=\mathbf{k}_0}$ (with $\mu = 0, ..., 3$). And in the special limit $\mathbf{v}_0 = 0$, $\mathbf{v}_a = v_0\hat{a}$; we get $H(\mathbf{k}_0 + \delta\mathbf{k}) = v\delta\mathbf{k}.\sigma$ which is similar to the Weyl Hamiltonian discussed before i.e., $H_\pm = \mp\mathbf{p}.\sigma$. From this, we can say that the bands disperse linearly in three-dimensional (3D) space.

Let us now consider a band insulator having a gap between conduction band and valence band designated with parity +1 and -1 respectively. On tuning spin-orbit interaction in the system, the bands move along the energy line and can cross (overlap with) each other. When the bands overlap, they open a gap everywhere in the momentum space,

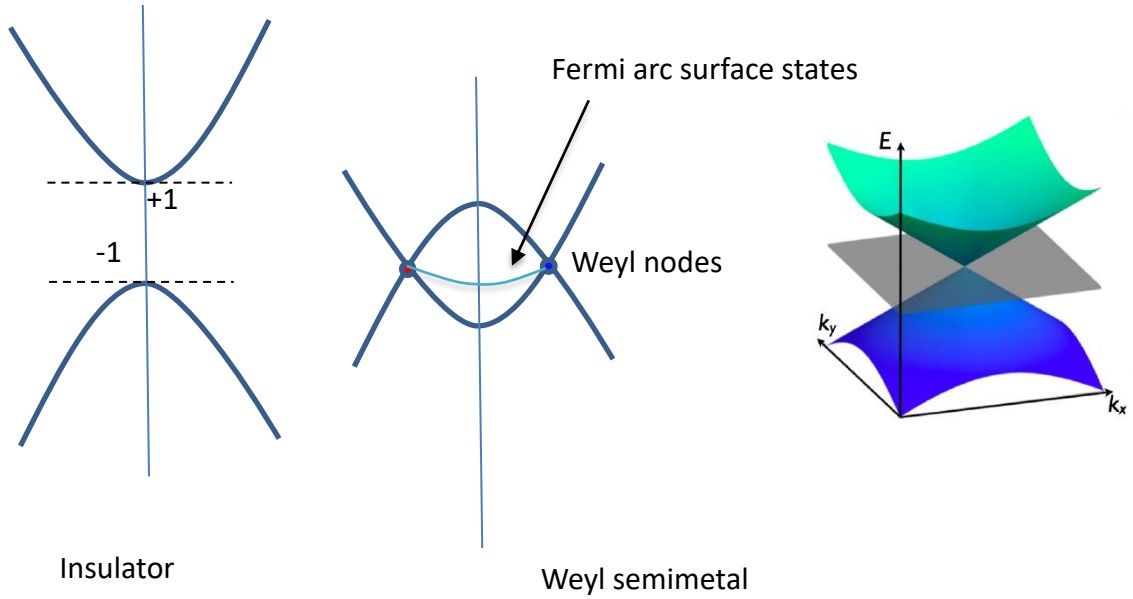

Figure 1.1: Schematic of bands in an insulator (showing a gap between conduction and valence bands) and a Weyl semimetal indicating a gap in bulk bands except at some isolating linearly crossing points, known as Weyl points. Due to the topology of the bulk bands, topological surface states appear on the surface and form exotic Fermi arcs.

except at the points in the Brillouin zone, where the bands intersect. The bands energy dispersion near these points is linear, which essentially represents Weyl dispersion. These points are called the Weyl points [7] and the phase of the matter where this is realized is called Weyl semimetal. The Berry curvature of the Weyl bands (which is like a magnetic field in momentum space) becomes singular at Weyl points with a fixed chirality in momentum space. Thus the Weyl points act as monopoles of the Berry flux [8] with topologically robust charges. These Weyl points are either a source (+ chirality) or a sink (- chirality) of the Berry curvature. Now, in order to diagnose the topology in it, we need to look at the surface states of the gapless system. Surface states are well defined at energy or crystal momentum, where there are no bulk states. If the energy is exactly equal to the energy of the Weyl points, the surface states are well-defined over the entire surface Brillouin zone, except at the two points where Weyl points project on the surface. Here the surface states are very unusual surface states, they take the form of an arc. As we know, Fermi surfaces in 2-D are expected to have a closed curve, but here we have an open curve and the ends of curve are exactly at the points where the surface states leak into the bulk. The Fermi surface, an energy contour crossing the Weyl points, will be an

unclosed line that starts from one Weyl point and ends at the other with opposite chirality. This is called a Fermi arc.

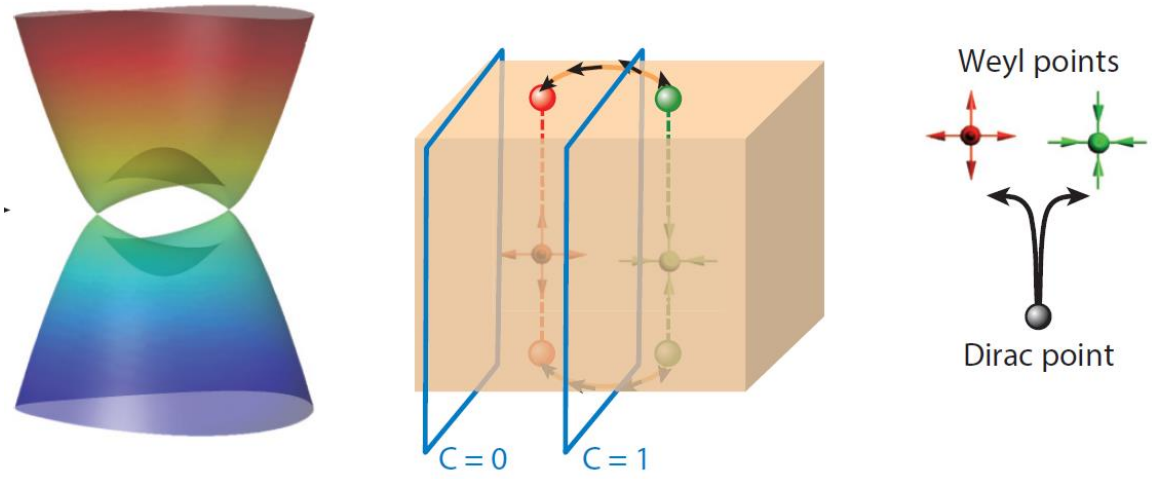

Figure 1.2: In a Weyl semimetal, the bulk bands are gapped by the spin-orbit coupling in the 3D momentum space except at Weyl points. Fig ref. [63]

We have discussed that the Weyl nodes are monopoles of Berry curvature in the Brillouin zone and the charge associated with such a monopole is its chirality. A Fermi surface enclosing a Weyl point has a well-defined Chern number, corresponding to the topological charge of the Weyl point. The net Berry phase accumulated in the two-dimensional (2D) k plane between a pair of Weyl points will induce a non-zero Chern number $C = 1$ with a quantized anomalous Hall effect, whereas the Berry phase is zero in other planes with $C = 0$ as shown in Figure 1.2. Consequently, the Fermi surface, an energy contour crossing the Weyl points, will be an unclosed line that starts from one Weyl point and ends at the other with opposite chirality, called Fermi arc. It is to be noted that the Weyl points are stable to weak perturbations and can only be annihilated in pairs (of opposite charge). With the existence of time reversal symmetry and inversion symmetry, a pair of degenerate Weyl points may coincide, leading to a Dirac point. Or one can say, Weyl semimetal is a semimetal, where a Dirac point gets separated into two Weyl points with opposite chiralities upon time reversal symmetry breaking or inversion symmetry breaking.

1.2 Effect of strain on a Weyl semimetal

Let us define a vector connecting two Weyl points of opposite chirality. Now if we introduce some sort of deformation in the lattice or strain the system, this vector varies in real space, $i.e.$, this vector can have different values as a function of position. Therefore, if in the unstrained system, the Weyl point is at $\mathbf{k}$, then upon straining the system, it will be shifted to $\mathbf{k} + \delta\mathbf{k}$. Now if the strain is non-uniform, $\delta\mathbf{k}$ will be a function of position($\vec{r}$). This is like a gauge field. If a definite curl of this field vector exists, then that can emerge as a pseudo-magnetic field. It has been predicted in high-energy physics a long time ago but the first evidence of pseudomagnetic field was found in graphene [12]. We will discuss this in more detail in chapter 3.

1.3 Topological insulators

Topological insulators are studied extensively in the recent times due to their potential to host novel (relativistic) quantum phenomena. This is an area of physics where application of an abstract mathematical concept like topology found profound applications. In fact, the intriguing feature of these materials is that the topological nature of the wave function of the charge carriers leads to diverse novel quantum properties.

As per the band theroy of solids, insulators are inert to conduction due to finite energy gap seperating the conduction and valence bands [13]. Different insulators are quantitatively differentiated on the basis of band dispersion and the energy gap size. The difference between an ordinary insulator and topological insulator is a matter of topology. In topological insulators, while the bulk is a gapped insulator like a regular band insulator, the surface is gap-less with special spin-momentum locked conducting surface states. The quantum Hall effect [14] is an example of a phenomenon having topological features. It occurs when a 2D gas of electrons is subjected to a strong magnetic field. In presence of a magnetic field, all the energy bands split into sub-bands, known as Landau levels. This leads to distinct quantized plateaus in the quantum Hall resistance for certain particular

values of the applied field. Each quantum Hall plateau represents a definite topological invariant (the "Chern number"). When the Fermi level lies in between the Landau levels, the bulk of the 2D gas of electrons becomes gapped like an insulator, but the edges host special conducting states (the so-called "edge states") through which electric current can flow. In topological insulators, similar behaviour is seen even in the absence of an externally applied magnetic field – crudely putting, the effect of the magnetic field is played by spin-orbit coupling in topological insulators.

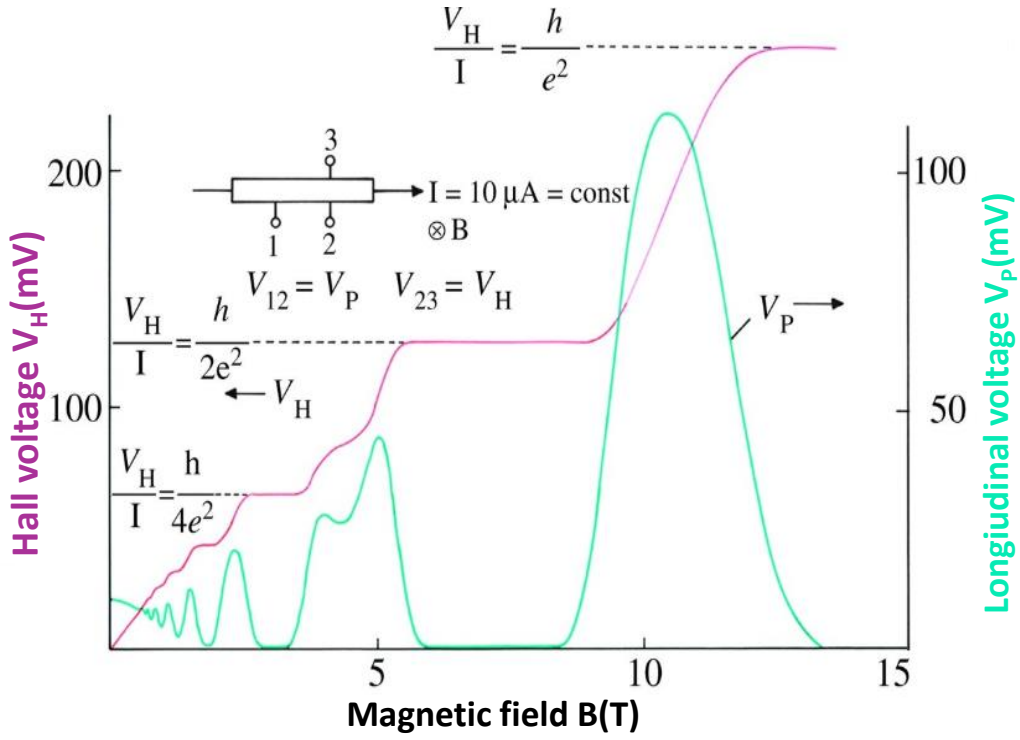

Figure 1.3: Integer quantum Hall effect. Both the transverse and longitudinal resistances are shown. Image ref. [15]

Here we will first try to understand the role of topology in topological insulators. For that, we first discuss the idea of Berry phase in quantum mechanics. That will help us define/identify topological invariants in topological insulators.

Consider a general Hamiltonian H(**R**), which is a function of several parameters represented as a vector **R** = (R1, R2, ..). At any instant, for a fixed **R**, the solutions can be

obtained using the time-independent Schrödinger equation as

$$H(\mathbf{R})\,|n(\mathbf{R})\rangle = E_n(\mathbf{R})\,|n(\mathbf{R})\rangle \tag{28}$$

Let us consider the system is initially in the state $|n(\mathbf{R}(t=o))\rangle$. The system will evolve to the state $|n(\mathbf{R}(t))\rangle$ at any later time. As according to adiabatic theorem, for a slowly varying Hamiltonian, a system initially in the eigenstate will always remain in its instantaneous eigenstate at any later time. Therefore, $|n(\mathbf{R}(t))\rangle$ will also be the instantaneous eigenstate of $H(\mathbf{R}(t))$ with slowly varying $\mathbf{R}$. We can also write the time evolved state as $|\psi(t)\rangle = e^{-i\theta t}\,|n(\mathbf{R}(t))\rangle$. This state will follow the Schrödinger equation

$$H(\mathbf{R}(t))\,|\psi(t)\rangle = i\hbar\frac{d}{dt}\,|\psi(t)\rangle \tag{29}$$

on differentiating the above equation

$$E_n(\mathbf{R}(t)\,|n(\mathbf{R}(t))\rangle = \hbar\left(\frac{d}{dt}\theta(t)\right)|n(\mathbf{R}(t))\rangle + i\hbar\frac{d}{dt}\,|n(\mathbf{R}(t))\rangle \tag{30}$$

Taking the scalar product with $\langle n(\mathbf{R}(t))|$ and assuming the state is normalised, we get

$$E_n(\mathbf{R}(t) - i\hbar\,\langle n(\mathbf{R}(t))|\,\frac{d}{dt}\,|n(\mathbf{R}(t))\rangle = \hbar\left(\frac{d}{dt}\theta(t)\right) \tag{31}$$

$$\theta(t) = \frac{1}{\hbar}\int_0^t E_n(\mathbf{R}(t^{'}))dt^{'} - i\int_0^t \langle n(\mathbf{R}(t^{'}))|\,\frac{d}{dt^{'}}\,|n(\mathbf{R}(t^{'}))\rangle\,dt^{'} \tag{32}$$

The first term of the phase is just the conventional dynamical phase that arises due to the time evolution of the Hamiltonian. The negative of the second term is what is known as the Berry phase γ_n,

$$\gamma_n = i\int_0^t \langle n(\mathbf{R}(t^{'}))|\,\frac{d}{dt^{'}}\,|n(\mathbf{R}(t^{'}))\rangle\,dt^{'} \tag{33}$$

$$\gamma_n = i \int_0^t \langle n(\mathbf{R}(t^{'}))| \nabla_{\mathbf{R}} |n(\mathbf{R}(t^{'}))\rangle \frac{d\mathbf{R}}{dt^{'}} dt^{'} \tag{34}$$

$$\gamma_n = i \int_{\mathbf{R}_0}^{\mathbf{R}_t} \langle n(\mathbf{R})| \nabla_{\mathbf{R}} |n(\mathbf{R})\rangle \, d\mathbf{R} = \int_{\mathbf{R}_0}^{\mathbf{R}_t} A_n(\mathbf{R}) d\mathbf{R} \tag{35}$$

Therefore,

$$A_n(\mathbf{R}) = \langle n(\mathbf{R})| \nabla_{\mathbf{R}} |n(\mathbf{R})\rangle \tag{36}$$

When $\mathbf{R}$ is transported around a closed loop, $|n(\mathbf{R})\rangle$ acquires a well defined Berry phase given by the line integral of $A_n(\mathbf{R}) = \langle n(\mathbf{R})| \nabla_{\mathbf{R}} |n(\mathbf{R})\rangle$ [32]. Topological invariants of phases of matter can be calculated by the Berry phase. First, let us discuss topological invariants through Gauss-Bonnet theorem and then will see how Berry phase helps in defining topological invariants.

As we discussed topology is a mathematical concept to classify shapes or geometries. If any object can be continuously transformed into other by bending or stretching then all the geometries, one can make out of the given geometry, will be topologically equivalent. For example, a doughnut and a coffee cup belong to the same topological class as both the shapes can be characterized by the single hole in the shapes. It can be better understood by the mathematical interpretation of Gauss-Bonnet theorem. According to the Gauss-Bonnet theorem, the integral of the curvature over the whole surface is a topological invariant.

$$\int_C k dS = 4\pi(1-g) \tag{37}$$

Here, k is the Gaussian curvature of an object and Gaussian curvature of the surface of an object can be evaluated by counting the number of holes in a given object. This statement tells that the integration of Gaussian curvature all over the surface is equal to $4\pi(1-g)$, here g represents the number of holes in the given object. Small deformations on the surface can modify the curvature locally but the integral over all the surface will still be equal to $4\pi(1-g)$. Therefore, g is a topological invariant which is not going to change by the small deformations on the given surface.

In condensed matter physics, it has recently been discovered that certain quantum phases of matter display unique physical properties that can be understood only by the quantities analogous to the topological invariant g. Quantum phases with an energy gap (e.g. Band insulator, semiconductor) are topologically equivalent if they can be smoothly deformed into one another without closing the gap. Two quantum mechanical wavefunctions can be in the same topological class if they are connected adiabatically into each other. A normal band insulator is characterized by the finite gap at the Fermi-level. The transition from normal band insulator into the topological insulator needs to close the gap somewhere in between at the critical point where valence band touches the conduction band at a single point. Therefore, these phases are in different topological class. Such phases can be described well within the framework of topological band theory. Thouless, Kohmoto, Nightingale, and den Nijs (TKNN) defined the topological phases by introducing topological invariants.

With the help of Berry phase, one can define Chern invariant, which is a topological invariant. Berry phase may be expressed as a surface integral of the Berry flux $F_n = \nabla \times A_n$. The Chern invariant is the total Berry flux in the Brillouin zone given by,

$$m_n = \frac{1}{2\pi} \int d^2\mathbf{R} F_n \tag{38}$$

Here m_n is integer quantized is analogous to $2(1-g)$ as given in Gauss-Bonnet theorem by equation (37). The total Chern number, summed over all occupied bands, $m = \sum_{n=1}^{N} m_n$ is invariant even if there are degeneracies between occupied bands, provided the gap separating occupied and empty bands remains finite. The Chern number m is a topological invariant in the sense that it can not change when the Hamiltonian varies smoothly.

1.4 Time reversal symmetry in topological insulators

In topological insulators, the usual ordering of conduction and valence bands in ordinary insulator is inverted by strong spin-orbit coupling. This bulk band inversion gives rise to conducting surface states. These surface states show a Dirac cone type dispersion where spin and momentum are locked up in a manner that they are perpendicular to each other [see appendix]. Thus if spin-up charge carriers are moving in the positive x-direction, then the spin-down charge carriers are bound to move in the negative x-direction, any mixture of these is prohibited. So, if the transport through the system is in just one direction, only one kind of spin can contribute to transport, thus the current flowing in the system is spin polarized. Also, these surface states are protected by time reversal symmetry. Let us discuss about time reversal symmetry in topological insulators through Kramer's theorem.

According to Kramers theorem, states with an uneven number of fermions or single electron states must be two fold degenerate (at least) under the preservation of time reversal symmetry. To demonstrate the Kramer's degeneracy, let us start with an antiunitary operator that represents time reversal symmetry is given by $\Theta = Ke^{i\pi S_y/\hbar}$ where S_y is spin operator. For a syatem with odd number of spin 1/2 electrons, Θ has the property $\Theta^2 = -1$. Suppose a system has a nondegenerate energy eigenstate $|\psi\rangle$, such that $\Theta|\psi\rangle = c|\psi\rangle$ for some constant c. This would mean $\Theta^2|\psi\rangle = |c|^2|\psi\rangle$ which is not possible because $|c|^2 \neq -1$. Thus the system containing an odd number of fermions, the assumption of a nondegenerate energy level must be incorrect. Thus we can conclude that in time-reversal invariant systems with an odd number of fermions, the energy levels are always degenerate. This is called Kramer's degeneracy [32, 33]. In the absence of spin-orbit interactions, Kramer's degeneracy is simply the degeneracy between up and down spins. In the presence of spin-orbit interactions, however, it has nontrivial consequences.

A T invariant Bloch Hamiltonian must satisfy

$$\Theta\hat{H}(k)\Theta^{-1} = \hat{H}(-k) \tag{39}$$

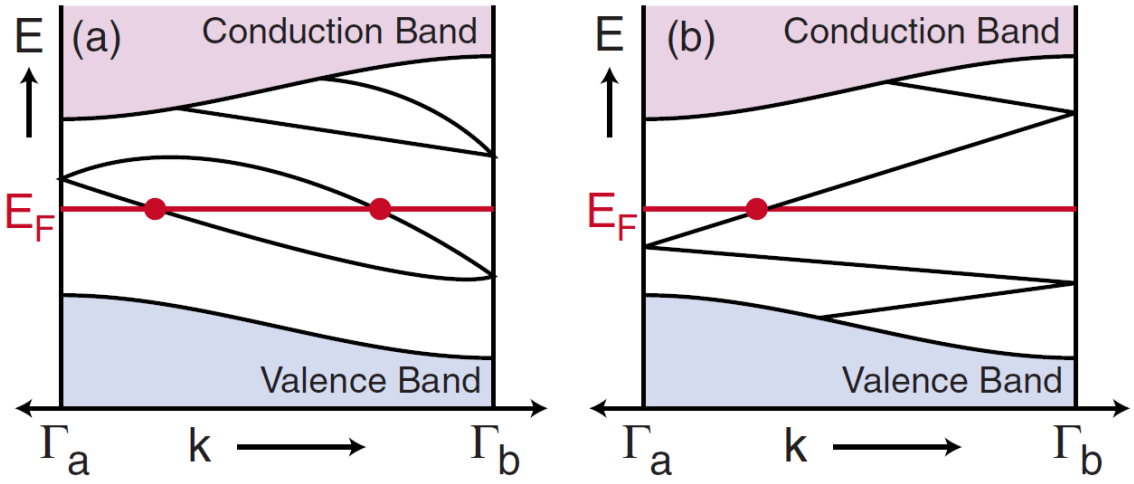

Figure 1.4: The surface state crosses the Fermi level even number of times indicates topologically trivial system. (b) The surface state crosses the Fermi level odd number of times indiicates topologically non-trivial system. Image ref: [29].

One can transform the Hamiltonian (satisfying this constraint) of one topological state into another under smooth deformation without closing the energy gap. The edge states are doubly degenerate and split up due to spin orbit coupling away from the time reversal invariant points i.e., high symmetry points ($k_x = 0, \pi/a$). We will show only half of the Brillouin zone $0 < k_x < \pi/a$ because T symmetry requires that the other half $-\pi/a < k < 0$ is a mirror image. The states at the time reversal invariant points ($k_x = 0, \pi/a$) can be connected in two ways. One way is they connect pairwise and not bound to the edge inside the gap. In this case the edge states are eliminated by pushing all the bound states out of the gap. Here the bands intersect the E_F even number of times between k=0 and $k = \pi/a$ as shown in Figure 1.4(a), and other way is bands intersect E_F an odd number of times and the edges states can not be eliminated. There will atleast one surface state which is gapless as can be seen in Figure 1.4(b). The system shown in Figure 1.4(a), may or may not have edge states and are topologically trivial systems while the system shown in Figure 1.4(b), will always have some edge states, indicating a topologically non-trivial system.

Thus, here we have discussed a bit about topological insulators and time reversal sym-

metry in topological insulators. Now what will happen if we dope a topological insulator with a magnetic impurity, the surface states will not be protected by time reversal symmetry anymore. Thus the topological character of spin polarized surface states will be reduced. In chapter 4, we will discuss the evolution of spin polarization in Bi_2Se_3 with the emergence of ferromagnetism on Mn doping.

1.5 Ferromagnets and spin polarization in a ferromagnet

A ferromagnet is a material in which permanent atomic magnetic moments align themselves in the absence of any external magnetic field. The exchange interaction among the neighbouring atoms, is responsible for the alignment of these magnetic moments. A domain (atoms in a group) in ferromagnet, grows in size in the presence of magnetic field [34] .

As we know magnetism of 3d transition metals has always been the subject of continued interest. Now, One can think whether the d electrons, which are responsible for magnetism, are localized on atoms or whether they are itinerant electrons transferring from atom to atom in a crystal. However, it is now generally accepted that the d electrons in transition metals are itinerant electrons that are interacting strongly with each other. The simplest model to explain ferromagnetism is Stoner model. In the Stoner theory, the uniform mean exchange field decreases with increasing temperature and vanishes above the Curie temperature T_c and ferromagnetism is destroyed by spin-flip thermal excitations of electrons across the Fermi level. Thus the Stoner excitations reduce the magnitude of magnetization, so that finally at the Curie temperature the itinerant system becomes a non-magnetic material.

Along with magnetization there is another property associated with ferromagnets called spin polarization. Spin polarization is the extent to which the spin, is aligned in a given direction. Spin polarization in ferromagnets is defined as difference of density of states of spin up channels and density of states of spin down channels at Fermi level

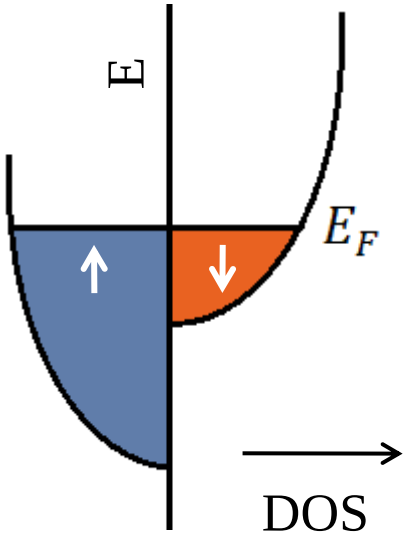

Figure 1.5: Band diagram for a ferromagnet showing up-spin and down-spin bands.

divided by total density of states at the Fermi level.

$$P = \frac{\mathbf{N}_{\uparrow}\ (\mathbf{E_F}) - \mathbf{N}_{\downarrow}(\mathbf{E_F})}{\mathbf{N}_{\uparrow}\ (\mathbf{E_F}) + \mathbf{N}_{\downarrow}(\mathbf{E_F})} \tag{40}$$

1.6 Theory of spin polarization measurements

Spin polarization can be investigated in a number of ways. Typical experiments that can probe P are spin resolved photoemission spectroscopy [35] and hard X-ray photoemission spectroscopy [36, 37]. However, these experiments involve complicated experimental set up and dependent on synchroton radiation and are also extreme surface sensitive. Another useful method is the tunneling spectroscopy. Pioneering experiments by Tedrow and Meservey [38, 39] earlier revealed that tunnel junction for ferromagnet/ insulator/superconductor (F/I/S) involves spin dependent tunneling from a ferromagnet to the superconductor requiring the fabrication of high quality junctions. Another technique, based on the combination of tunneling magnetoresistance (TMR) and F/I/F junction-Julliere's model, is also used for estimating the degree of spin polarization [40]. In this case, the results strongly depend on the structural quality of material system and the choice of the tunneling barrier material. On the other hand, Point Contact Andreev Reflection (PCAR) spectroscopy involving Andreev reflection [41] at the interface be-

tween a ferromagnet and superconductor is a versatile technique for direct probing of spin-polarization. The advantage of this novel technique lies in its device-independence without the requirement of fabrication of tunnel junction and/or application of magnetic fields. In a transport experiment like PCAR, the relevant quantity is not the absolute spin polarization but the so called "transport spin polarization" which is defined as: P_t = ($\langle N_\uparrow v_{F\uparrow}\rangle_{FS}$ - $\langle N_\downarrow v_{F\downarrow}\rangle_{FS}$)/($\langle N_\uparrow v_{F\uparrow}\rangle_{FS}$ + $\langle N_\downarrow v_{F\downarrow}\rangle_{FS}$), where $N_\uparrow$ and $N_\downarrow$ are the density of states (DOS) of the up and down spin channels respectively at the Fermi level and $v_{F\uparrow}$ and $v_{F\downarrow}$ are the respective Fermi velocities.

1.7 Point contact Andreev reflection(PCAR)

Point-contact spectroscopy is a technique to study various mechanisms of electron scattering in metals. Point-contact spectroscopy studies the non-linearity of the current-voltage characteristics (deviation from Ohm's law) resulting from the scattering of the electrons.

Point-contact spectroscopy is different from tunneling spectroscopy. In tunneling spectroscopy, quantum mechanical tunneling of the electrons occurs through an insulating gap between two electrodes whereas in point contact spectroscopy two electrodes are kept in metallic contact and the scattering process occuring in this metallic contact, is probed to gain energy resolved spectroscopy information. Tunneling spectroscopy is more surface sensitive technique as compared to point contact spectroscopy. Also, the inelastic scattering of tunneling electrons between normal metals gives rise to extra channels for the electrons to tunnel through the barrier, whereas in Point Contact Spectroscopy, the inelastic scattering of the electrons gives a negative contribution to total current.

The resistance to electronic transport between two metals across point contact is given by Wexler's formula [42] as shown below:

$$R_{PC} = \frac{2h/e^2}{(ak_F)^2} + \Gamma(l/a)\frac{\rho(T)}{2a} \tag{41}$$

where, h is the Planck's constant, e is the charge of a single electron, a is the contact diameter and l is the mean free path (elastic or inelastic) of an electron. $\Gamma(l/a)$ denotes a slowly varying function of the order of unity. ρ is the bulk resistivity of the material and T is the effective temperature at the point-contact.

Point contact spectroscopy can also be used to measure superconducting gap, spin polarization and symmetry order parameter, when the contact is established between a normal metal and a superconductor. In point contact spectroscopy, a contact of size of the order of 1 $\mathring{A}$ to few hunderds of nm (point contact) is established between a superconductor and normal metal across which a voltage is applied. Based on the contact diameter, the transport of electrons between metal and superconductor occurs in different regimes:

(a) Quantum Regime: If the diameter of point-contact is of the order of angstrom $i.e.$,

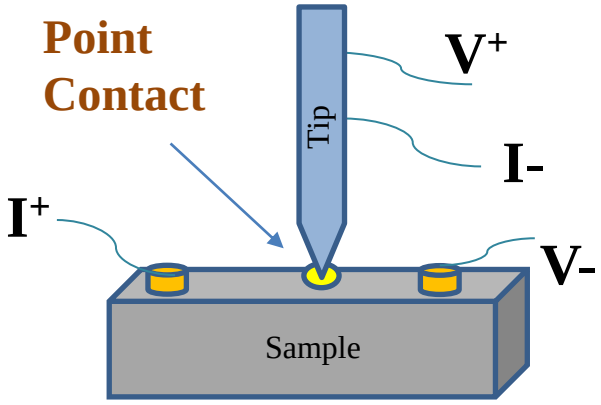

Figure 1.6: The schematic diagram of point contact spectroscopy experiment, showing a point-contact between tip and sample.

of the order of de Broglie wave length of electron, then the transport is in quantum regime. In this regime, conductance gets quantized and is given by $G_0 = N\frac{2e^2}{h}$, where N is number of the conducting channels [43].

(b) Ballistic Regime: If the diameter of point-contact becomes larger than the de Broglie wave length and smaller than the electronic elastic mean free path (l_e) $i.e.$, $a < l_e$, then the contact is said to be in ballistic regime. In this regime, statistically, the electrons do not undergo any inelastic scattering across the interface and they pass through the contact without any dissipation. However, because of large number of conducting channels and physical properties of point-contact, there is always some finite resistance at a meso-

scopic contact which is equal to the Sharvin's resistance (R_S) represented as a first term in the equation. The first term of the equation (41) depends only on the geometry of the point-contact.

(c) Thermal Regime: In thermal regime, the contact diameter is larger than the inelastic electronic mean free path of electrons (l_i) $i.e.$, $a < l_i$ where inelastic scattering becomes more prominent. The point-contact resistance in this regime is represented by Maxwell's resistance (R_M) $i.e.$, the second term in equation (41). It depends directly on the resistivity of the materials forming the point-contact. Energy dissipation occurs in thermal regime due to inelastic scattering.

(d) Intermediate Regime: In intermediate regime, the contact size lies somewhere in between two extreme regimes $i.e.$, ballistic and thermal regimes. In this regime both Sharvin's resistance and Maxwell's resistances contribute. The contact resistance is given by Wexler's formula given by the equation(41).

1.7.1 Andreev Reflection

Andreev reflection occurs at the interface between a superconductor and a normal metal in ballistic region. Andreev reflection can be illustrated as following: A voltage is applied across the metal-superconductor interface, the electron with energy E_1 will transmit from the metal to superconductor in its normal state and with energy E_2, the electron can not transmit as the energy falls in the energy range of superconducting gap. Here the electron incident on the interface reflects back as a hole with opposite spin to that of incident electron and to conserve the charge, a cooper pair is generated at the Fermi level of the superconductor. Thus a normal current is converted to a super current. This process is called Andreev reflection. Andreev reflection is studied by analysing the normalized differential conductance $\frac{G(V)}{G_n}$ vs. V where $G(V) = \frac{dI}{dV}$ and $G_n = G\left(V \gg \frac{\Delta}{e}\right)$ and V is the applied dc voltage across the N/S point-contact. Thus, the spectrum which we obtained from $\frac{G(V)}{G_n}$ vs. V is known as point-contact Andreev reflection (PCAR) spectrum. Now, I will discuss about the analysis of this PCAR spectrum.

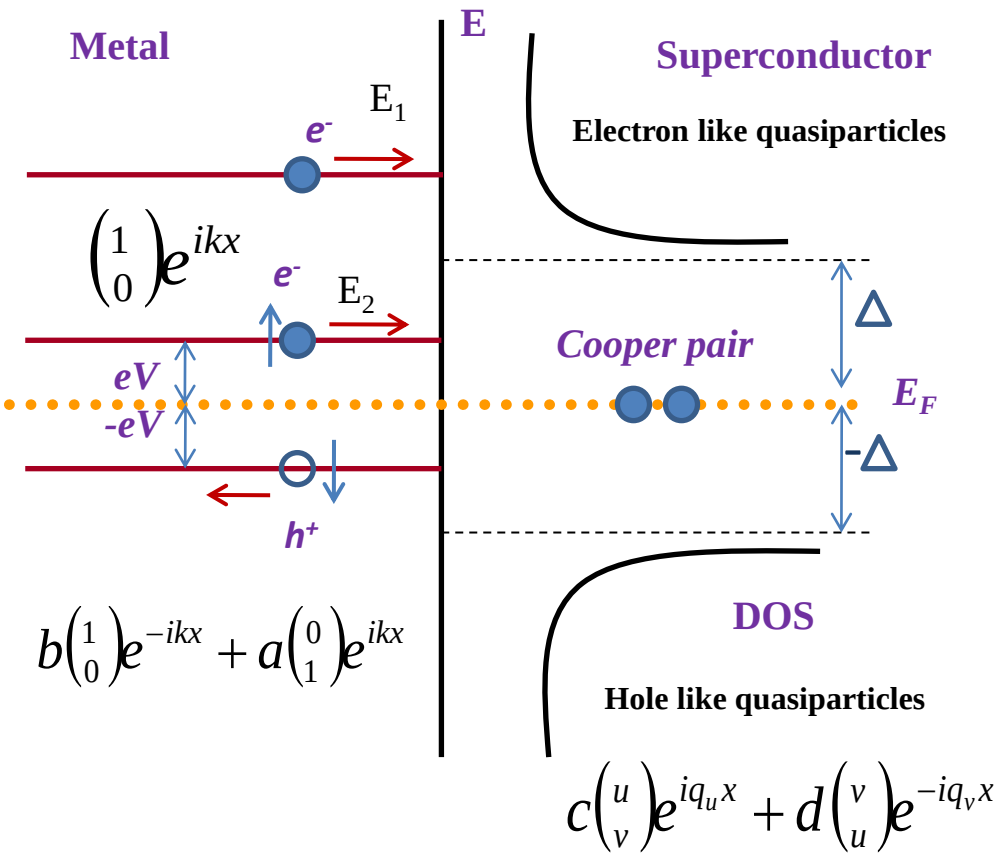

Figure 1.7: A schematic diagram of Andreev reflection process, describing electronic transport from a metal to a superconductor in the ballistic regime of transport.

1.7.2 Analysis of the PCAR spectrum

To analyze the PCAR spectrum, we use a theoretical model given by Blonder, Tinkham and Klapwijk (BTK) [44]. This model is one dimensional model. The model considers all the possible processes like transmission, reflection and Andreev reflection that occur at NS junctions, where electrons move perpendicular to the interface of two materials. The interface between normal metal and superconductor is made up of delta function potential, $H = V_o\delta(x)$. The barrier potential strength is characterised by a dimension less parameter $Z = \frac{V_0}{\hbar v_F}$, (where V_0 is the potential , $\hbar$ is the planck's constant and v_F is the Fermi velocity). This barrier potential at the junction arises due to presence of oxide layer and Fermi mismatch (as the Fermi velocities of two different materials are different), due to which the interface can never be transparent.

There will be an energy shift due to accelerating potential. We are assuming that the distribution function of all the incoming particles is given by the equilibrium Fermi function. We are choosing the electrochemical potential of the pairs in the superconductor as our reference level, as it remains a well defined quantity even when the quasiparticle populations are far from equilibrium. If electrons tunnel through an NS junction, then number of occupied states is $N_N(E-eV)f(E-eV)$ and number of unoccupied final states is $N_S(E)[1-f(E)]$. Here, $N_N(E-eV)$ is density of states of the normal metal, $N_S(E)$ is quasi-particle density of states of the superconductor and $f(E)$ is the Fermi function. The forward current probability is $N_N(E-eV)f(E-eV)N_S(E)[1-f(E)]$ and for reverse current joint probability for this process is $N_N(E-eV)[1-f(E-eV)]N_S(E)f(E)$. By subtracting the reverse current from the forward current, net current through an NS junction is [44, 45]

$$I_{NS} = \alpha \,|\, T \,|^2 \int_{-\infty}^{+\infty} N_N(E-eV)N_S(E)[f(E-eV)-f(E)]dE \tag{42}$$

where α is the constant that depends upon the junction and Fermi velocity. $|\,T\,|^2$ is a phenomenological tunneling matrix element that depends on the type of insulator between the N/S junction and governs whether the event occurs. In practice, $N_N(E) = N_N(0)$, then differential conductance at T= 0 is given as below:

$$G_{NS} \equiv \frac{dI_{NS}}{dV} \,|_{T=0} \propto N_S(e \,|\, V \,|) \tag{43}$$

The calculated dI/dV gives the density of states of a superconductor [46].

In PCAR electrons move through a point-contact and suffer scattering during transport. We know the interface can never be transparent, thus, electron has some finite probability of reflection $i.e.$, normal reflection. A(E) and B(E) are the Andreev reflection and normal reflection probabilities respectively, and C(E) is the probability of transmission through the interface with a wave vector on the same side of the Fermi surface (i.e., $k \rightarrow q_u$), while D(E) gives the probability of transmission with crossing through the Fermi

surface (i.e., $k \to -q_v$). With this convention, all incoming electrons from the superconductor side have the distribution function $f(E)$, while those coming in from the Normal metal side are described by $f(E-eV)$. Then the current through the interface can be described as follows:

$$I = \mathscr{A} J = 2N(0)ev_F \mathscr{A} \int_{-\infty}^{+\infty} [f_{\rightarrow}(E) - f_{\leftarrow}(E)]dE \tag{44}$$

Where $\mathscr{A}$ is effective neck cross sectional area, N(0) is the one-spin density of states at ϵ_F, v_F is the Fermi velocity and $f_{\rightarrow}(E) = f(E - eV)$ and

$$f_{\leftarrow}(E) = A(E)[1 - f_{\rightarrow}(-E)] + B(E)f_{\rightarrow}(E) + [C(E) + D(E)]f(E) \tag{45}$$

here $f(-E) = 1 - f(E)$ and conservation of probabilities gives $A + B + C + D = 1$

$$I_{ballistic} = 2N(0)ev_F \mathscr{A} \int_{-\infty}^{+\infty} [f(E - eV) - (A(E)f(E + eV) + B(E)f(E - eV) + [1 - A(E) - B(E)]f(E))]dE \tag{46}$$

$$I_{ballistic} \propto N(0)\nu_F \int_{-\infty}^{+\infty} [f(E - eV) - f(E)][1 + A(E) - B(E)]dE \tag{47}$$

If we use the BTK formulation to incorporate ARs (Andreev reflections), the current that flows across the junction is:

$$I_{ballistic} \propto \int_{-\infty}^{+\infty} [f(E - eV) - f(E)][1 + A(E) - B(E)]dE \tag{48}$$

Thus, we are left with the terms A(E) and B(E) in the expression of current flowing through the junction. Thus we will focus on calculating A(E) and B(E) in the coming algebraic calculations. The coefficient of A(E) and B(E) can be calculated by applying the boundary conditions for delta function with the wave function satisfying the Bogoliubov-

deGennes [47] equation which is given as follows.

$$i\hbar\frac{\partial f(x,t)}{\partial t}=\left[-\frac{\hbar^2\nabla^2}{2m}-\mu(x)+V(x)\right]f(x,t)+\Delta(x)g(x,t) \tag{49}$$

$$i\hbar\frac{\partial g(x,t)}{\partial t}=\left[-\frac{\hbar^2\nabla^2}{2m}-\mu(x)+V(x)\right]g(x,t)+\Delta(x)f(x,t) \tag{50}$$

Where $\Delta(x)$ is the gap, $\mu(x)$ is the chemical potential, $f(x,t)$ and $g(x,t)$ are the elements of two-element column vector $\psi=\begin{bmatrix}f(x,t)\\g(x,t)\end{bmatrix}$ (which describes one type of the BCS quasiparticle states and proportional to u and v respectively). Deep in the superconducting electrode where $\Delta(x)$, $\mu(x)$, and $V(x)$ are constants, the solutions to equations (49) and (50) can be taken as $f(x,t)=ue^{ikx-iEt/\hbar}$, $g(x,t)=ve^{ikx-iEt/\hbar}$

For V=0;

we get

$$Eu=\left[\frac{-\hbar^2k^2}{2m}-\mu\right]u+\Delta v \tag{51}$$

$$Ev=\left[\frac{-\hbar^2k^2}{2m}-\mu\right]v+\Delta u \tag{52}$$

For each E, we have

$$\frac{\hbar^2k^2}{2m}=\mu\pm\sqrt{E^2-|\Delta|^2} \tag{53}$$

For $E>0$;

$$u^2=\frac{1}{2}\left(1+\frac{\sqrt{E^2-\Delta^2}}{E}\right) \tag{54}$$

The solution of Bogoliubov equation corresponds to the incident, reflected and transmitted wave and are given by

$$\psi_{inc} = \begin{bmatrix} 1 \\ 0 \end{bmatrix} e^{ikx} e^{-iEt/\hbar} \tag{55}$$

$$\psi_{refl} = \left(a \begin{bmatrix} 0 \\ 1 \end{bmatrix} e^{ikx} + b \begin{bmatrix} 1 \\ 0 \end{bmatrix} e^{-ikx} \right) e^{-iEt/\hbar} \tag{56}$$

$$\psi_{tran} = \left(c \begin{bmatrix} u \\ v \end{bmatrix} e^{iq_u x} + d \begin{bmatrix} v \\ u \end{bmatrix} e^{-iq_v x} \right) e^{-iEt/\hbar} \tag{57}$$

The boundary conditions for particles moving at $x = 0$ from normal metal to superconductor are as follow:

(i) ψ at $x = 0$, so $\psi_S(0) = \psi_N(0)$

(ii) $(\hbar/2m)(\psi'_S - \psi'_N) = H\psi(0)$, the derivative of boundary condition for delta function.

Let us assume $k = q_u = q_v$. This assumption was made by BTK for simplicity of the algebraic calculations. $A(E)$ is the AR probability and $B(E)$ is the normal reflection probability that is given by $A(E) = aa^*$ and $B(E) = bb^*$ respectively.

$$A(E) = \frac{\Delta^2/E^2}{1 - \varepsilon(1 + 2Z^2)^2}, \quad for E < \Delta \tag{58}$$

$$A(E) = \frac{(uv)^2}{\gamma^2}, \quad for E > \Delta \tag{59}$$

$$B(E) = 1 - A(E), \quad for E < \Delta \tag{60}$$

$$B(E) = \frac{((u)^2 - (v)^2)^2 Z^2 (1 + Z^2)}{\gamma^2}, \quad for E > \Delta \tag{61}$$

where $\gamma^2 = ((u^2 - v^2)Z^2 + u^2)^2$ and $\varepsilon = (E^2 - \Delta^2)/E^2$.

The expression for the dI/dV of an NS junction corresponding to the AR process at

$T = 0$ is given as below:

$$G_{ballistic} = \frac{dI_{NS}}{dV} |_{T=0} \propto (1 + A(eV) - B(eV)) \tag{62}$$

In BTK theory, only the elastic scattering was accounted at the interface, but practically the electrons also experience inelastic scattering. In order to compensate the discrepancy, one another parameter associated with quasiparticle lifetime was added in the modified BTK model. The formalism of the modified theory is depicted below.

$$i\hbar \frac{\partial f(x,t)}{\partial t} = -[\frac{\hbar^2 \Delta^2}{2m} + \mu(x) + i\Gamma - V(x)]f(x,t) + \Delta g(x,t) \tag{63}$$

$$i\hbar \frac{\partial g(x,t)}{\partial t} = -[\frac{\hbar^2 \Delta^2}{2m} + \mu(x) + i\Gamma - V(x)]g(x,t) + \Delta f(x,t) \tag{64}$$

The solutions to these equations can be taken as $f(x,t) = ue^{ikx - i(E+i\Gamma)t/\hbar}$, $g(x,t) = ve^{ikx - i(E+i\Gamma)t/\hbar}$

$A(E) = aa^*$ and $B(E) = bb^*$, where the coefficients a and b are given by

$$a = uv/\gamma \tag{65}$$

$$b = -(u^2 - v^2)(Z^2 + iZ)/\gamma \tag{66}$$

where u^2 and v^2 are the probabilities of an electronic state being occupied and unoccupied respectively which are written as:

$$u^2 = \frac{1}{2}[1 + \frac{\sqrt{(E + i\Gamma) - \Delta^2}}{E + i\Gamma}] \tag{67}$$

$$v^2 = 1 - u^2 \tag{68}$$

$$\gamma = u^2 + (u^2 - v^2)Z^2 \& \gamma^2 = \gamma\gamma^* \tag{69}$$

Consequently, the probabilities A(E) and B(E) will get modified on taking the effect of Γ into account.

Modified BTK theory with spin polarization: When the metal in the metal-superconductor point contact is a ferromagnet, the Fermi level is expected to be spin polarized. This means, the density of states of the up-spin electrons ($N_\uparrow$) is not equal to the density of states of the spin down electrons ($N_\downarrow$) at the Fermi level. Now, in an $N - S$ point contact, the electron undergoes Andreev reflection, a hole is generated propagating in the spin down band opposite to that of the incident electron. Thus, $|N_\uparrow - N_\downarrow|$ electrons encountering the interface can not undergo Andreev reflection because they do not find accessible states in the opposite spin band. Therefore, in a point-contact between a ferromagnetic metal and a conventional superconductor, Andreev reflection is suppressed. By measuring the degree of this suppression, the spin-polarization of the Fermi surface is measured. In order to extract the absolute value of the Fermi level spin polarization, first the BTK current is calculated for zero spin polarization (I_{BTKu}) and 100% spin polarization (I_{BTKp}) respectively. Then the current for an intermediate spin polarization P_t is calculated by interpolation between (I_{BTKu}) and (I_{BTKp}) following the relation $I_{total} = I_{BTKu}(1 - P_t) + P_t I_{BTKp}$. As per BTK theory [44, 48] when the point contact is between a superconductor and an unpolarized (normal) metal, the current is given by

$$I_{\mathrm{u}} = C \int_{-\infty}^{+\infty} [f(E - eV) - f(E)][1 + A_{\mathrm{u}}(E) - B_{\mathrm{u}}(E)]dE \tag{70}$$

Where, $A_{\mathrm{u}}(E)$ is the AR probability and $B_{\mathrm{u}}(E)$ is the normal reflection probability for an unpolarized current. For a fully polarized current, the same formula can be used by replacing A_{u} and B_{u} with A_{p} and B_{p} respectively. A_{p} and B_{p} are respective probabilities for a fully spin polarized Fermi surface of the non-superconducting electrode forming the point contact. The subscripts u and p denote the coefficients for the unpolarized and

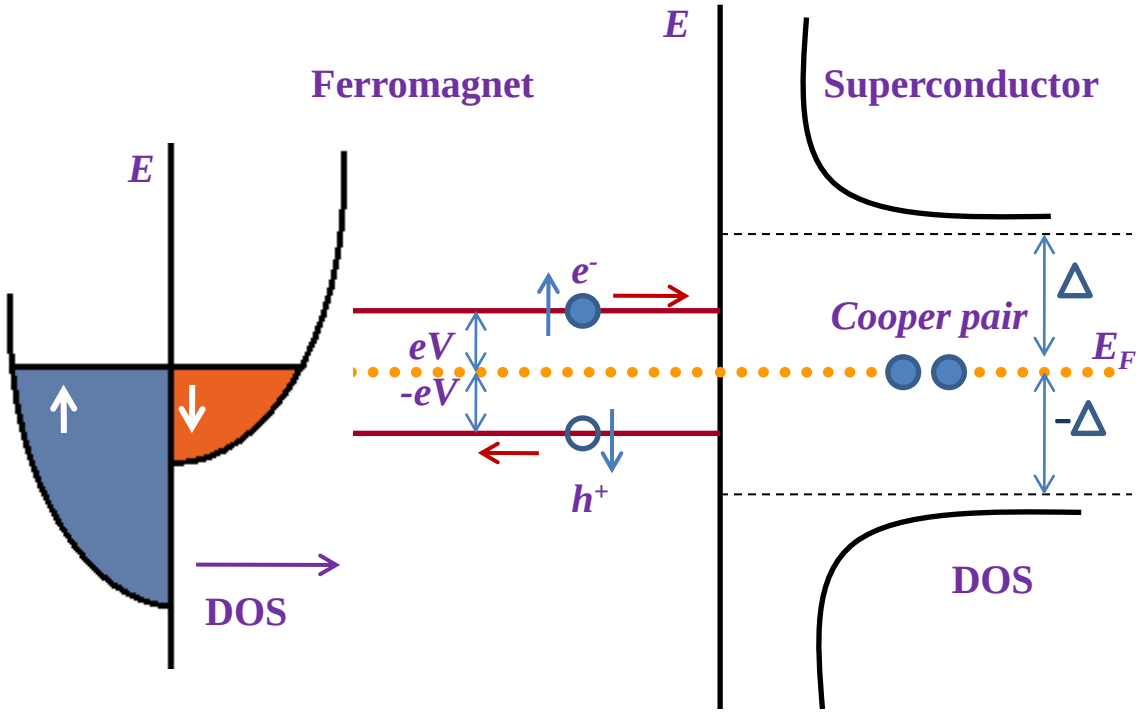

Figure 1.8: A schematic showing the Suppression of Andreev reflection in a point-contact between a ferromagnetic system and a superconductor.

polarized current respectively. $A_{\mathrm{u}}(E)$, $B_{\mathrm{u}}(E)$, $A_{\mathrm{p}}(E)$ & $B_{\mathrm{p}}(E)$ were calculated using the following formula:

For the entire range of E:

$$A_{\mathrm{p}}(E) = 0 \tag{71}$$

$$B_{\mathrm{p}}(E) = 1, \quad for E < \Delta \tag{72}$$

$$B_{\mathrm{p}}(E) = \frac{(\sqrt{\frac{E^2-\Delta^2}{E^2}} - 1)^2 + 4Z^2(\frac{E^2-\Delta^2}{E^2})}{(\sqrt{\frac{E^2-\Delta^2}{E^2}} + 1)^2 + 4Z^2(\frac{E^2-\Delta^2}{E^2})}, \quad for E > \Delta \tag{73}$$

$$A_{\mathrm{u}}(E) = \frac{\Delta^2}{E^2 + (\Delta^2 - E^2)(1+2Z^2)^2}, \quad for E < \Delta \tag{74}$$

$$A_{\mathrm{u}}(E) = \frac{(uv)^2}{\gamma^2}, \quad for E > \Delta \tag{75}$$

$$B_{\mathrm{u}}(E) = 1 - A(E), \quad for E < \Delta \tag{76}$$

$$B_{\mathrm{u}}(E) = \frac{(u^2 - v^2)^2 Z^2 (1 + Z^2)}{\gamma^2}, \quad for E > \Delta \tag{77}$$

where

$$\gamma^2 = ((u^2 - v^2)Z^2 + u^2)^2, \tag{78}$$

$$u^2 = 1 - v^2 = 1/2[1 + \sqrt{\frac{E^2 - \Delta^2}{E^2}}] \tag{79}$$

$$Z = \frac{V_0}{\hbar v_F} \tag{80}$$

After calculating the I_{u} and I_{p} we have simply written the total modified current including the transport spin polarization P_{t} as

$$I_{\mathrm{mod}} = (1 - P_{\mathrm{t}})I_{\mathrm{u}} + P_{\mathrm{t}} I_{\mathrm{p}} \tag{81}$$

The derivative of I_{total} with respect to V gives the modified Andreev reflection spectrum with finite spin. This model is used to analyze the spin-polarized Andreev reflection spectra obtained between a ferromagnetic metal and a superconductor by using four fitting parameters Z, Δ and Γ and P_t. It should be noted that for the measurement of the spin polarization of ferromagnets usually standard conventional superconducting probes are used for which the value of Δ is known. In addition, in order to have superconductivity, Γ cannot be arbitrarily large with respect to Δ. Therefore, effectively only two parameters, Z and P_t, are tuned freely during the analysis of spin-polarized Andreev reflection spectra.

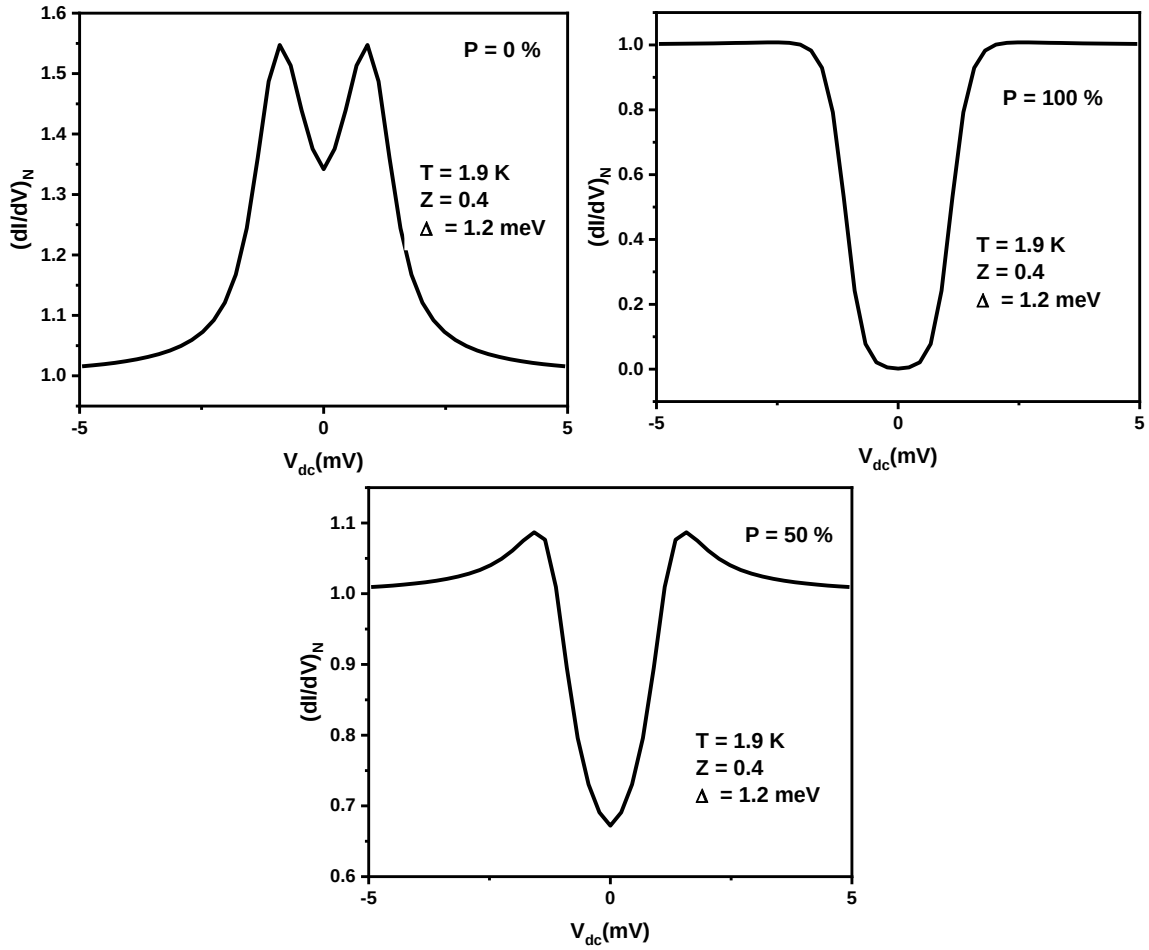

Figure 1.9: Various simulated curves obtained from modified BTK model with spin-polarization for P=0%, 50%, 100%.

The magnitude of spin polarization (P_t) thus determined may decrease monotonically with increasing barrier strength (Z). Such a dependence is seen routinely in spin polarization measurements using Andreev reflection spectroscopy and is attributed to spin-fip scattering processes taking place at mesoscopic interfaces with higher barrier strength. [49–51] For certain materials, however, where such spin-dependent scattering processes are not allowed, the dependence of P_t on Z may not be observed.

1.8 Spin polarization measurement in topological insulator

In order to measure spin-polarization of a toplogical we can use the same schematic as presented in Figure 1.8, here we just replace the ferromagnetic system with a topological insulator. In ferromagnets suppression of Andreev reflection occurs because of the pres-

ence of spin selective bands. However, in topological insulator the spin is in plane locked perpendicular to the momentum which causes a spin selective transport. Let us consider

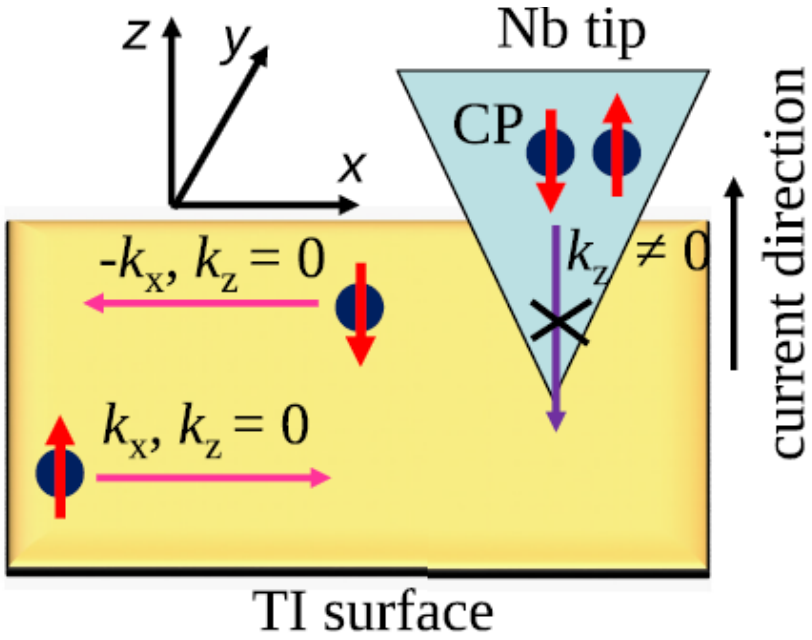

Figure 1.10: The electron injection process in point contact Andreev reflection. The electron spins of a topological insulator surface states are in plane locked perpendicular to the momentum. Cooper pairs with out-of-plane spin components are not allowed to be injected elastically in the TI surface states due to momentum conservation. Image ref. [52]

the injection is performed from a superconductor in the ballistic regime of point contact Andreev reflection as shown in Figure 1.10. Cooper pairs with spin along z can not get injected in topological insulators due to momentum conservation, hence the Andreev reflection is suppressed, and the contact shows high spin polarization. The measurement is a direct indication that the transport spin polarization is in plane.

1.9 Appendix

1.9.1 Why the carriers in the surface states of topological insulator have their spin locked at a right angle to their momentum?

When an electron with momentum $\vec{p}$ moves across a magnetic field $\vec{B}$, it possessses Zeeman energy $\mu_B \vec{\sigma}.\vec{B}$, where $\mu_B = 9.27 \times 10^{-27}$ is Bohr magneton and $\vec{\sigma}$ is the vector of Pauli spin matrices. Similarly, when this electron moves across an electric field $\vec{E}$, it experiences an effective magnetic field $\vec{B} \sim \vec{E} \times \vec{p}/mc^2$ in its rest-frame (c is the speed of light), a field that also induces a momentum-dependent Zeeman energy $\hat{H}_{so} \sim \mu_B(\vec{E} \times \vec{p}).\vec{\sigma}/mc^2$, called the spin orbit coupling. In crystals, due to broken inversion symmetry at the surface, electrons feel a electric field given by gradient of crystal potential,$E = -\vec{\nabla}V$. Considering the electric field to be $\vec{E} = E_z\hat{z}$. Then the spin orbit coupling energy is given by:

$$H_R = \frac{\alpha_R}{\hbar}(\hat{z} \times \vec{p}).\vec{\sigma} \tag{82}$$

The coefficient α_R is called the Rashba parameter [53] and is proportional to the strengths of the SOI and Ez.

The 3D TIs can be considered as a 2D surface states, and these surface states are characterized by Rashba SOC. Thus the mathematical expression for spin orbit coupling energy involves the vector product of velocity (or momentum) and the potential gradient. The momentum vector of surface Bloch states lies in the surface and the potential gradient points along the surface normal. Their vector product is a vector in the surface, perpendicular to the momentum vector. This is, why the spin direction of minimum energy is locked at right angle to momentum. As an example, If spin-up charge carriers are moving in the positive x-direction, then the spin-down charge carriers are bound to move in the negative x-direction, any mixture of these is prohibited. As a consequence, if any non-magnetic impurity falls on the way of the charge carriers, the spin has to flip in order to backscatter from the impurity state. The spin flipping is not allowed because it will

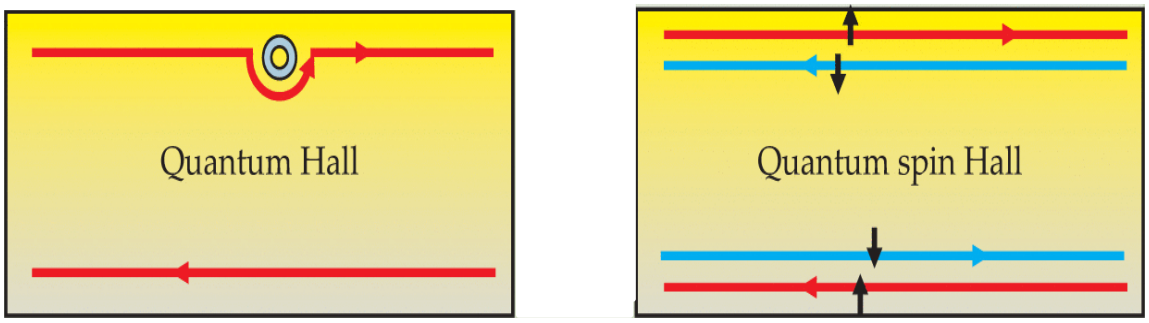

Figure 1.11: Spatial separation of charge/spin transport in the integer quantum Hall (IQH) and the quantum spin Hall (QSH) effects. Image ref. [30]

cost enormous amount of energy to reach at the another edge of the sample. Therefore, this property makes the motion of the charge carriers topologically robust.

2 Experimental details and Instrumentation

In this chapter, I will discuss the measurement technique that will be helpful in clear understanding of our experimental results. I have used mainly two experimental techniques, Scanning Tunneling Microscopy (STM) and Point-Contact Andreev Reflection Spectroscopy (PCAR). First, I will briefly go through the detailed description of Scanning Tunneling Microscope (STM) and then briefly explain the Point-Contact Andreev Reflection Spectroscopy (PCAR).

2.1 Scanning tunneling microscope (STM)

STM is the most powerful technique to study the physics of low energy excitations in the condensed matter systems. The scanning tunneling microscope (STM) was invented by Gerd Binning and Heinrich Rohrer at IBM Zurich in 1981 [54] and they were given Nobel Prize in Physics in 1986. This invention changed the standard of research completely in experimental condensed matter physics. STM provides the ability to see the topographic features of materials at angstrom level and the ability to resolve the electronic information at meV level. It is based on the phenomenon of quantum mechanical tunneling. Atomically resolved images can be obtained using STM. If the tunnel junction has a barrier width 'd' , then the expression for tunneling current is given by

$$I \propto \exp^{-2kd} \tag{83}$$

,

where k is given by the expression

$$k^2 = \frac{2m}{\hbar^2}(U_0 - E) \tag{84}$$

Here E is the total energy of the particle, and U_0 is the barrier height.

The tunneling current decreases exponentially with distance. Due to this exponential

dependence on the distance, the vertical resolution of STM is quite high.

2.2 STM Working

Scanning in STM mainly requires a tip and a sample. In order to have tunneling, the tip should either be metallic or semiconducting. The tip is brought closer to the sample upto few angstroms so that it lies in the tunneling regime. This can be done with the piezoelectric Z- positioner. In order to approach the tip towards the sample, we apply a bias to the sample with respect to the tip (say 800 mV) and set a current value (say 300 mA) and measure this current through an ammeter. When the tip and sample are far away from each other, it is not possible to get a current of 300 mA. Hence, the tip (sample) is taken closer to the sample (tip) by applying a high voltage to a piezoelectric Z – positioner which works in a slip- stick mechanism [55]. The current amplifier is connected to the positioner through a feedback loop where it measures a current and a bias is applied continuously until the set current is reached. XY - positoners are also attached to move the sample in x and y directions. The tip is embedded in the piezoelectric tube scanner which can be used to scan the sample once the tip is approached. The tube is divied into four quadrants and each of the vertical opposite quadrants is connected to a voltage source. One can bend this piezolelectric tube in any direction by applying a combination of voltages. Further, scanning of the sample can be done in two ways:

1) Constant height mode: In this mode of scanning in STM, the height between the sample and tip is fixed and the current varies according to the height of the surface. The variation in current as a function of position reveals the topographic features.

2) Constant current mode: Here the set point is current. In this mode, the feedback loop will try to maintain the current constant according to the topography of the sample by varying the height between the tip and sample.

The variation of current/height can be plotted at various points of the sample. The color variation of the plot gives the idea of the topography. However, we can obtain the sample topography using both the above methods. Depending on the surface of the sample

and apex of tip, one can get the atomically resolved images of the surface.

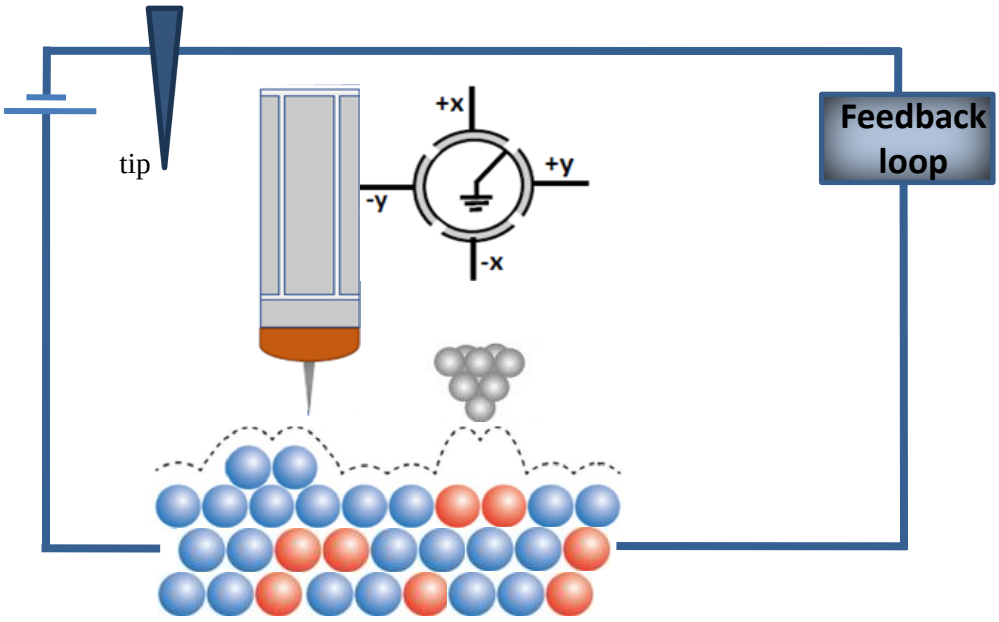

Figure 2.1: Scanning mechanism in a STM. A tube scanner with four major quadrants are shown.

2.3 Types of STM measurements

At cryogenic temperature the tunnelling equation can be written as

$$I_T \approx \beta \, |T|^2 \int_0^{eV} N_S(E) dE \tag{85}$$

where, $N_S(E)$ is the density of states of the sample. Typically, PtIr or W tips are used in the STM measurements and the density of states of tip is considered to be constant around the Fermi level. $|T|^2$ is a phenomenological tunneling matrix element.

2.3.1 Topography:

As we already know, STM can be used to obtain the topography of the surface of a sample. The defect and impurity states can be easily observed on the sample surface. The tunneling current is dependent on the density of states (DOS) of the sample and the barrier height. Purely geometric surface topography can be obtained for samples having homogeneous DOS, While geometric surface plus charge density wave (CDW) can be obtained for heterogeneous DOS samples.

2.3.2 $dI - dV$ spectroscopy

STM can also be used to acquire LDOS upto several electron volts other than the sample topography. By fixing the distance between the tip and sample and turning off the feedback, dI/dV vs V can be measured which gives the local density of states of occupied as well as non occupied states with respect to energy.

$$dI/dV \propto N_S(E) \tag{86}$$

Here $N_S(E)$ is the local density of states.

2.3.3 $dI - dV$ mapping

As we can measure the LDOS at one point, it is also possible to measure the LDOS at each and every point in a given scan area. After obtaining the LDOS at every point on the scan area, one can slice the dI/dV at a particular energy (bias). From this data, we can get the LDOS in the real space directly.

2.4 STM at IISER Mohali

The STM was bought from UNISOKU (model 1300) equipped with a JANIS-He^3 cryostat. The STM measurements can be done at 300 mK in (10^{-10}mbar) upto 11 T magnetic field along the z-axis with 4G magnet controller.

2.4.1 Chambers in STM

The complete set up consists of a load lock chamber, preparation chamber, an exchange chamber and a STM chamber arranged respectively. All the chambers have a VAT valve between them which seperates one chamber from the other and maintined in UHV at all times other than the load lock chamber. The load lock chamber is used to mount a new sample or a new tip and it is exposed in the air. The load lock chamber is first pumped

Figure 2.2: (a) STM setup along with power supply rack in our lab. (b) shows 1 K pot and He^3 pot and a scanning stage hanging from the end of the insert with metal springs at low temperature. (c) Charcoal pump

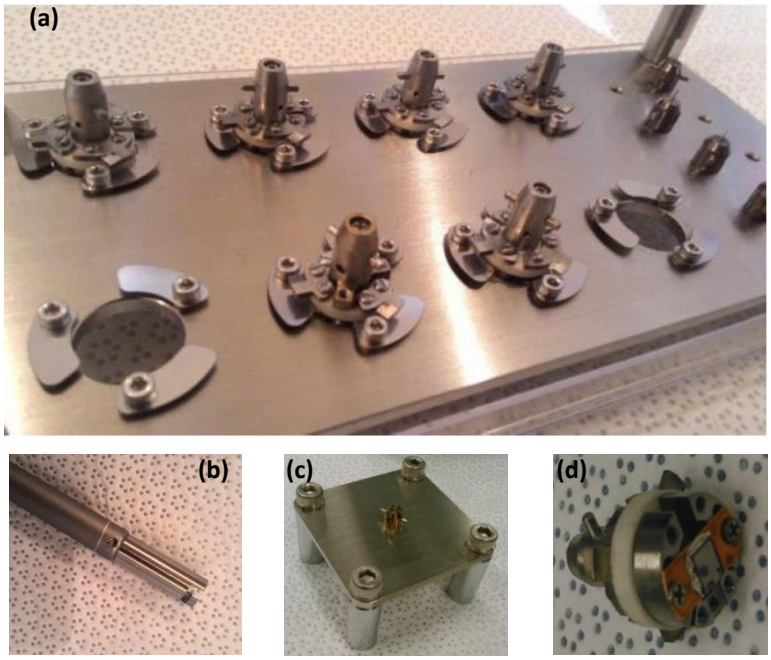

Figure 2.3: (a) Sample holders (b) Mounting tool (c) Tip holder (d) Sample holder

down to 10^{-8} mbar with an Edwards nEXT- 300 turbo molecular pump (TMP) before opening the gate valve between load lock chamber and preparation chamber.

We can clean, prepare and characterize a sample in preparation chamber. This chamber (preparation chamber) contains a tip heating facility, two thermal evaporators (K-shell) with low-temperature surface treatment facility on a sample, one Argon reverse sputtering system, reflected high energy electron diffraction (RHEED), low energy elec-

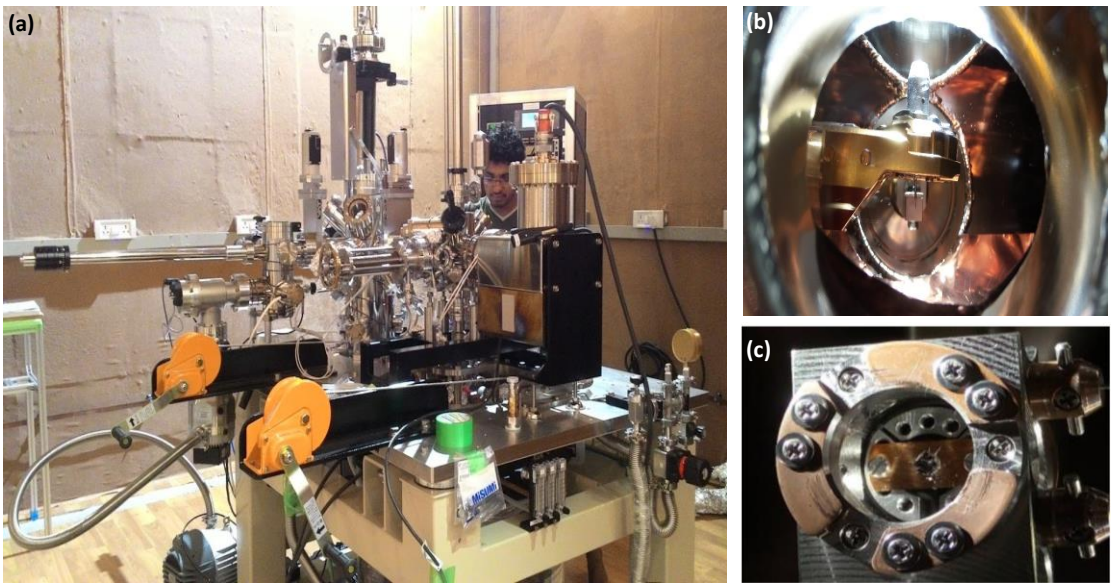

Figure 2.4: (a) A view of STM from a different angle (b) Cleaving stage (c) Cleaved sample

tron diffraction (LEED), and an auger electron spectroscopy (AUS).

LEED facility in STM: Low energy electron diffraction(LEED) is one of the various ways to characterize the surface of the sample. In this technique, collimated electron beam is generated by the low energy electron gun and this electron beam is made to fall normally on the surface of a single crystal. If the sample is clean enough, a diffraction pattern is observed which can be detected by a detector placed behind the source. To observe the diffraction, the sample must be properly grounded otherwise there can be charge accumulation and this accumulation of charge can scatter the electron beam. This accumulated charge can be transferred to ground if the sample is grounded.

The exchange chamber consists of a large manipulator to transfer the tip holder and sample and has sample cleaving facility as well. Infact, all the chambers have UHV magnetic manipulators for transferring of tip and sample holder from one chamber to the other.

2.5 Vibration isolation

The most important part for working of STM is the vibration isolation. All types of noise (vibrational, electromagnetic and acoustic) must be completely isolated from the scanning space. At IISER Mohali, we build a huge concrete pit in a seperate building for STM. The

pit was properly isolated in all sides from the rest of the building in order to avoid any kind of vibration. Aluminium rods of 1 inch diameter were used in concrete block. All the chosen components are non magnetic as cryostat has a high field magnet installed in it. In order to avoid electromagnetic and acoustic noise, we have a Faraday cage along with the acoustic isolation. For ground loop noise, we have made separate grounding pits for the electronic measurements having a ground line resistance of < 2ohm.

2.6 Tip preparation

In order to get an atomic resolution image, apex of the tip plays a vital role. The most widely used tip in STM is of Tungsten (W) as it is easy to etch the tungsten wire and its density of states is flat near the fermi energy. We use electrochemical etching for the formation of STM tips.

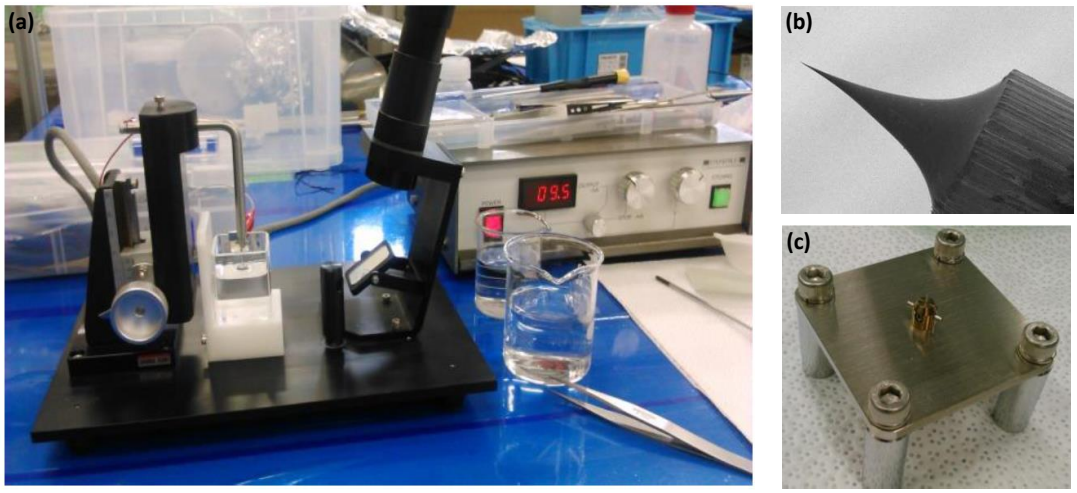

Figure 2.5: (a) Tip preparation setup (b) A processed tip image (c) Tip holder.

In this process, we use an electrolyte which can be either KOH or NaOH and out of the two electrodes, one is connected to the tip and other one is Platinum ring. A voltage is applied between the tungsten wire and platinum ring. The submerged section near by meniscus is the most ablated region and the tungsten wire is very close to meniscus. The constriction point made by this erosive process gradually becomes thin. Finally, the part of the tungsten wire under the constriction point falls off and the edge of tungsten wire

becomes very sharp.

In general, the tungsten (W) wires of diameter 0.5 or 1 mm is cut into small pieces and rubbed with a P8000 grade sandpaper to remove the oxide layer and then these wires are cleaned with ethanol and make one tungsten wire fixed on one of the electrodes. Keep two separate beakers of ethanol and distilled water ready before starting the process. A 1.2 N solution of KOH/NaOH is prepared and both the electrodes are inserted into the solution. Then apply a bias of 10 V and set a current of 1 mA. A current feedback circuit is used to automatically break the circuit once the set value of current is reached. Once the etching is complete, an alarm rings to alert and the tip is taken out from the electrode and dipped instantly in distilled water for 30 seconds, then it is dipped in ethanol to avoid formation of oxide layer on the freshly etched tip. Then, we look at the apex of the tip through the optical microscope. Once the good apex is confirmed, the tip is mounted on the tip holder and immediately transferred to the UHV chamber. In this chamber, we have another tip heating facility for modifying the tip apex by heating it.

2.7 STM measurements

All of these measurements are done with UNISOKU - 1300 system. All the noises have been isolated from the STM chamber in some ways; to remove the electrical noise, we need good electronics. The interfacing is done with a R9 controller from RHK technology. We have four lock-in amplifiers (0-100 kHz), several voltage sources (-10 V to 10 V), high/low pass filters, two PLLs, twenty DACs, spectrum analyzers and four digital oscillators. The R9 controller is interfaced with IHDL icon-based program language.

In principle, it is easier to measure voltage than current, but here we apply voltage between tip and sample and measure the current. For this, we have Femto DLPCA-200 current amplifier (gain from 10^3 to 10^{11} V/A, input noise down to 4.3 fA/$\sqrt{Hz}$). This also helps in reduction of noise in the feedback signal. To reduce the high frequency noise in the input signal, we make use of a high voltage filter from UNISOKU having cut off frequency 530 kHz. A second stage voltage pre-amplifier (R9 IVP preamp) is

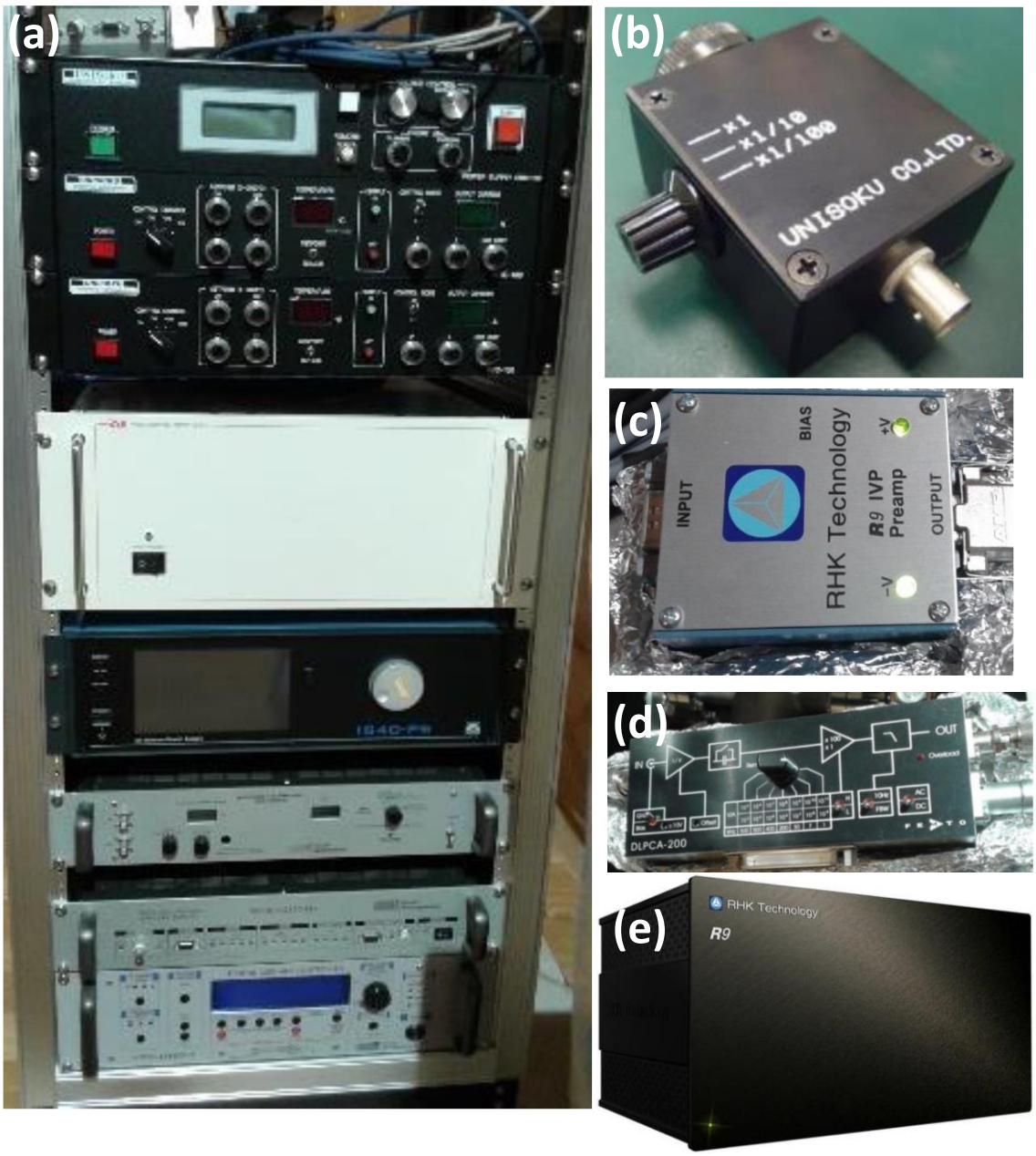

Figure 2.6: (a)(Top to bottom) RHEED controller, RHEED control power supply, Ion source power supply, LEED power supply, LEED controller(b)voltage divider (c) preamplifier (d) DAC (e) R9 STM controller

also used to the input signal. The approach mechanism is controlled using PMC100 from RHK technology interlocked with the R9 controller in order to automatically control the approach mechanism by the interface program. For high signal to noise ratio, several filters are used before all the input lines.

The resolution of R9 controller is 24 bit. The applied voltage should be less than the superconducting energy gap during the spectroscopic measurement on a low-tempertaure

superconductor. As the bit size of the controller is fixed, therefore, for high resolution, a voltage divider down to 1/100 during spectroscopy is used at low bias.

As the tip and the sample in the STM geometry do not touch each other, it works as a capacitor, and for AC signal one must take care of the phase of the input and output signal. To do this, we need a lock-in amplifier. We can measure the first harmonic with a lock-in amplifier, which is phase sensitive, without losing any information. The signal locked at first harmonic is proportional to dI/dV, it can be shown through Taylor's expansion: $I(V = V_{dc} + V_{ac}cos\omega t with V_{dc} \gg V_{ac}) = I(V_{dc}) + \left(\frac{dI}{dV}\right)|_{V_{dc}} V_{ac}cos\omega t + \frac{1}{2}\left(\frac{d^2I}{dV^2}\right)|_{V_{dc}} (V_{ac}cos\omega t)^2 + \cdots = I(V_{dc}) + \left(\frac{dI}{dV}\right)|_{V_{dc}} V_{ac}cos\omega t + \frac{1}{4}\left(\frac{d^2I}{dV^2}\right)|_{V_{dc}} (V_{ac})^2(1 + cos2\omega t) + \cdots$

For the LDOS mapping, we perform imaging and spectrscopy both but one at a time by choosing image + spectroscopy option. During imaging, feedback is turned on, while switched off during spectroscopy measurements.

Time duration for a LDOS map in a given area depends on the selection of the pixel size and sampling time. However, it is also possible to do LDOS map at certain energy by adding a low AC signal to the tip-sample bias voltage and do imaging only, this requires much less time. Here, it is important to note that in this process the feedback remains turned on. Therefore, any signal which is comparable to the topographic signal can not be resolved here.

2.8 Point contact spectroscopy measurements

Point-contact spectroscopy (PCS) is a very powerful technique to study the behaviour of a electron in metals [56, 57], superconductors, ferromagnets [48, 50, 58, 59] and topological insulators [52]. etc. There are several techniques to do point-contact spectroscopy like needle-anvil [60], shear method [61] and lithographic method [62]. I have used Needle-anvil method to make a point-contact as shown in Figure 2.7. In Needle-anvil method, a specially processed metallic electrode in the form of thin needle (made by mechanical cutting of wire), is slightly pressed against the flat surface of another electrode by a differential screw, which is connected to a stepper motor from outside the cryostat. We use a

home-built point contact spectrscopy probe to carry out the measurements. The lower part of the point-contact probe is made of brass in cylindrical form. Within the brass cylinder there is a differential screw, which is used to change the contact size, and a Teflon material, with which the tip holder is connected.

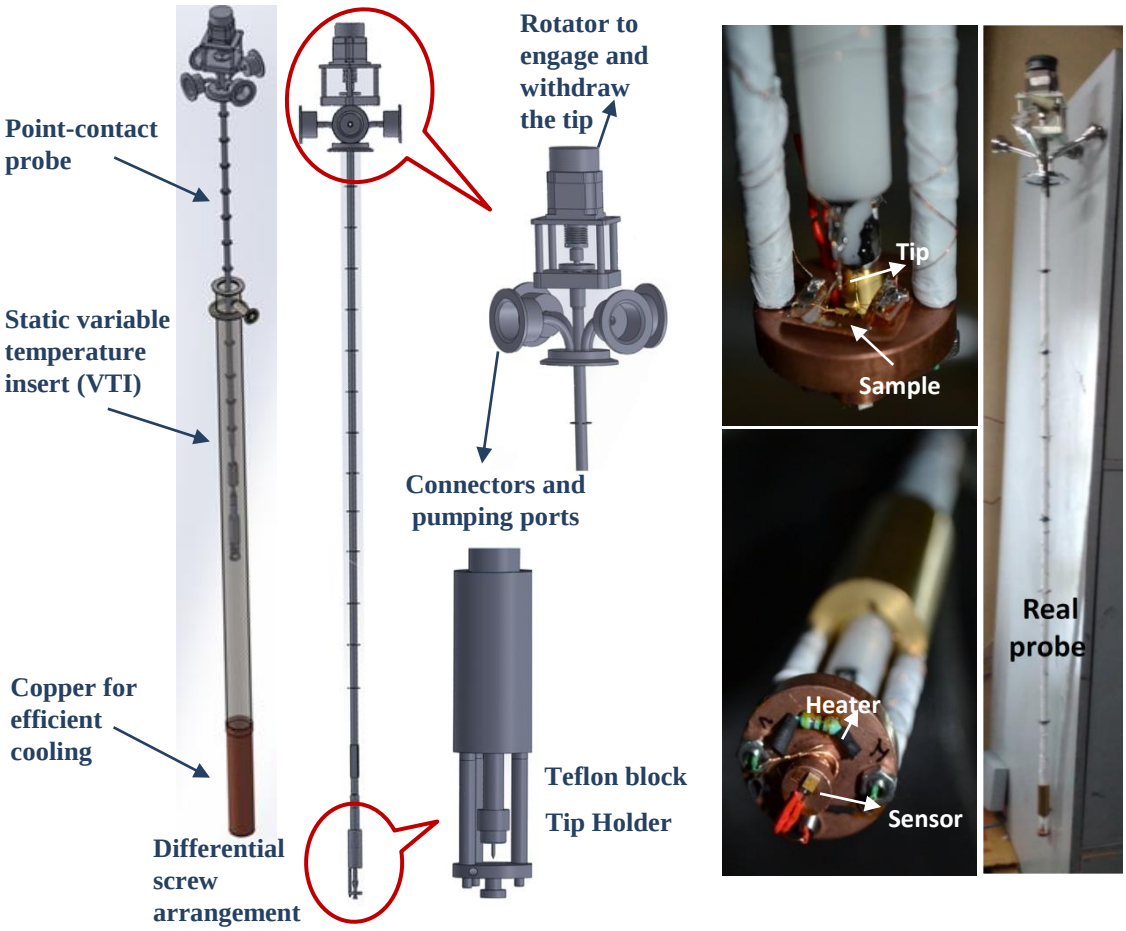

Figure 2.7: An image of a home-built point-contact probe with zoomed in view of different parts of the probe.

The system to be studied is mounted on copper disc (sample holder) in PCS probe. A calibrated cernox thermometer and a heater (a 50 Ω Nichrome wire) were attached to the same copper disc for precise measurement of the temperature and for controlling the sample temperature during the PCS measurements. Two 100 micron thick gold wires are mounted on the sample using silver epoxy as a conductive glue, for transport measurements. The superconducting tips are fabricated from 250 micron thick conventional superconducting wires (I used Nb in my experiments). Then the tip is mounted on a teflon piece connected with head of a differential screw. The differential screw is threaded to a

cylinder in such a way that its one end is attached to a block and other end is attached to shaft inside the cylinder. The block moves forward and backward, when we use rotator to move the screw through the shaft. That block is attached to a teflon piece to which tip is fixed. This differential screw has 100 threads per inch. Then two more 100 micron thick gold wires are fixed on the tip for transport measurements. 250 micron thick twisted pair of copper wires are used for the connections from the top to the sample space. As the measurements are going to be performed at liquid He temperature, one should block the radiation from the outside. In order to block the radiation, we use multiple copper radiation baffles on the probe.

The probe is then inserted inside the static variable temperature insert (VTI) of a liquid-helium cryostat. The static VTI is first evacuated and then filled with exchange (dry helium) gas to cool down the sample area. The bottom part of the static VTI is made of copper for efficient cooling. The static VTI is surrounded by a dynamic VTI with a micro-capillary that allowed us to perform measurements down to 1.4 K. This whole assembly of VTIs and probe is designed to be operated in an American magnetics cryostat. The whole assembly goes inside the liquid Helium cryostat. The cryostat is equipped with a three axis vector magnet which can apply a maximum magnetic field of 6 Tesla along the vertical direction using a superconducting solenoid and 1 Tesla in the horizontal plane using four superconducting Helmholtz coils with AMI (American Magnetics, Inc.) controller.

A lock-in modulation technique is employed to obtain the point contact spectra i.e. dV/dI vs. V data, where a dc current(sweeping current) is coupled with a small current drawn from the sinusoidal output of a digital lock-in amplifier (Stanford Research Systems, model: SR-830) through a passive current source (a pomona box is used). The ac component of the input current should not be very high since this voltage determines the resolution of the measurement technique. This current is typically set such that the first harmonic response of the lock-in is roughly only 1% of the voltage scale of interest $i.e.$, for a PCAR experiment, since the superconducting gap is typically few millivolts, the

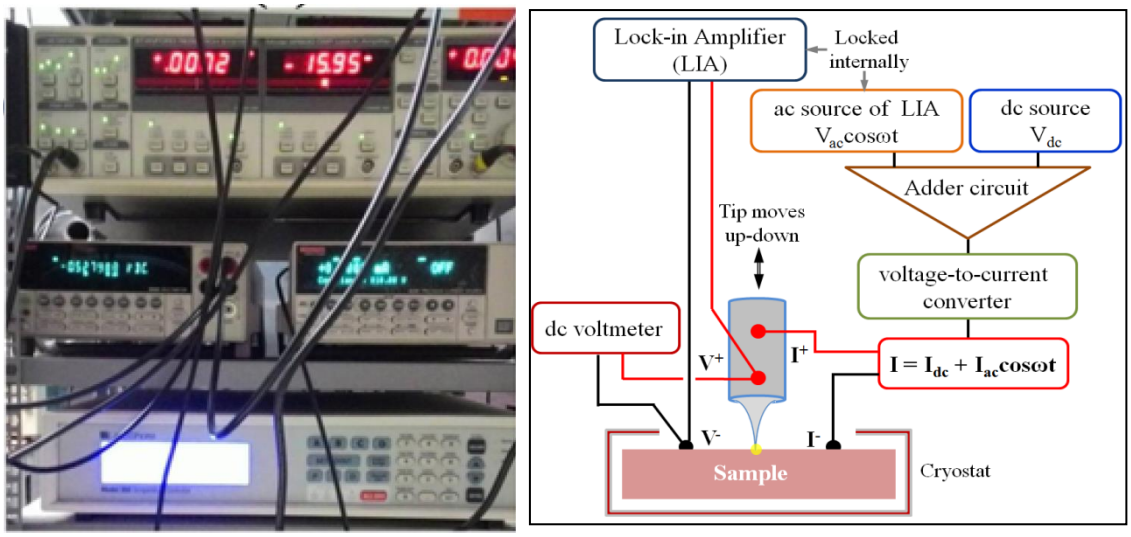

Figure 2.8: Electronics and schematic diagram of lock-in modulation technique used in point contact spectroscopy measurements.

lock in response should be of the order of few micro volts. A modulated current is passed through the point-contact. The dc component of voltage drop across the point contact is recorded by a digital multimeter (Keithley 2000) while the ac component is measured by the same lock-in amplifier. The differential resistance dV/dI (proportional to the ac output voltage locked externally at the first harmonic) is measured by a lock-in amplifier. The signal locked at first harmonic is proportional to dV/dI. It can be shown through Taylor's expansion:

$$V(I = I_{dc} + I_{ac}cos\omega t) = V(I_{dc}) + \left(\frac{dV}{dI}\right)|_{I_{dc}} I_{ac}cos\omega t + \frac{1}{2}\left(\frac{d^2V}{dI^2}\right)|_{I_{dc}} (I_{ac}cos\omega t)^2 + \cdots =$$
$$V(I_{dc}) + \left(\frac{dV}{dI}\right)|_{I_{dc}} I_{ac}cos\omega t + \frac{1}{4}\left(\frac{d^2V}{dI^2}\right)|_{I_{dc}} (I_{ac})^2(1 + cos2\omega t) + \cdots$$

A Model-350 temperature controller from Lakeshore Inc is used to monitor and control the sample temperature. The data acquisition is done through GPIB connection and the measurement is made completely automated (using a lab-view programme developed in our lab).

3 Generation of strain induced pseudo-magnetic field in a doped type-II Weyl semimetal

It is not obvious to relate an equation from the context of high energy and particle physics to current research in condensed matter physics. Weyl fermions are well known in quantum field theory for so long, but could not be observed as a fundamental particle in nature. Recently it has been seen that a Weyl fermion emerges as a quasiparticle in certain crystalline materials. Weyl fermion was missed by Weyl in 1929 due to its breaking of the stringent Lorentz symmetry of high-energy physics. Lorentz invariance however is not present in condensed matter physics. The concept of quasiparticle arises when the real electrons interact with the crystal or among one another. Although the realization of Weyl fermions as quasiparticles in crystals was proposed a long ago, but it was considered recently followed by many theoretical proposals on material realizations. These materials are shown to be Weyl semimetals. A wide variety of exotic physical phenomena predicted several decades ago in the context of high energy physics have finally been observed in Weyl semimetals [63–70]. One such example is the so called chiral anomaly which is observed through transport measurements when both electric and magnetic fields are applied to the material [71–75]. Realization of Weyl physics in solid state systems has also paved the way for realization of even more exotic phenomena that are rather uncommon in high energy physics. One particular example is the generation of an axial gauge potential, experimental investigation of which is known to be an extremely complex problem in high energy physics whereas, a synthetic gauge potential is expected to be easily obtained in strained Weyl semimetals [74, 76]. Such an axial gauge potential, unlike the usual electromagnetic gauge potential A, is an observable as it can give rise to pseudo-electromagnetic fields which interact with fermions of opposite chirality in a Weyl semimetal. Recent theoretical proposals suggest that a pseudo-magnetic field generated by strain in a Weyl semimetal may give rise to the formation of quantized Landau levels and quantum oscillations even in absence of an externally applied magnetic field [77–82]. However, in

contrast to it's numerous theoretical predictions, the experimental demonstration of the pseudo-magnetic field in Weyl semimetals has been extremely limited. We observe the evidence of an intrinsic strain-induced pseudo-magnetic field in Re doped $MoTe_2$. This effect was earlier observed by scanning tunneling spectroscopy in graphene, a 2D Dirac material, at localized nano-bubbles under strain. A great variety of unique properties like quantum hall effect, magneto-electric effect can be realized in topological systems in the presence of an externally applied magnetic field. Thus, synthetic generation of an intrinsic magnetic field in Weyl semimetals can, in principle, make their implementation possible in new generation technology and fundamental research.

In this chapter, I will present the first experimental evidence of an intrinsic strain-induced pseudo-magnetic field (3 Tesla) over a large area in a three-dimensional, type-II Weyl semimetal $MoTe_2$ doped with Re through scanning tunneling microscopy and spectroscopy down to 300 mK. I will show the formation of Landau levels at zero applied magnetic field in intrinsically strained crystals of Re-$MoTe_2$ which confirms an intrinsic pseudo-magnetic field in the system.

3.1 First experimental evidence of pseudo-magnetic field

However, many theoretical proposals suggests the possibility of inducing a large pseudo–magnetic field in graphene [83] in the past, but it could not be found experimentally. It has been revealed recently through scanning tunneling spectroscopic experiments that highly strained nanobubbles of graphene (formed during growth of graphene) on a platinum (111) surface, corresponds to Landau level formation owing to an extremely high pseudo-magnetic field of the order of 300 Tesla [12]. Inspired by such report, we chose Re doped $MoTe_2$, which has linearly dispersive bands similar to graphene, for such an experiment. The motivation behind choosing Re doped $MoTe_2$ for our experiment is (i) It is a Weyl semimetal which have linearly dispersive bands. (ii) Topographic ripples formed due to strain were earlier observed in strained single crystals of Bi_2Te_3 [84], so we chose a telluride for our experiment. In our single crystals, the strain was possibly induced either

during crystal growth or during cleaving and the STM topographs clearly show long range periodic topographic ripples formed due to the strain as reported in strained single crystals of Bi_2Te_3 [84].

Now, I will discuss about the type-II Weyl semimetal.

3.2 Weyl semimetal

We have discussed about Weyl semimetal in chapter 1, Weyl fermions at zero energy correspond to points of bulk band degeneracy, known as Weyl nodes, associated with a chiral charge that protects gapless surface states on the boundary of a bulk sample. Fermi arcs are the surface states connecting the projection of bulk Weyl nodes in the surface Brillouin zone. Weyl semimetal can be classified into two types; Type I Weyl semimetal and Type II Weyl semimetal.

3.3 Classification of Weyl semimetals

As we have discussed in chapter 1, perturbations can only shift the position of the Weyl point in momentum space, but can not remove the Weyl point locally. However, the cones can be tilted and may even tip over. In high energy physics, the light cone (counter part of Weyl cone in space-time), in principle, can be tilted by the Gravitational field of a massive object. But for the relativistic Weyl cone such a distortion is forbidden by particle-hole symmetry, however, that is not a fundamental symmetry in condensed matter. Weyl cones can be divided into two topologically distinct types depending on the degree of tilt. In type I Weyl semimetal, the cone is only weakly tilted so that the electron-like states and hole-like states occupy separate energy ranges, above or below the Weyl point. In type II Weyl semimetal, the cone has tipped over so that electron and hole states coexist in energy. We can also talk about this classification of Weyl semimetal on the basis of fermiology and whether the Lorentz symmetry is respected or not: Type-I Weyl Semimetals have point-like bulk Fermi Surfaces formed solely by Weyl Points that approximately respect the Lorentz symmetry whereas type-II Weyl Semimetals break the Lorentz symmetry and

have finite electron density of states at the Fermi energy. Recently, type-I topological Weyl semimetals have been discovered in the (Ta, Nb) (As, P) family of compounds.

Hamiltonian for a type-II Weyl semimetal is given by:

$$H = d_0(\mathbf{k}) I_{2\times 2} + \sum_{\mu=1}^{3} d_\mu(\mathbf{k}) \sigma_\mu \tag{87}$$

where σ_μ are the 2-component Pauli matrices, and d_μ are their anisotropic coefficients. Here the k-dependent term $d_0(k)$ in the Hamiltonian can add interesting modification to the Weyl bulk spectrum. In absence of any k dependence, the density of state at the node energy, is vanishingly small point and the Fermi surfaces are just discrete Weyl points whereas an adequate k dependence can tilt the Weyl cones creating electron and hole pockets at the node energy. Or in other words, the key difference between the type-I and type-II Weyl Hamiltonians arises from the onsite dispersion d_0 which is even and odd under inversion with respect to the Weyl points in the two cases, respectively. For a type-II system, this odd parity is responsible for tilting of the Weyl cone thereby giving rise to unique quantum properties.

In type I Weyl semimetal, there are zero density of states at the Weyl node, whereas type II Weyl semimetal supports Fermi pockets at node energy. The one phase transits to the other one via a Lifshitz transition.

Type-II Weyl fermionic systems are predicted to inherit a set of unique peculiarities in response to a magnetic field due to the tilting of the Weyl dispersions [85]. We chose Re-doped $MoTe_2$ for our experiment, which is a type-II Weyl semimetal, let us first discuss about $MoTe_2$.

3.4 $MoTe_2$: A type-II Weyl semimetal

The exotic quantum properties of transition metal dichalcogenide (TMDs) have gained research interest in recent years. TMDs family members are predicted to exhibit various topological states of matter.

$MoTe_2$ is an interesting member of transition metal dichalcogenides as it exists in multiple structural phases [86, 87]. $MoTe_2$ is generally studied in the most stable hexagonal (2H) phase. However, experiments revealed another layered crystal structure in $MoTe_2$, the monoclinic ($1T^{'}$) phase. Unlike the semiconducting 2H phase, the semimetallic or metallic $1T^{'}$ phase of $MoTe_2$ retain inversion symmetry. Structural phase transitions in transition metal dichalcogenides can be induced by thermal means or chemical means. At 250 K, $MoTe_2$ shows a structural phase transition where a high temperature inversion symmetric monoclinic phase finds a new ground state with non-centrosymmetric orthorhombic structure (space group: $Pmn21$, T_d Phase) [88]. $MoTe_2$, along with its various structural phases, it displays variety of intriguing physical properties including Weyl physics. The Orthorhombic T_d phase is a Weyl semimetal [89, 90] which is also known to show superconductivity below a very low critical temperature (T_c) of 0.1 K in its pristine form [91].

The dynamic control of transitions between the 2H, $1T^{'}$ and T_d phases can reveal the competition, coexistence and cooperation of different crystal structures, as well as interplay among distinct physical properties. Such control also leads to broad device applications such as memory devices, reconfigurable circuits and topological transistors.

It is also possible to enhance the T_c of $MoTe_2$ by introducing strain in the system through any means whether by applying external pressure or by chemical means (doping). By introducing strain in the crystals of $MoTe_2$ through large external hydrostatic pressure, the T_c of $MoTe_2$ can be enhanced significantly. Recently it was shown that the same high T_c phase of $MoTe_2$ can also be achieved by doping the Mo-sites of $MoTe_2$ with Re [92]. At 30% Re doping, $MoTe_2$ shows a dramatically increased transition temperature as high as 4.1 K at ambient pressure [92]. While the mechanism through which the enhancement of T_c in Re-$MoTe_2$ occurs is not understood as of now, from the similarities of the results with those obtained under high pressure, it is rational to consider chemically induced internal strain as one of the highly probable mechanisms.

If the lattice gets strained by some means, it should be possible to explore a wide

variety of (strain induced) phenomena discussed in the domain of quantum field theory [93,94]. As we will discuss below, our STM topographs reveal that the crystals are indeed under strain and generate a pseudo-magnetic field, the effect of which is also observed in our STM spectroscopy experiments. Let us first discuss the effect of strain and how to create strain in dichalcogenides.

3.5 Effect of strain

It has been seen that highly strained nanobubbles of graphene on a platinum surface induces an intrinsic pseudomagnetic field of the order of 300 Tesla and Landau levels are formed as a consequence of this pseudomagnetic field [95]. The ingredients to see such a effect in graphene are a linear band and a triangular symmetry without which the synthetic gauge field will not be able to give rise to pseudomagnetic field. The individual nanobubbles of graphene grown on Pt(111) often showed triangular shape.

A pseudomagnetic field can be realized in Weyl semimetals too, when there is an inhomogeneous strain in the system. Small mechanical strain in a Weyl semimetal can be described as an effective axial vector potential **A**. Due to inhomogeneous strain, there will be a spatial variation of the quantity **A** (vector potential corresponding to the pseudomagnetic field) in the system. This can give a pseudo-magnetic field as $\mathbf{B} = \nabla \times \mathbf{A}$. If **A** was spatially uniform, Curl of **A** would be zero and there would be no pseudo-magnetic field. The only quantity that can be as non-uniform as the strain itself is **A**. To summarise, in fact only **A** is expected to vary in sync with the variation of strain, but not **B**.

3.6 How to create such strain in dichalcogenides

The ripples could have formed due to strain developed either during crystal growth or during the cleaving of the crystals prior to STM experiments. Such stripy surface ripples emerging from strain were earlier observed on single crystals of Bi_2Te_3. In this paper, the authors clearly say that it is not explicitly clear which interactions might induce these features, a probable explanation is that the buckling occurs during sample growth or cleaving

due to strain. However, we have confirmed that the ripples are most probably formed during cleaving of the crystal at low temperature in UHV. In fact, arbitrary choice of cleaving temperature does not lead to the ripples—in our case, room temperature cleaving did not lead to clear ripples but cleaving at 80 K reproducibly formed the ripples. This itself is interesting and invites material science analysis of the surface. The experiment was done in collaboration with Anshu Sirohi and Aastha Vasdev. Now we will have a look on our experimental results.

3.7 Experimental details

High quality single crystals of Re dpoed $MoTe_2$ were used for all the measurements presented here. Single crystals of Re doped $MoTe_2$ were grown by the Chemical Vapor Transport (CVT) technique (see appendix). In the first step, pure phase polycrystalline samples of composition $Mo_{1-x}Re_xTe_2$ ($x = 0.2$) were prepared by the standard solid-state reaction process. The obtained pure polycrystalline samples were then used in the crystal growth process.

Scanning tunnelling microscopy is a surface sensitive measurement. Therefore, it requires an extremely clean surface. In order to achieve this, the single crystal was cleaved in UHV(10^{-11} mbar) by an $in-situ$ cleaver at liquid nitrogen temperature to get a pristine crystal surface.

Cleaving: There is a tungsten rod fixed on the top of the sample (can be seen in Figure 3.1) by silver epoxy which is very hard and covers the entire surface of the sample. This tungsten rod can be knocked out by hitting the manipulator from outside. When this rod is knocked out, some of the layers of the crystal also go off along with the rod, and a clean surface of Re doped $MoTe_2$ crystal is obtained.

In order to confirm the surface quality of the crystal first, we perform LEED measurement on Re doped $MoTe_2$. The low energy electron diffraction LEED pattern of $Re_{0.2}Mo_{0.8}Te_2$ single crystal is shown in Figure 3.2. The LEED pattern is a well ordered pattern implying high quality of Re doped $MoTe_2$. There are no extra features present

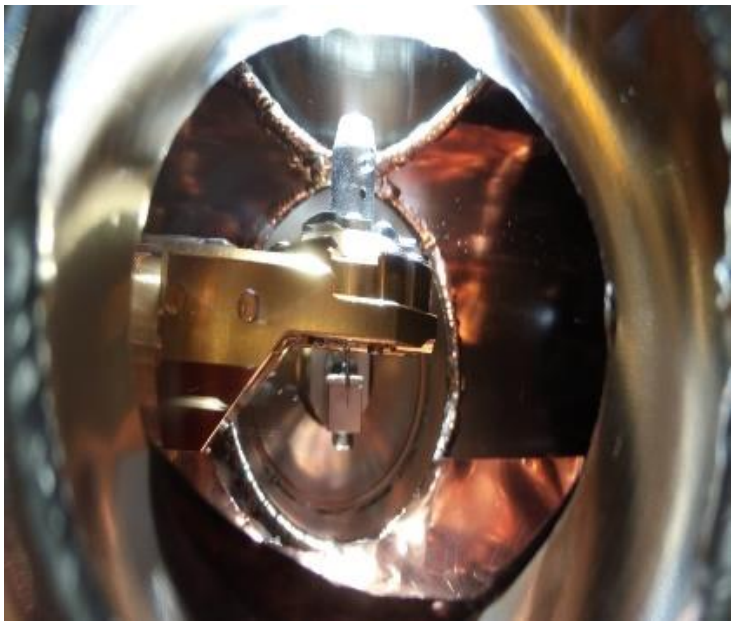

Figure 3.1: Cleaving stage in STM

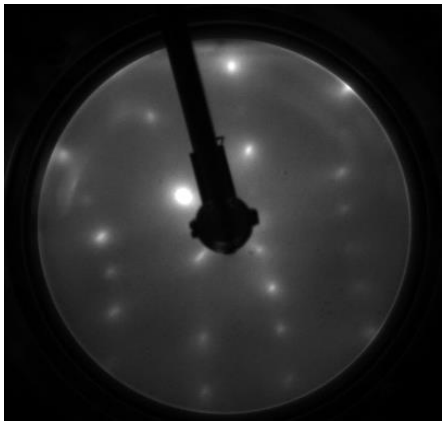

Figure 3.2: LEED pattern of Re doped $MoTe_2$.

due to any other impurities or clusters in the LEED patterns. After confirming the high quality of crystals, the crystal is transferred to the STM head using an ultra-high-vacuum manipulator, for scanning measurements. The crystal is placed on a scanning stage which hangs from the end of the insert with metal springs at low temperature. The sample is biased and the tip is virtually grounded through the current pre-amplifier.

As we discussed some of the layers of the crystal go off during cleaving the sample, while some of them relax back. When they relax back, they form a ripple structure.

This ripple structure can be clearly seen in the topography in STM. Figure 3.3 shows a large area (700 nm $\times$ 700 nm) STM topographic image of one part of the surface captured

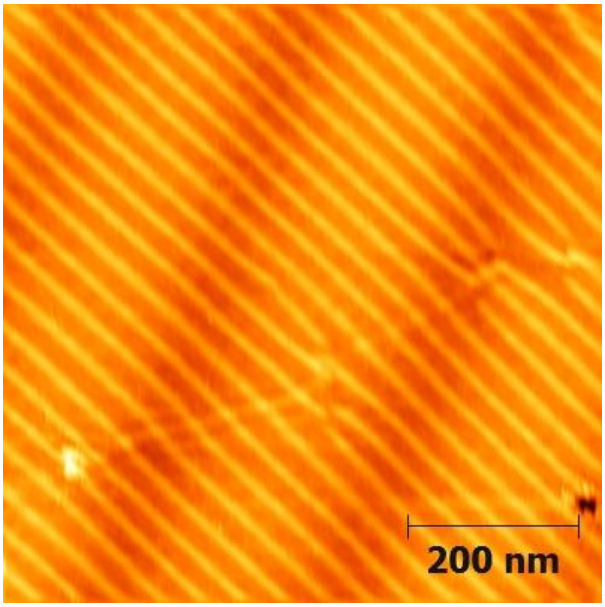

Figure 3.3: 2D picture of large area STM topograph of the cleaved surface of Re doped $MoTe_2$ obtained in a "high-strain" region.

at a temperature of 7 K. In this part, a large number of stripes are seen. The stripes occur periodically in real space with a distance between two consecutive stripes (modulation wavelength) of approximately 35 nm. On the other hand, a line profile [Figure 3.4(a)] drawn across the stripes shows a periodic height variation of the order of ~ 8 $\mathring{A}$ (Figure 3.4(b)). These observations confirm that the stripes are not due to an electronic order, but due to the formation of atomic scale topographic modulations (ripples) on the surface of the single crystals. We will show later that such areas are maximally strained and the effect of a pseudo-magnetic field is most prominent in such areas.

Now, when we go for a closer inspection of the area (Figure 3.4(a)), it reveals the existence of another bunch of stripes formed along a different direction and with a much higher width. A corresponding line cut (blue line) is shown in Figure 3.4(c).

3.7.1 Probing the ripples under various conditions

On reversing bias voltage: We change the sign of tip-sample bias to check whether there is any effect of reversing the voltage on the bright and dark contrast of the stripes. But the contrast remains same on reversing voltage between tip and sample.

Effect of temperature: There is no effect of varying temperature on the pattern .

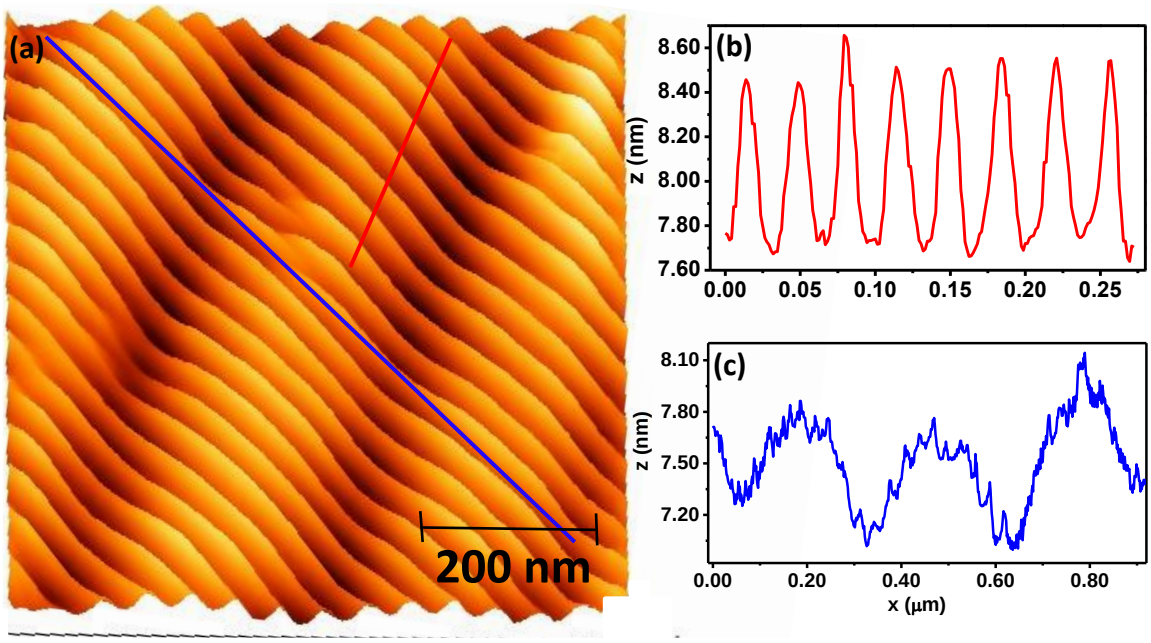

Figure 3.4: (a) 3D picture of large area STM topograph of the cleaved surface of Re doped $MoTe_2$ obtained in a "high-strain" region. The periodic modulation due to strain-induced ripples is observed. Variation of topographic height along (b) the red line shown in (a), (c) along the blue line shown in (a).

The topographic height of the ripples remains same of the order of ~ 8 $\mathring{A}$. on varying temperature. The ripples are formed during surface cleaving at high temperature (77 K) and they persist down to lowest temperature we have measured.

Effect of variation in scanning parameters: We have probed these ripples by changing scan angles, scan areas, and other scan parameters to unambiguously confirm that they are real topographic features. The number of ripples (n) and their spacing (Δl) do not vary with changing the scan angle and for all scan angles, n changes systematically with changing scan size.

In Figure 3.5, we show a different region away from that shown in Figure 3.4(a). In this region, the ripples formed are not dense and are present with larger width. These stripes might be due to the formation of a moiré pattern induced by the strained surface of the crystal. Such strain-induced patterns were earlier seen in other two dimensional materials like graphite [95]. As the ripples present in this area are not that dense, so we can say that this area is less strained as compared to the previous one. In fact, in this region, the strain responsible for the denser ripples [as in Figure 3.4(a)] is absent. We will show later that in these regions, the effect of the pseudo-magnetic field is not observed.

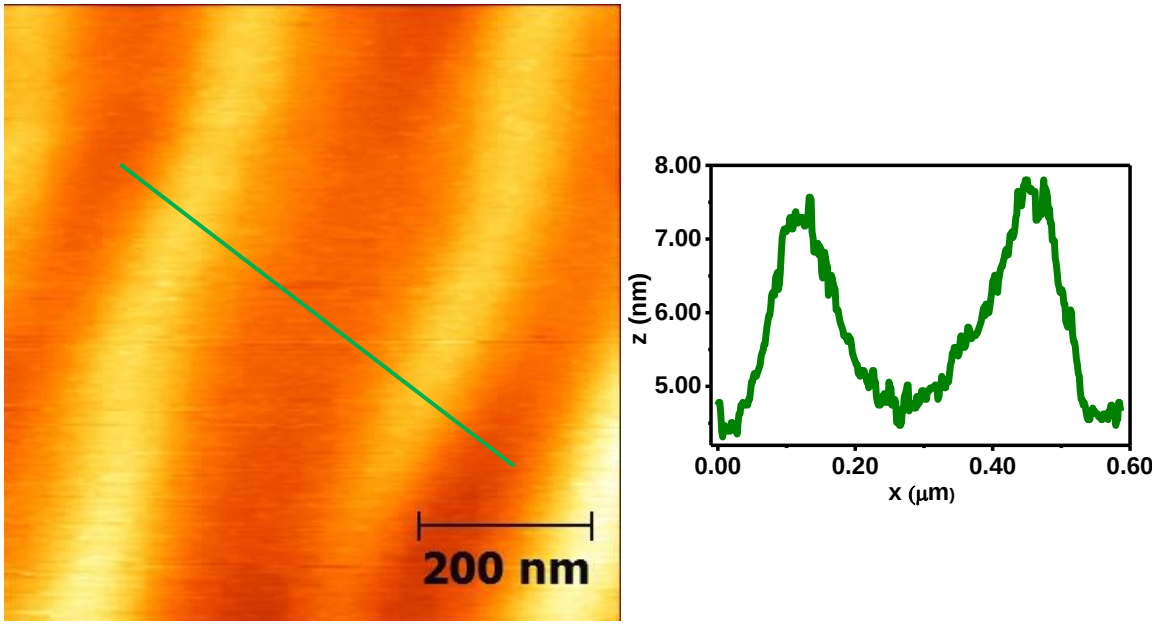

Figure 3.5: STM topograph of a large area in a "low-strain" region. The inset shows the topographic modulation along the green line.

When we zoom into a small area (20 nm $\times$ 20 nm) as shown in Figure 3.6, we observe the periodic arrangement of the atoms on the surface. At this length scale, the arrangement of the atoms on the surface is found to be identical at all regions under different levels of strain.

However, we could not predict anything from the angle which 35 nm-periodicity ripples made with the atomic rows, though, it would be interesting to see at what angle these topographic ripples are alligned to the atomic rows. The 35 nm-periodicity ripples are at an angle to the atomic rows. The angle can be clearly seen in 30 nm $\times$ 30 nm atomic resolution image and 700 nm $\times$ 700 nm scan in the following Figure 3.7. We have not given any rotation to either of them. The direction can be compared directly.

Now when we move the STM tip to different points on the high-strain region represented by Fig. 3.8(a), we obtain spectra as seen in Fig. 3.8(b). At 310 mK, distinct and strong peaks, along with the central dip due to superconductivity, are seen in the dI/dV vs V spectra. The three spectra shown in the Figure 3.8(b) are obtained from three different points in the same high-strain region. The peaks are separated by an energy of $\sim$ 1.3 meV.

Further, we focus on the local tunneling spectroscopy experiments. When we move

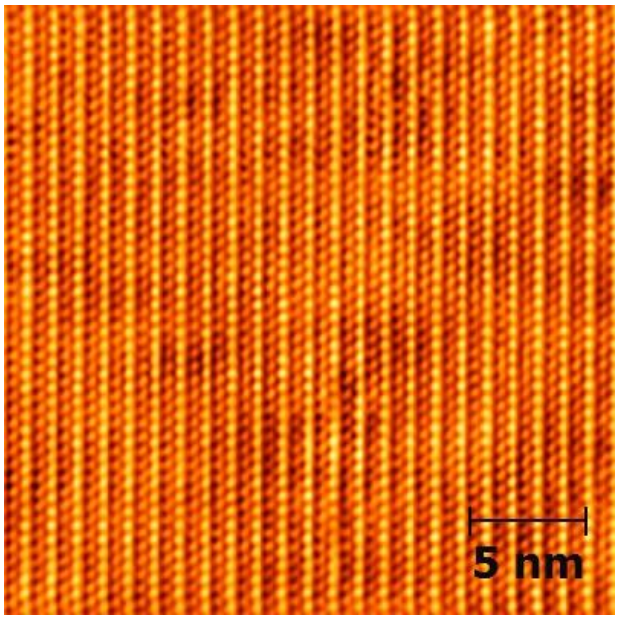

Figure 3.6: STM topograph of a 20 nm $\times$ 20 nm area within the same region as in fig 3.4(a). The atoms are clearly resolved.

the STM tip to points located in the low-strain area as shown in Figure 3.8(c) at a temperature of 310 mK, we obtain the spectra as shown in Fig. 3.8(d). We have shown three representative spectra obtained at three points on the surface. All the three spectra show the evidence of a superconducting energy gap. Superconductivity in Re-$MoTe_2$ with 20% Re doping is known to appear at $\sim$ 3.8 K. No other prominent spectral features other than the superconducting energy gap, could be observed.

The peaks observed in high-strain area do not appear in the spectra obtained from the low-strain regions of the crystal. We obtained spectra with such peaks on more than 50 points in different high-strain regions. Various spectra are recorded on a number of points in the area including on the peak of ripples and away from the peak of ripples, the spectra remains more or less same at all these points (see appendix). The position of the peaks remains almost at the same location with approximately 5% variation which might be due to the variation of the strain itself from one high-strain region to another. Since the dI/dV spectrum at a given point is directly related to the local density of states (LDOS) at that point, the peaks in this case represent quantized energy levels. The peaks in dI/dV in the strained region can be well understood in terms of the presence of a pseudomagnetic field, which is not a surprise at all in Weyl semimetals. Such quantized levels appear-

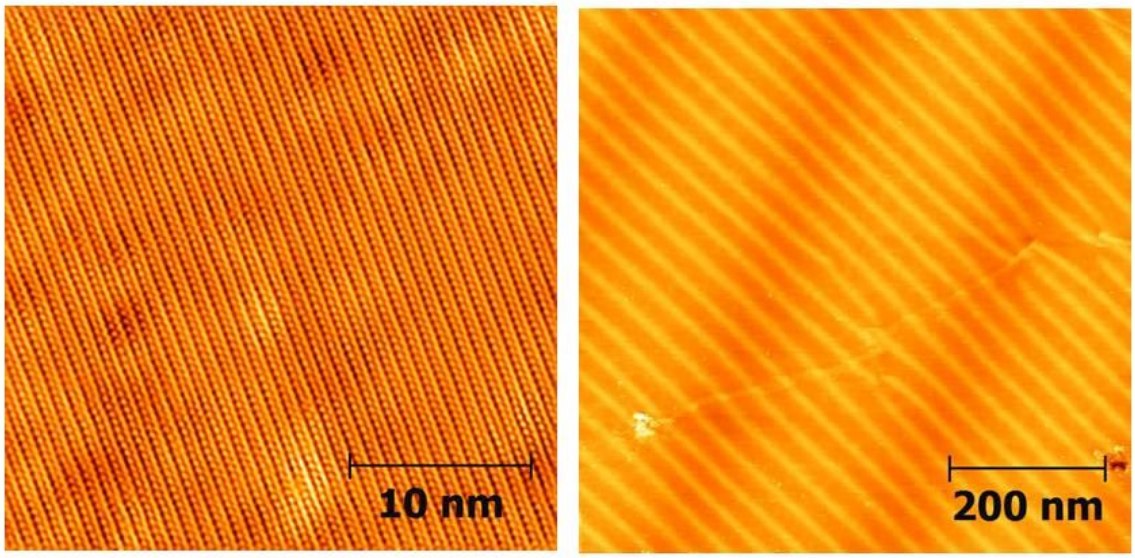

Figure 3.7: (left) 30 nm × 30 nm atomic resolution image and (right) 700 nm × 700 nm scan

ing in the presence of a large externally applied magnetic field have been observed in a number of topological systems in the past [96]. These are the well-known Landau levels. In the present case, since the discretization takes place without any externally applied magnetic field, the peaks can be attributed to the Landau levels forming due to a strain-induced pseudo-magnetic field appearing in the system. The features of these peaks are expected to change with the change in temperature, so let us have a look over the effect of temperature on the Landau levels formed in the system.

3.8 Effect of temperature on the spectrum obtained in "high-strain" region

The oscillation amplitude and width of each peak due to pseudo Landau levels are also expected to evolve systematically with changing temperature. Figure 3.9 shows the temperature evolution of the spectra obtained at a point in "high-strain" area. At 310 mK, superconducting gap can be seen along with oscillations with large amplitude due to landau levels. The oscillation amplitude decreases with rise in temperature whereas, the oscillation frequecy remains the same. At 1.3 K, the oscillation amplitude reduces almost down to the background noise level. The oscillation disappears within the background at 1.5 K. To note, up to this point the spacing between two consecutive peaks should not

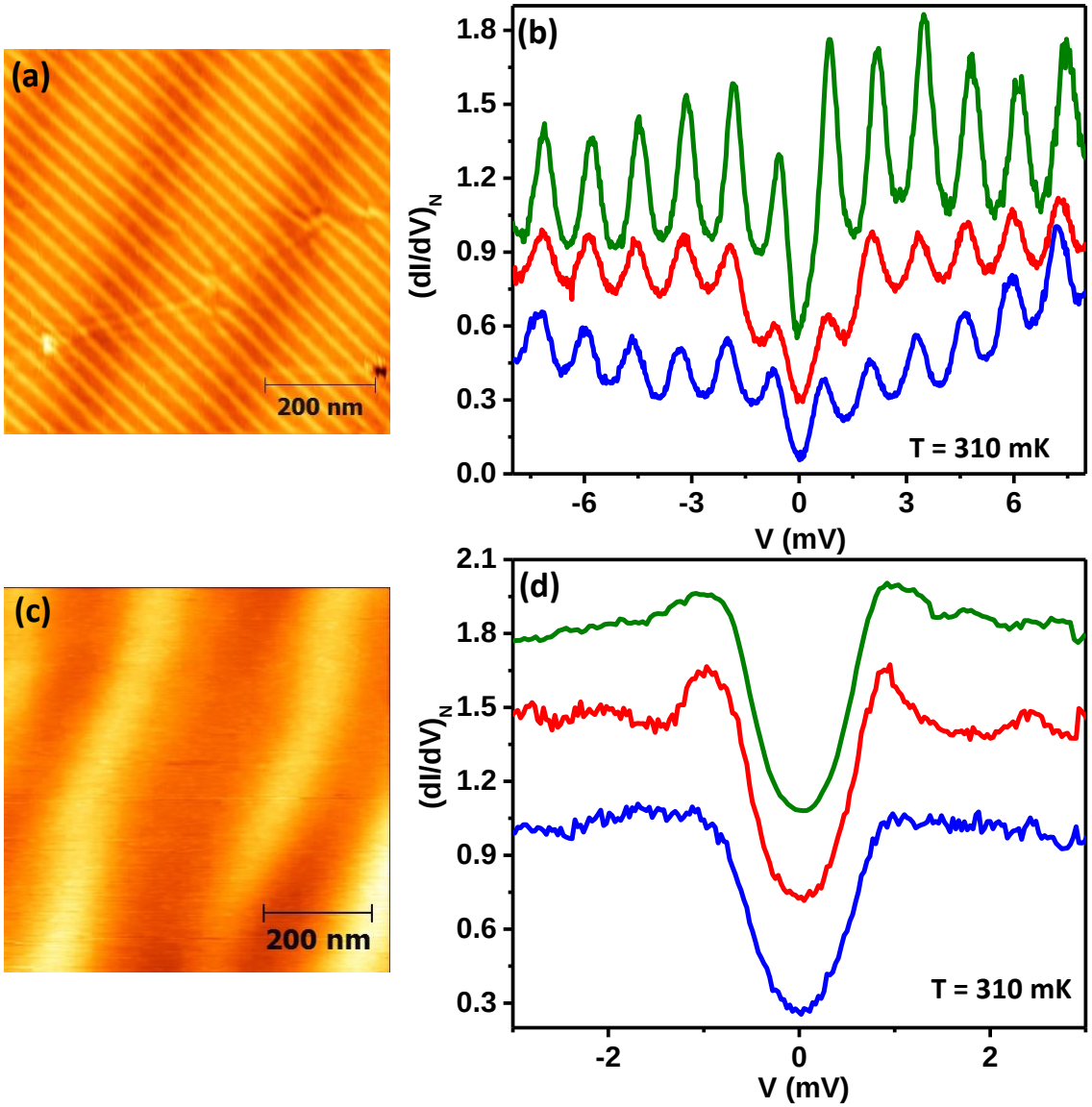

Figure 3.8: (b) Tunneling spectra in the "high-strain" region at 310 mK showing LL oscillations along with a low bias conductance dip at three different points in the "high-strain" region as in (a). (d) Tunneling spectra recorded at 310 mK at three different points in the "low-strain" area as shown in (c).

show a noticeable change as the temperature scale is significantly smaller than the separation energy scale. We can explain this as, the peak seperation, in terms of energy is 1.3 meV, which corresponds to $\sim$ 15.1 K. Thus we can not expect the oscillations to disappear at 1.5 K due to thermal broadening.

Further, with increasing temperature, the spacing between the Landau levels do not alter, only the broadening of the states increases rapidly, to make the oscillation in density of states (DOS) indistinguishable by 1.5K. This means, the pseudo-magnetic field is also present above 1.5K, but the Landau levels become rapidly broadened (much faster than

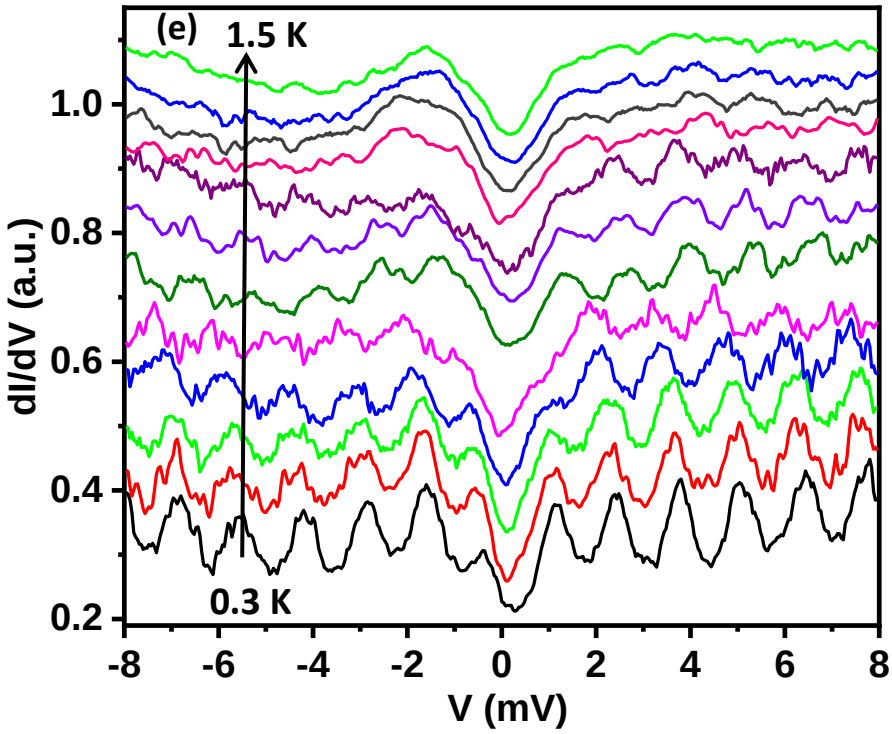

Figure 3.9: Temperature evolution of the STS data. The oscillations get vanished at 1.5 K.

their typical thermal broadening). Hence, the disappearance is not expected to be due to the loss of discreteness of the spectrum due to thermal broadening, but due to additional effects which could possibly be due to disorder and phonons. However, the exact mechanism can not be determined from our experiments. In fact, addition of any kind of higher order interaction term to the Hamiltonian used in our model (to be discussed later) can, in principle, account for such non-thermal broadening effects.

One could imagine another possibility where the strain field itself evolves with temperature. For that, when we look at the details of the ripples at different temperatures, we could not find any change. The ripples at a much higher temperature where they exist do not display any difference from the low temperature images and also, there is no difference in the topographic height of the ripples at different temperatures. The ripples, in fact, are formed during surface cleaving at high temperature (77 K) and they persist down to lowest temperature we have measured. Thus, such possibility where the strain field itself evolves, has been ruled out because we did not find any noticeable change in the topographic ripple structure as a function of temperature.

3.9 Other possibilities for oscillations

Before attributing the discrete energy levels with the pseudo-magnetic field induced Landau levels, we have carefully considered other sources of such a signal.

1. **Impurities**: In STM experiments, oscillations may arise due to trapped impurity states. To rule out this possibility experiment has been done on "high-strain" areas near and far from the impurities as seen in the STM images. The oscillation pattern did not depend on that and remains the same at all points in high strained region.

2. **Confinement or trapped states**: In our system, the energy gap between two consecutive peaks remained nearly the same for a given spectra and almost same for all the spectra in a given "high-strain" region. The simplest confinement system is "particle in a box", where the energy gap between consecutive levels is not same. We can not expect such thing for any other complex confinement system. Thus the role of arbitrary confinement potential is ruled out. Furthermore, Klein tunneling in Weyl and Dirac semimetals forbids the formation of such trapped/confined states [97].

3. **Superconductivity**: Unlikely because in the low-strain area superconductivity is observed but no oscillations and also in high-strain area, the oscillation frequency and amplitude remained insensitive to an externally applied magnetic field. Hence the oscillation is directly related to the strain.

In addition to the above-mentioned facts, the appearance of the oscillations in the high-strain areas and the absence of the same in the low-strain areas directly confirms that there is a direct correlation between the observed oscillations and strain.

Furthermore, from the images of the "high-strain" region it is clear that the strain is inhomogeneous, and also periodic with a periodicity which is much larger than the underlying lattice constant. Intuitively, a variation of the measured pseudo-magnetic field is also expected. However, we observe almost homogeneous magnetic field over a given strain region. This has agreed with the modelling used in the theoretical calulations (discussed below) in the low energy limit of our model. Any variation in B might emerge as

a higher energy correction to the model.

3.10 Brief theoretical calculations

Theoretical calculations for the above experiment were done by some of the co-authors (Paratha Sarathi Rana and Tanmoy Das) of the manuscript "Generation of strain-induced pseudo-magnetic field in a doped type-II Weyl semimetal" (Phys. Rev. B **100**, 115105 (2019)). I will briefly discuss about the calculatoins. Let us assume that the ripples are formed on the surface and they get relaxed as we go down. In Figure 3.10, a neutral axis can be seen, where there is no strain. And thus we can get spatial dependence of a quantity say $\mathbf{A}$. x, y and z axes are defined in the figure. y-axis is the cylindrical axis of the ripples and we assume inhomogenity in strain along the x-axis, and z-axis is perpendicular to the neutral plane. From electronic structure point of view, the electron's hopping along the x-axis is modulated in space, giving the gauge field in this case, whereas along the y-axis, it remains the same. Thus, strain comes into the hopping term $u_{xx} = \partial u_x/\partial x$.

We use a type-II Weyl Hamiltonian specific for $MoTe_2$ [98, 99], $H = d_0(\mathbf{k})I_{2\times 2} + \sum_{\mu=1}^{3} d_\mu(\mathbf{k})\sigma_\mu$, where σ_μ are the 2-component Pauli matrices, and d_μ are their anisotropic coefficients. For convenience of illustration, we simplify the coefficients with a trivial rotation of the coordinate system from the lattice frame of reference to our above-mentioned set-up and obtain $d_0 = t_0 \sin(k_y a_y) - \epsilon_F$, $d_\mu = t'_\mu \sin(k_\mu a_\mu)$, where μ=1,2,3, and lattice constants a_μ are the lattice constants in the strained lattice, and k_μ are measured with respect to the Weyl points $\mathbf{Q}$. t_0, and t'_μ are the intra-species and inter-species hopping integrals, respectively.

As we discussed before, the rippled structure induces a spatial dependence in the tight-binding hopping along the x-direction as $t'_x\sigma_x \rightarrow t'_x(1-u_{xx})\sigma_x + \sum_{\mu'\neq x} u_{\mu\mu'}t'_{\mu'}\sigma_{\mu'}$, where u_{ij} is the stress tensor obtained from the displacement field vectors $\mathbf{u}$ as $u_{xx} = \partial u_x/\partial x$. [100,101] The displacement field vector can be approximated to the lowest order as $\mathbf{u} = [zx/(R-d), 0, 0]$, see Figure 3.10(bottom)

Now we will see how the spatially modulated hopping provides a vector potential. It is

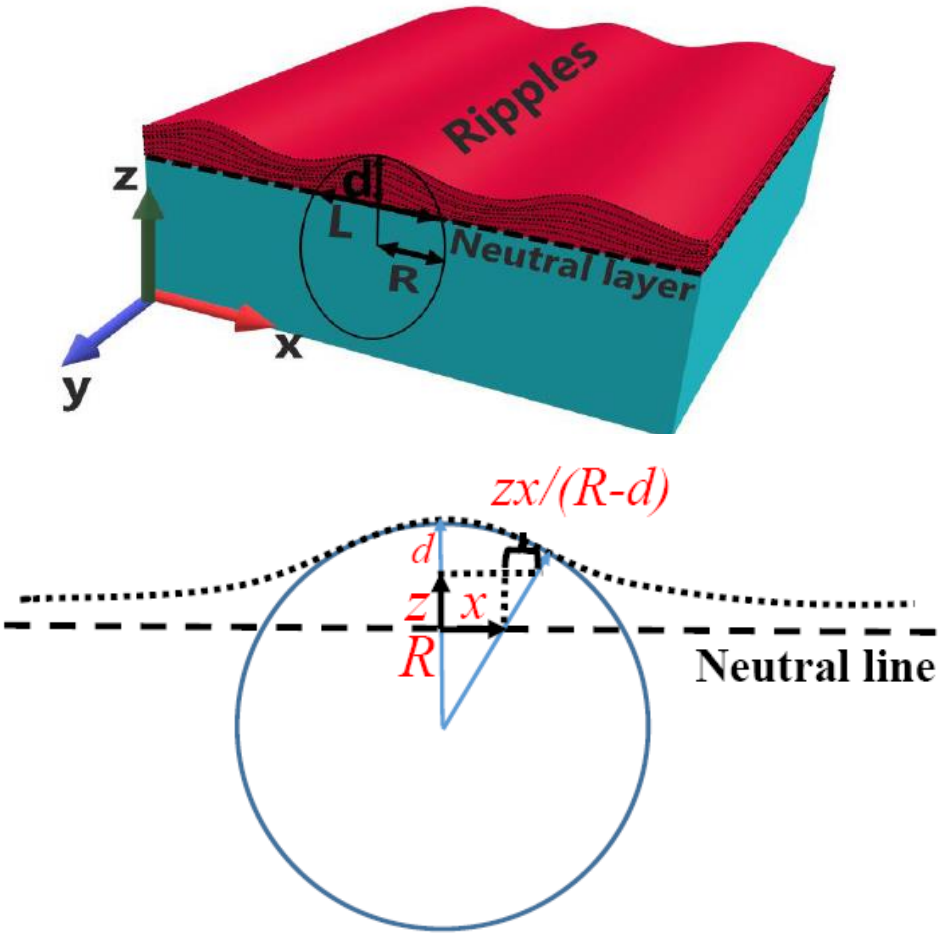

Figure 3.10: Theoretical model solution to the strained induced LL spectrum (top) A Schematic description of the setup, consisting of ripples with d-length sticking out from the neutral surface (first strain-less surface down the material). (bottom) A single ripple (black dotted line) and its tip with radius of curvature R. x and z are the displacement in the corresponding directions, giving a displacement field along x-direction as $u_x = zx/(R-d)$.

convenient to use the long-wavelength limit of the Hamiltonian by substituting $\sin(k_\mu a_\mu) \sim k_\mu a_\mu$, and expressing the tilt velocity as $\omega_\perp = t_y a_y$, and the Weyl fermion velocity as $v_\mu = t' a_\mu$, we obtain the effective low-energy Hamiltonian as

$$H \approx (\omega_\perp k_y - \epsilon_{\mathrm{F}}) I_{2\times 2} + \sum_{\mu=1}^{3} v_\mu \sigma_\mu (k_\mu - e\mathcal{A}_\mu). \tag{88}$$

(We set $\hbar = 1$ for simplicity). The above equation resembles a typical low-energy Hamiltonian for massless fermions under a vector potential $\mathcal{A}$, except here $\mathcal{A}$ arises intrinsically from $t'_\mu(\mathbf{r})$. With a lengthy algebra, we estimate $\mathcal{A} = \frac{1}{e}\left(\frac{z}{a_x(R-d)}\tan(Q_x a_x), 0, \frac{x}{a_z(R-d)}\tan(Q_z a_z)\right)$ where $\mathbf{Q} \sim 2\pi/a_x(0.18, 0.17, 0)$, is the location of the Weyl points in this system.

Now, from the STM images (Figure 3.4), we find that the ripples are very much one-

dimensional and periodic, with average ripple height of $8\mathring{A}$ (from the surface), and with about L=35 nm of inter-ripple distance. Radius of curvature of the tip of ripple is R, and tip of $d\sim 41.3\mathring{A}$-height is sticking out from the neutral plane of the surface, and L is the spatial extent of one ripple and lattice strain is calculated from the lattice parameters in strained and unstrained area and it comes out to be 3%. With the experimental inputs of 3% lattice strain giving $a_x = 3.46\mathring{A}$,$a_z = 13.86\mathring{A}$, $d = 41.3\mathring{A}$ and $R = 34d$ we obtain the magnetic field to be $\mathcal{B} \approx 3\,T$ aligned along the y-direction.

In this model, a minimal coupling theory has been considered, which means we only considered the strain near its extrema with the leading order term in space [c.f. the expression for u_{xx}=$[zx/(R-d)]$. This strain translates into a vector potential in the long-wavelength limit of the Hamiltonian. The vector potential itself shows spatial variation, but within this approximation, the pseudo-magnetic field remains constant in space. If higher order terms are included in the calculation, an inhomogeneity in the magnetic field can arise, but that may not be very large.

The estimated magnetic field is large enough to separate the LL's above the intrinsic broadening scale of the system. However, the manifestation of the LL's into oscillations in DOS is required to overcome additional constrained posed by the peculiarities of the type-II Weyl fermions. In such Weyl fermion cases, we find that (a) the tilt velocity manifests into dispersive LLs and hence its bandwidth W is required to be smaller than the LL spacing for its visualization, and (b) the tilt velocity must overcome a threshold value to commence closed Fermi pocket.

(a) Dispersive Landau levels: The LL's are split across the tilting term with its dispersive obtained from Eq. (88) as

$$E_n^{\pm}(k) = \omega_\perp k_y - \epsilon_{\rm F} \pm \sqrt{(v_y k_y)^2 + 2(v_\perp/l_B)^2 n}, \tag{89}$$

where the magnetic length $l_B = 1/\sqrt{e\mathcal{B}}$, $v_\perp = \sqrt{|\,v_x v_z\,|}$. Interestingly, the LLs are chiral with its velocity arising from the tilt velocity $\omega_\perp$. Such chiral cyclotron orbits arise with

electric field perpendicular to the velocity [102]. Hence, the type-II Weyl semimetals can be understood to experience pseudo-magnetic and pseudo-electric field simultaneously under strain. The LL splitting can be appreciated in the limit of $2v_\perp/l_B < v_y k_y$ which is satisfied in the large magnetic field limit as achieved in our experiments. In this limit, Eq.

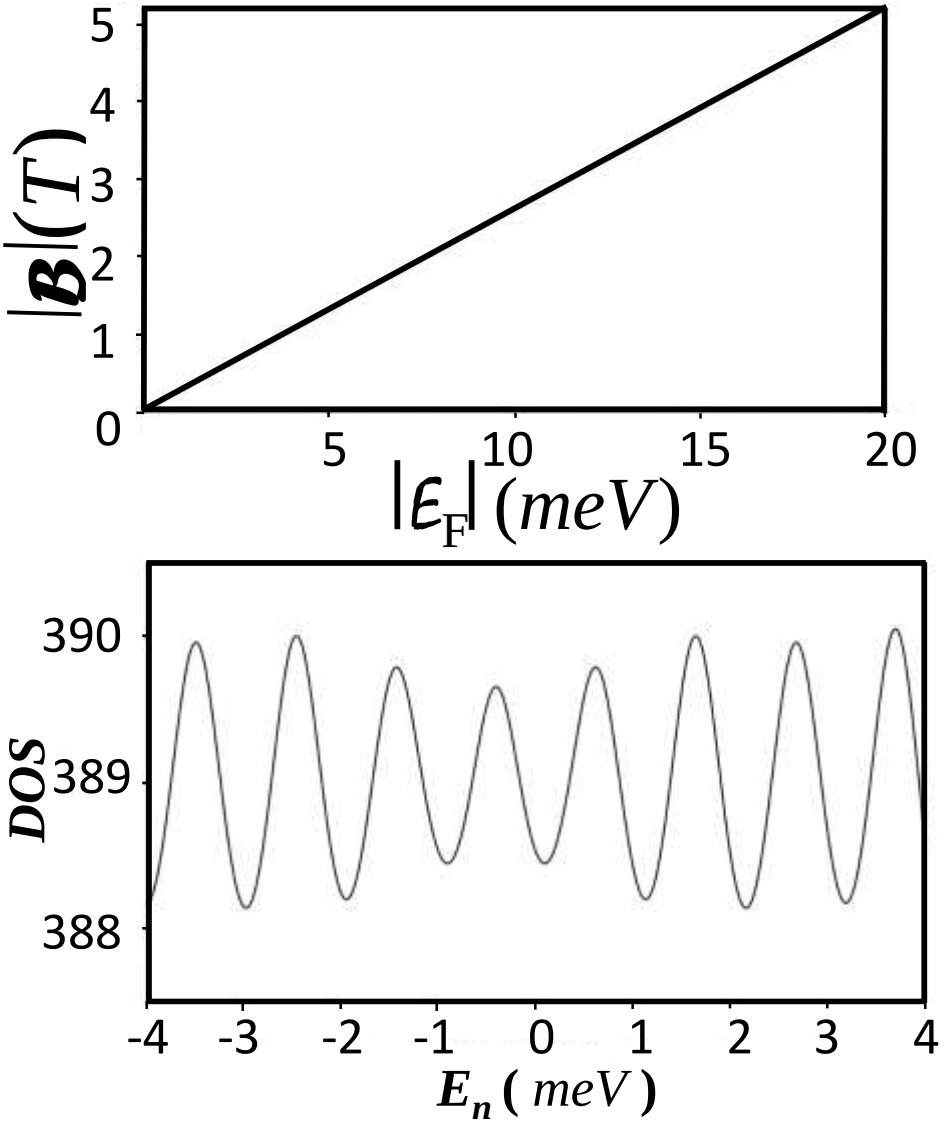

Figure 3.11: (top) $\mathcal{B}$ vs v_F plot, from which order of pseudo-magnetic field is estimated semiclassically. (bottom) Density of states vs energy showing discrete Landau levels.

(89) can be written for the lowest Landau levels as

$$E_n^{\pm}(k) = \omega_\perp k_y - \epsilon_{\mathrm{F}} \pm v_y k_y \left(1 + \frac{{v_\perp}^2}{{l_B}^2 (v_y k_y)^2} n\right). \tag{90}$$

Equation (90) indicates that in the limit of $2v_\perp/l_B < v_y k_y$, the low-energy Landau

levels would appear as equally spaced in energy. By substituting the realistic values of the velocity parameters (v_y, $v_\perp$) from the DFT estimates from Refs. [98, 99], and the magnetic length for 3T field values, we obtain $v_\perp/l_B \sim 10^{-4}$, while $v_y k_y \sim 10^{-2}$ (in unit of eV $\mathring{A}$). Thus the condition $2v_\perp/l_B < v_y k_y$ is indeed achieved in our system as also observed experimentally.

The calculated DOS are shown in Figure 3.11(bottom) for $\mathcal{B} = 3T$ and with all other band parameters set as in Ref. [98, 99].

(b) Closed FS formation: According to the Lifshitz-Kosevich paradigm, the quantum oscillation requires the FS perpendicular to the field orientation to form closed contour, and the oscillation frequency is proportional to the FS area. [103, 104] Type-II Weyl fermions however may fail to form closed FS pocket due to the tilt, [85] unless the tilt velocity is substantially modified. The pseudo-magnetic field is aligned along the y-direction, and thus we focus on the condition for a closed FS in the (k_x, k_z)-plane. We find that the DFT-derived value of the band parameters for $MoTe_2$ fail to give closed contour, However, the modifications of the hopping parameter t'_μ with the pseudo-magnetic field renders closed Fermi surface on the (k_x, k_z)-plane.

Our theoretical analysis reveals that strained Re-doped $MoTe_2$ supports large separation of the Landau-levels (LLs) in the density of states making the experimental detection of the pseudomagnetic field possible.

3.11 Conclusion

Oscillations in the differential conductance are observed in regions where the topographic ripples exist. Peaks in the dI/dV (or density of states) are interpreted as the discrete Landau levels created by the strain-induced pseudo-magnetic field. In the theoretical model, the pseudo-magnetic field is estimated to be $\sim$ 3 Tesla for this specific type of Weyl semimetal.

The reported material is interesting in terms of the coexistence of multiple orders such as the superconductivity, charge density wave, atomic modulations, as well as the

topological order. It could serve as a model system to study some fundamental issues in condensed matter physics as well as their interrelationships, such as the interplay between the (enhanced) superconductivity and pseudo-magnetic field.

There are couple of things that we could not conclusively address and remain open for further investigation: (a) the disappearance of the Landau levels far below the characteristic energy scale and (b) the reason for the remarkable validity of a minimal coupling theory in a strained type II Weyl semimetal.

One more thing I would like to mention here that though the effect of pseudomagnetic field in Weyl semimetals looks seemingly similar to that in graphene, one must note the subtle differences in the condition under which such effects can be observed in graphene and in Weyl semimetals. The first requirement of course is a linear band which is readily available in graphene as well as in Weyl semimetals.

In Weyl semimetals, apart from the inhomogeneous strain and the satisfaction of the closed orbit criteria, no special spatial symmetry requirements are there for the observation of a pseudomagnetic field, whereas for graphene, a triangular symmetry is also required. The individual nanobubbles of graphene grown on Pt(111) often showed triangular shape. Consequently, the possibility of obtaining a uniform pseudomagnetic field is higher for Weyl semimetals. In fact, this makes our work on the Weyl semimetal special and different from the observations on graphene and is expected to attract attention of the theoretical community.

3.12 Appendix

3.12.1 Effect of external applied magnetic field on the oscillations observed in "high-strain" area

Considering the pattern of the strain-induced ripples and theoretical modeling of the same, it is clear that in this case the direction of the pseudo-magnetic field is along the axis of the stripes in the plane of the crystal surface. Applying an external magnetic field of the order

of 3T is non-trivial along the plane of the sample in an STM set up. Such measuresments would require a sub-kelvin STM head mounted inside a powerful vector magnet where the vector field is of the order of 3 Tesla. We do not have such a non-trivial system available in our lab.

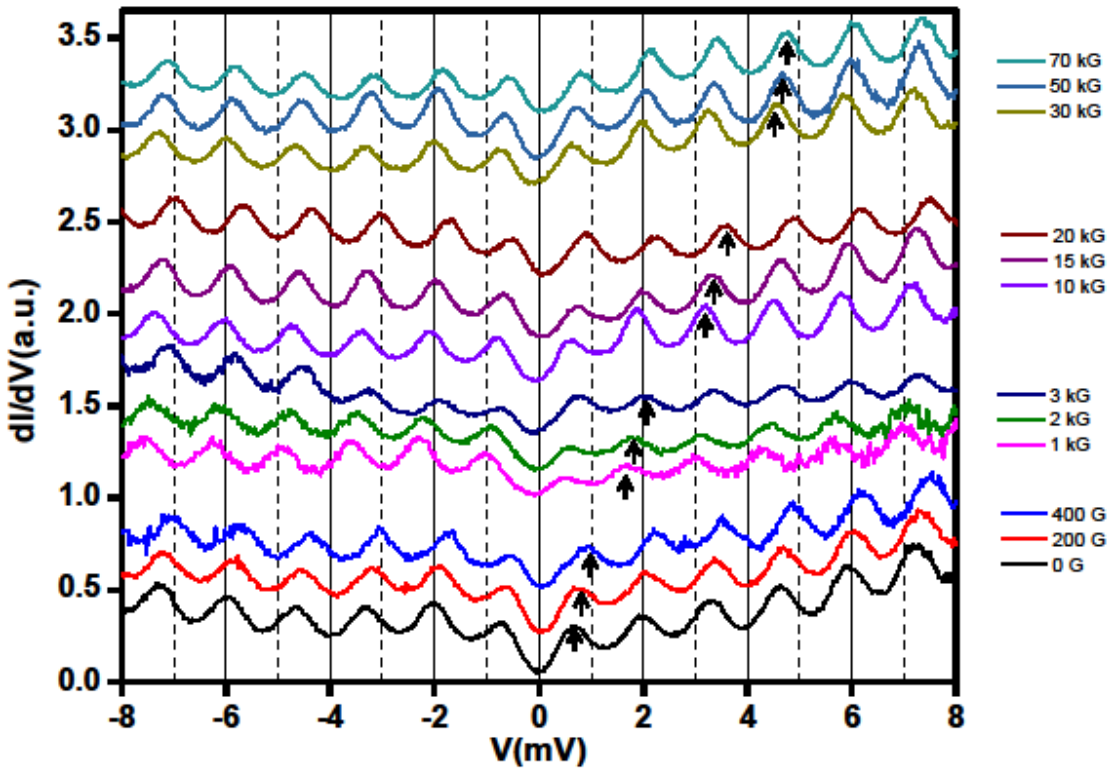

Figure 3.12: Tunneling spectra in the high strain region at 310 mK in the presence of magnetic field. To make a clear comparison among the spectra in the presence of magnetic field, the spectra are plotted in the set of 3 magnetic fields (0 to 400 G, 1kG to 3 kG, 10 kG to 20 kG and 30 kG to 70 kG). The figure shows a shift in the peaks observed in dI/dV among the spectra in a particular set of applied magnetic field. This indicates the real magnetic field is somehow mixed with the pseudo magnetic field.

However we performed experiments to look at the coupling between the pseudomagnetic field and an externally applied magnetic field, where we applied magnetic field and studied the evolution of the strain-induced peaks in dI/dV as a function of the external magnetic field strength. Since our magnet is a superconducting solenoid with the field direction pointing perpendicular to the plane of the crystal surface, this does not create additional peaks in the spectra (as can be seen in Figure 3.12). But, the field causes a systematic phase shift of the peak patterns as the strength of the field is increased. We show a number of spectra captured at different applied magnetic field in the Figure 3.12

to show the effect clearly. To note, up to a high magnetic field of 7 Tesla, no additional peaks in the dI/dV are observed. This further confirms that application of a magnetic field along a perpendicular direction does not cause Landau quantization explaining why such a field would not produce oscillations in the low-strained area.

3.13 Some additional data

I am including some additional data like topographic images in "high strain" area of different sizes and differential conductance spectra recorded at different points in "high strain" area.

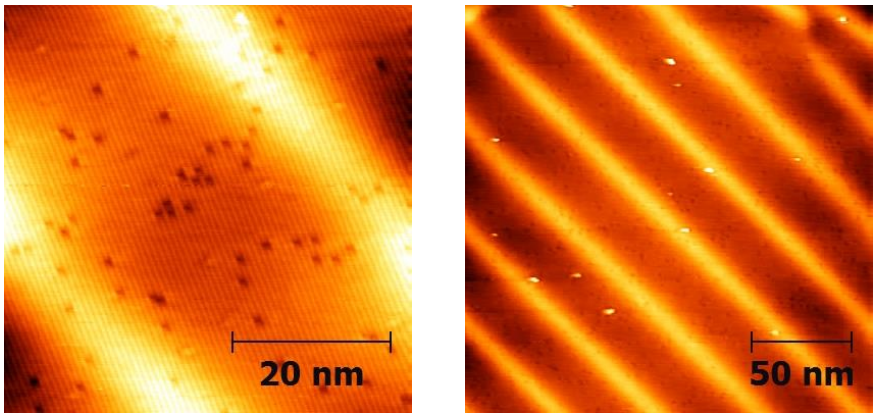

Figure 3.13: 60 nm x 60 nm and 200 nm x 200 nm STM topograph of the cleaved surface of Re-$MoTe_2$ obtained in a "high-strain" region respectively. The periodic modulation due to strain-induced ripples is observed.

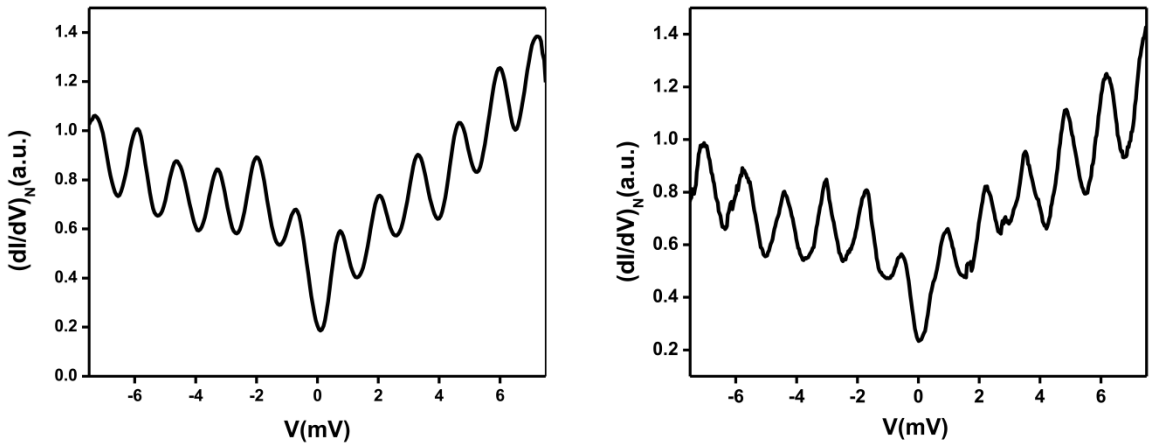

Figure 3.14: Differential conductance spectrum recorded at 310 mK showing LL oscillations along with a low-bias conductance dip at two additional points in the high strained region.

3.13.1 Synthesis of $ReMoTe_2$

The synthesis of $ReMoTe_2$ crystals was done in collaboration with Manasi Mandal, Sourav Marik and Ravi Prakash Singh. Polycrystalline samples of composition $Mo_{1-x}Re_xTe_2$ (pure phase) were prepared by the standard solid-state reaction process. Mo (99.9% pure), Re (99.99% pure) and Te (99.99% pure) powders were ground together in the required stoichiometry and then sealed in an evacuated quartz tube. The ampoules were first heated for 24 hours at 1100° C. Then the obtained samples were ground, pelletized, and annealed at 1100° C for 24 hours. After this ice water quenching is done to avoid the formation of the 2H phases. Iodine is used as a transport agent while growing single crystals of composition $Mo_{0.8}Re_{0.2}Te_2$ via chemical vapour transport method using polycrystalline $Mo_{0.8}Re_{0.2}Te_2$ powder. Crystals were obtained by sealing 3g of $Mo_{0.8}Re_{0.2}Te_2$ powder and I_2 in a quartz tube. The tube was then flushed with Argon, evacuated, sealed and heated in a two-zone furnace. Crystallization was carried out from 1100° C (hot zone) to 1000° C (cold zone) for 14 days. Finally, the sealed quartz tube was quenched in ice water to avoid the formation of the hexagonal phase.

4 Transport spin-polarization in the low Curie temperature complex itinerant ferromagnet $EuTi_{1-x}Nb_xO_3$

Spintronics is a field of physics that studies the spin of electrons, an intrinsic type of magnetism that many elementary particles have. The field of spintronics has led to technological concepts of "spintronic devices", which involves manipuation of the spin of electrons. In this regard, determination and understanding of spin polarization in novel materials is of utmost importance. The quest for efficient generation of spin has motivated physicists to search for materials which possess a high degree of spin polarization. One such class of materials are itinerant ferromagnets which are known to possess a high degree of spin polarization and thus can act as a source for spin polarized electrons [105–107].

The efficiency of a spintronic device depends on its degree of polarization at ambient temperatures. However, most of the traditional "transport" spin polarization measurement techniques rely on low-temperature experiments, therefore, it is important to understand temperature evolution of the magnitude of spin polarization in materials. In chapter 1, we have discussed in detail that point contact Andreev reflection (PCAR) spectroscopy can be used to find the spin polarization in a ferromagnet. However, in PCAR experiments the temperature range for investigation of spin-polarization is restricted by the transition temperature of the superconducting tip used in the measurement. Therefore, for successful estimation of transport spin-polarization using such technique it is important to understand temperature evolution of magnitude of spin polarization in materials.

It is traditionally assumed that the spin polarization at the Fermi level of a metallic ferromagnet evolves with temperature following a proportional relationship with the spontaneous magnetization (M_S). While this assumption has been experimentally verified for strictly parabolic bands, there has been no experimental verification of this scenario for materials that can not be characterized by conventional metallicity, where this simplistic picture may not be valid. Hence, it would be interesting to investigate evolution of transport spin-polarization in complex ferromagnetic system. In this context,

$EuTi_{1-x}Nb_xO_3$ for x= 0.15, is a good candidate as it is "bad" metal and at the same time, a ferromagnet with low T_c 9.5 K [108], here T_c falls within the low temperature limit where time evolution of spin polarization like measurements are possible. In this chapter, we have employed spin-resolved Andreev reflection spectroscopy using conventional superconducting tip of Nb to measure the transport spin-polarization at the Fermi level of Nb doped $EuTiO_3$ and then discuss about spin-polarization measurements on $EuTiNbO_3$ using spin-resolved PCAR spectroscopy.

4.1 $EuTiO_3$ as a member of perovskite titanate family

Over the last several decades, the perovskite titanate family of compounds with a general formula $RTiO_3$ (R = rare earth ion) have attracted significant attention of the condensed matter community due to the potential of these compounds to show the co-existence of exotic magnetism and complex charge scattering processes and their interplay. Special attention has been received by the members of the family where ferromagnetism coexists with bad metallicity governed by strong electron-correlation. It has been observed that in such ferromagnets, the transport and magnetic properties and their correlations deviate significantly from those of the good metallic elemental ferromagnets like iron, cobalt, nickel etc. The perovskite titanate family $RTiO_3$ (R = rare earth ion) with $3d^1$ electron configuration has attracted researchers since last two decades owing to their several fascinating properties including magnetic, dielectric and superconducting properties that have been reported for this family. [109–112]. There has been a considerable amount of theoretical and experimental work done for understanding the nature of the orbital ground state in this family. In the perovskite titanate family $RTiO_3$, R is rare-earth ion with a $3d^1$ electron configuration. Among these titanates, $EuTiO_3$ is unique because, unlike other R ions, Eu is divalent ($4f^7$). Also, $EuTiO_3$ is an anti ferromagnetic (T_N = 5.5 K) band insulator while other titanates are Mott insulators. Among the perovskites, $EuTiO_3$ with divalent rare-earth ion Eu and tetravalent Ti has generated substantial interest since the discovery of magnetoelectric coupling in this compound below the antiferromagnetic

(AFM) transition temperature T_N = 5.5 K [113–118]. $EuTiO_3$ is antiferromagnetic with a positive Currie-Weiss constant and exhibits strong coupling between magnetic ordering and phonon modes. Efforts have been made to drive this system from antiferromagnetic phase to other magnetic phases upon modifications due to partial substitution at the Ti site. Small amount of substitution at Ti site by Nb drives the system from antiferromagnetic to ferromagnetic system(shown in figure later) [113–115]. In the ferromagnetic state, the resistivity shows a T^2 temperature dependence possibly due to electron-magnon scattering and above the curie temperature T_c, the dependence changes to $T^{3/2}$ behaviour indicating a correlation between transport and magnetic properties [116]. Substitution by Nb^{4+} ion at the Ti^{4+} results in the introduction of electrons in $EuTiO_3$ without disturbing the Eu^{2+} moments chain. Previous studies in $EuTi_{1-x}Nb_xO_3$ revealed notable increase in electrical conductivity and large values of magnetocaloric response of about 23.8 J $kg^{-1}K^{-1}$ even at low magnetic field 0-2 T [116]. Therefore, introduction of Nb in antiferromagnetic $EuTiO_3$ results in ferromagnetic behaviour in $EuTi_{1-x}Nb_xO_3$ (x = 0.15) with T_c 9.5 K and with saturation magnetization at low temperature of 2 K and 9 T magnetic field is estimated to be close to the expected moment of $7\mu_B/Eu$ [116].

4.2 Potential application of $EuTiO_3$

$EuTiO_3$ is a multiferroic system and it exhibits strong antiferromagnetism and strong ferroelectricity simultaneously. On doping $EuTiO_3$ with Nb at the site of Ti, it transforms into a ferromagnetic system. Coexistence of ferroelectricity and ferromagnetism can arise several good potential applications for spintronics. Also, $EuTiO_3$ has not only a large dielectric constant but also the dielectric constant increases with decreasing temperature and exhibits a sudden drop at T_N(Neel temperature) which can be reverted by an external magnetic field, thus indicating strong magneto-electric coupling. This is another interesting area where active research is going on.

4.3 Emergence of ferromagnetism from antiferromagnetism on Nb substitution at Ti site

The temperature dependence of magnetizations of single crystalline $EuTi_{1-x}Nb_x$ O_3 for various x is shown in the Figure 4.1. $EuTiO_3$ is antiferromagnetic with a positive Curie -Weiss constant. However on doping Nb in $EuTiO_3$ ($x = 0.05$), the system shows a transition from antiferromagnetic state to ferromagnetic state and it remains ferromagnetic for the rest of the dopings as shown in Figure 4.1.

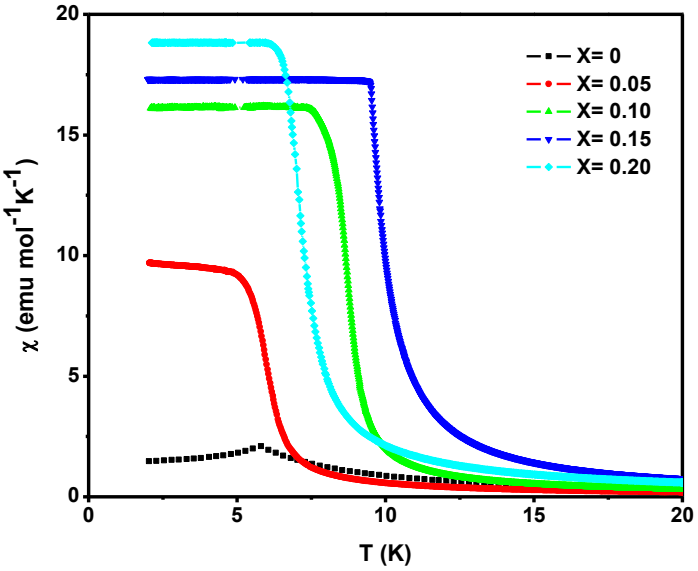

Figure 4.1: Thermal variation of zero-field-cooled susceptibility measured at 50 Oe for $EuTi_{1-x}Nb_xO_3$ ($x = 0 - 0.20$) single crystals.

4.4 Synthesis of $EuTiNbO_3$

$EuTiNbO_3$ crystals were grown in collaboration with Susmita Roy and Prabhat Mandal. The polycrystalline $EuTi_{1-x}Nb_xO_3$ (x=0.15) powder samples were prepared by the conventional solid-state reaction method using high-purity Eu_2O_3, Nb_2O_5, and TiO_2. To remove any adsorbed CO_2 and H_2O, the rare earth oxide Eu_2O_3 was heated at 900°C for overnight before using it. The stoichiometric mixture of the above mentioned ingredients were heated at 1000-1100 °C for few days in the reduced atmosphere of 5% H_2 and 95% Ar, with intermediate grindings. Then, the obtained polycrystalline powder was reground

and pressed into two cylindrical feed and seed rods under hydrostatic pressure. These two rods were finally sintered at 1100 °C in the same environment for 24 hours. The single crystal of $EuTi_{1-x}Nb_xO_3$ (x= 0.15) were grown under the same reduced atmosphere using a 4-mirror float zone image furnace FZ-T-10000-H-VPM (Crystal System Co.). Over the entire crystal growth, the feed and seed rods were oppositely rotated at a speed 25 rpm and the typical growth rate was 5 mm/hr. The phase purity of $EuTiNbO_3$ was checked by the powder XRD method with CuK_α radiation (λ=1.5406 Å) in a high resolution Rigaku diffractometer (TTRAX III) at room temperature. No impurity peak has been found within the resolution of XRD which confirms the single phase nature of the compound. All the peaks in XRD were assigned to cubic structure of space group Pm3m by the Reitveld method using FULLPROF. The estimated lattice parameters $a = b = c = 3.929$ Å are very close to that reported earlier. The temperature and field dependence of the dc magnetization measurements were carried out in a SQUID-VSM. Now, I will discuss about transport spin polarization measurement of $EuTiNbO_3$.

4.5 "Transport" spin polarization measurement:

As we have discussed in chapter 1, point contact Andreev reflection spectroscopy can be used to find the spin polarization of a ferromagnet by making mesoscopic point-contact by using a sharp tip of a conventional superconductor [48, 119–126]. The present work deals with spin-resolved Andreev reflection spectroscopy on $EuTi_{1-x}Nb_xO_3$ (x = 0.15). The low T_c of this material enables us to extract the transport spin polarization all the way up to T_c from PCAR using Nb, a conventional superconductor with T_c of 9.2 K. As we discussed previously, this technique relies on the fact that the process of Andreev reflection, through which an electron incident on a normal metal/superconductor (N/S) interface with energy less than the superconducting energy gap (Δ) gets reflected back as a hole in the opposite spin band of the metal, is strongly suppressed when the normal metal electrode is a ferromagnet.

Spin polarizaton in a metallic ferromagnet is defined as P = ($N_\uparrow(E_F)$-$N_\downarrow(E_F)$)/($N_\uparrow(E_F)$

+$N_{\downarrow}(E_F)$), where $N_{\uparrow}(E_F)$ and $N_{\downarrow}(E_F)$ are the density of states of the up and down spin channels respectively at the Fermi level. However, in a transport experiment like PCAR, the relevant quantity is not the absolute spin polarization but the so called "transport spin polarization" which is defined as: P_t = ($\langle\ N_{\uparrow}\ v_{F\uparrow}\ \rangle_{FS}$ - $\langle\ N_{\downarrow}\ v_{F\downarrow}\ \rangle_{FS}$)/($\langle\ N_{\uparrow}\ v_{F\uparrow}\ \rangle_{FS}$ + $\langle\ N_{\downarrow}\ v_{F\downarrow}\ \rangle_{FS}$), where $N_{\uparrow}$ and $N_{\downarrow}$ are the density of states (DOS) of the up and down spin channels respectively at the Fermi level and $v_{F\uparrow}$ and $v_{F\downarrow}$ are the respective Fermi velocities [127].

The transport spin-polarization is estimated from the analysis of the differential conductance versus voltage (V) characteristics of a ballistic or diffusive point contact established between a superconducting tip and the ferromagnet. Blonder-Tinkham-Klapwijk (BTK) model is used to analyze the spin-polarized Andreev reflection spectra [44, 128, 129] obtained between a ferromagnetic material and a superconductor by using four fitting parameters Z, Δ, Γ and P_t. The symbols Z, Δ, Γ and P_t denote the dimensionless interfacial barrier strength as in BTK theory, superconducting gap amplitude, energy scale associated with finite quasi-particle lifetime and percentage transport spin-polarization respectively. While keeping in mind that for the measurement of the spin polarization of ferromagnets usually standard conventional superconducting probes are used, for which the value of Δ is known, we have chosen Nb tip to measure the spin polarization of $EuTiNbO_3$. Thus we need to tune rest of the parameters except Δ during the analysis of spin-polarized Andreev reflection spectra.

4.6 Experimental details

To measure the spin-polarization of $EuTi_{0.85}Nb_{0.15}O_3$, we performed PCAR spectroscopy meaurements on material using Nb(conventional superconductor) tips. A differential screw based head assembly was used to make and control the point contact between the sample and Nb tip in ballistic region (as discussed in chapter 2). We measured differential conductance dI/dV vs. V curve for different contacts with different values of Z, Δ, Γ, P_t for ballistic point contacts. The experimental data were fitted with modified BTK model

for the finite spin polarization of the material. The theoretical fits are exactly lying on the experimental curves. The BTK model includes the parameter spin polarization (P) which gives the value of spin polarization in the point-contact geometry at a certain barrier Z. In Figure 4.2, we show the representative Andreev reflection spectra obtained on single

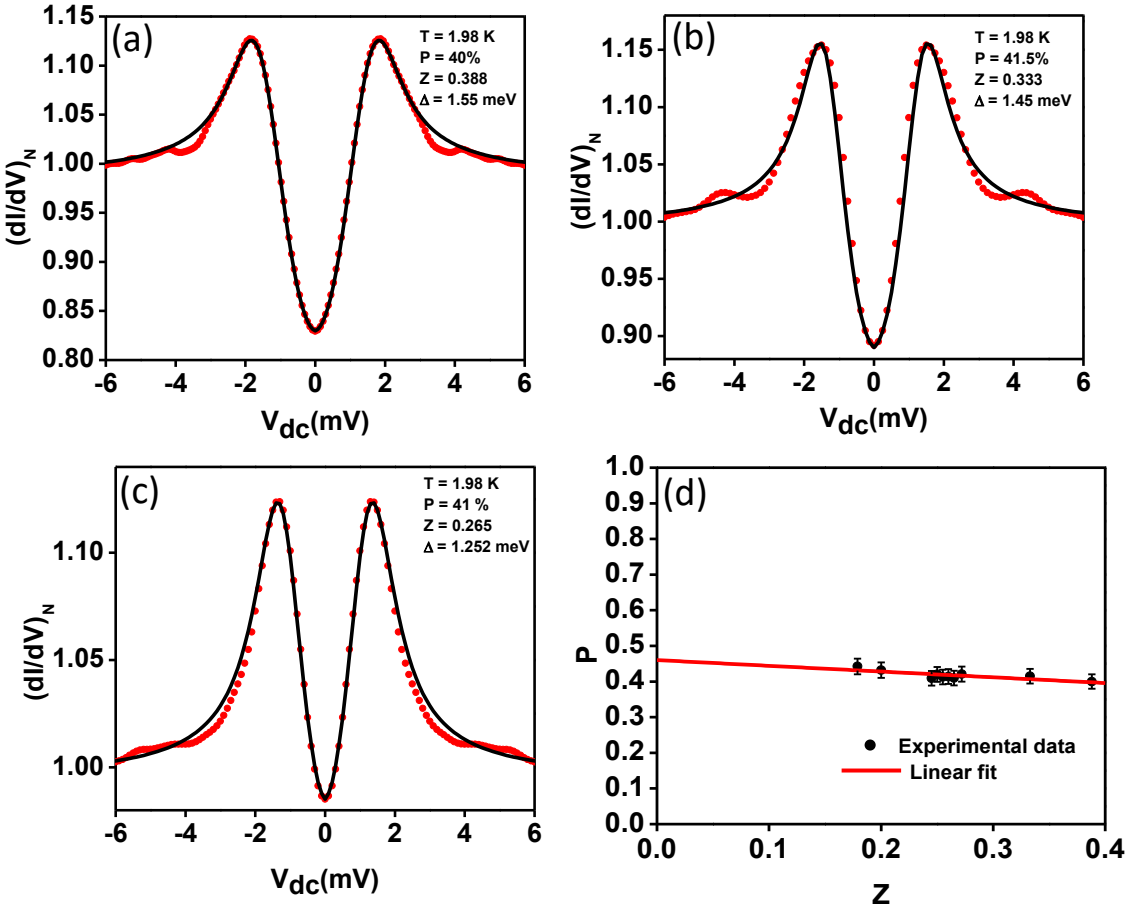

Figure 4.2: (a),(b),(c) Normalized dI/dV spectra for point contacts on $EuTi_{1-x}Nb_xO_3$ with x=0.15 using a Nb tip. The black lines show BTK fits with spin-polarization included. (d) Spin-polarization (P) vs. barrier strength (Z) plot. The solid lines show extrapolation to Z = 0 where the spin-polarization approaches 45 %

crystal $EuTi_{0.85}Nb_{0.15}O_3$. It can be clearly seen that the zero-bias conductance is low and two peaks are symmetric about V = 0 appear due to Andreev Reflection. As we have discussed in chapter 1, this suppression arises due to the spin polarization of the transport current [48, 58]. The superconducting gap Δ ranges between 1.2-1.5 meV for different contacts. Thus, the analysis involved three freely varying fitting parameters – P_t, Z and Γ. Δ is known for a standard superconductor, which varies a bit from the standard bulk value and is more or less same for most of the point contacts. The extracted values of

spin-polarization P_t and Γ are also shown. For different values of Z between 0.265-0.388 the transport spin polarization is measured to be around 41%.

While analyzing the PCAR spectrum, we should keep one thing in our mind, if the Z of the point-contact is large, the spin-flip scattering starts at the interface. Therefore, the spin polarization measured for a finite Z is less than the intrinsic spin polarization (Z = 0 for intrinsic spin plarization). So, to find intrinsic transport spin polarization by PCAR technique, we record a large number of spectra for different point-contacts. Thus, there will be a statistical distribution of the Z values for these contacts $i.e.$, some of the contacts will have very high Z while some will have very small Z. All the point contacts are analyzed and extracted value of the transport spin polarization P_t is plotted against the Z. The extracted value of P_t is seen to decrease with increasing Z, as expected. It depends linearly on Z as shown in Figure 4.2(d) . This curve is extrapolated to Z = 0 to obtain the intrinsic transport spin polarization. The solid line in Figure 4.2(d) shows linear extrapolation of the Z-dependence of P_t to Z = 0 which gives the expected intrinsic value of the spin-polarization (for Z = 0). The intrinsic spin-polarization extracted in this case is found to be 45% which is comparable to elemental ferromagnetic metals like Fe(P = 40%), Co(P = 42%) and Ni(P = 39%) [48].

Figure 4.3(top) shows temperature dependence of normalized dI/dV spectra for point-contacts on $EuTi_{0.85}Nb_{0.15}O_3$. The dip at V = 0 in the spectra is maximum at the lowest observed temperature of 1.98 K. With increase in temperature, the differential conductance spectra gradually undergo thermal smearing. The two peaks in the conductance spectra associated with the superconducting energy gap, the most dominant feature of the spectra, gets flattened at temperatures greater than 8.34 K. The BTK fits of the temperature dependence of normalized dI/dV spectra (solid line in Figure 4.3(top)) give an estimate of temperature dependence of the measured transport spin-polarization P_t and also the broadening parameter Γ as shown in Figure 4.3(bottom).

Transport spin-polarization decreases with increase in temperature whereas the parameter Γ is observed to increase with temperature. Γ gradually increases and reaches a

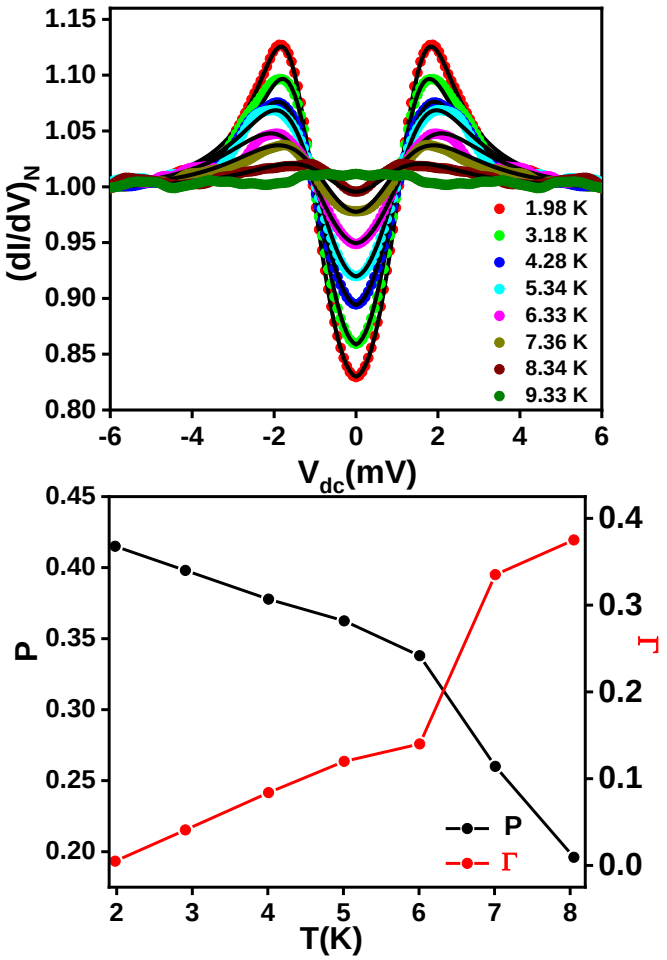

Figure 4.3: (top) Normalized dI/dV spectra with varying temperature over a temperature range of 1.98 K to 9.33 K for point contacts on $EuTi_{0.85}Nb_{0.15}O_3$ using a Nb tip. The colored lines show experimental data points and the black lines show BTK fits with spin-polarization included. (bottom) Temperature dependence of transport spin-polarization and the broadening parameter Γ. The solid lines are guide to the eye.

maximum value of 0.4 meV at 8 K close to the T_c of $EuTi_{0.85}Nb_{0.15}O_3$. The parameter Γ is associated with lifetime (τ) of superconducting quasiparticle in the way $\Gamma = \hbar/\tau$. The increase in Γ with temperature signifies a corresponding decrease in quasiparticle lifetime which might be due to enhanced spin fluctuations at higher temperatures. Figure 4.4(top) shows temperature dependence of transport spin-polarization and spontaneous magnetization in the same panel for a direct comparison between the two. P_t is observed to decrease with temperature following the same behaviour as M_s. This is clearly seen in Figure 4.4(bottom) where M_s and P_t are seen to linearly dependent on each other. Thus, the temperature dependence of spin polarization shows similar dependence as the temperature dependence of spontaneous magnetization as is expected for a ferromagnetic

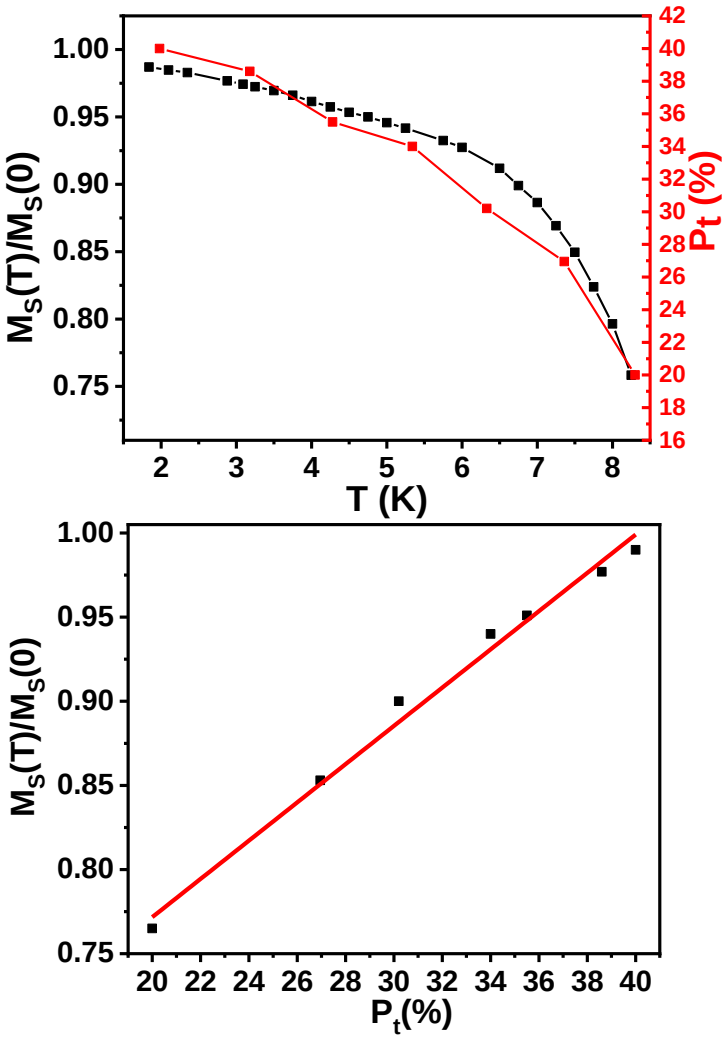

Figure 4.4: Temperature dependence of transport spin-polarization (P_t) and spontaneous magnetization M_S(T) normalized by that at T=0 K,in the temperature range 2 - 9 K. (bottom) shows variation of normalized magnetization with transport spin-polarization. The solid lines are guide to the eye.

system. This is remarkable because such proportional dependence of P_t and M_s with temperature is expected only for materials with strictly parabolic bands and $EuTi_{0.85}Nb_{0.15}O_3$ is known to be a system with large correlation effects.

4.7 Conclusion

From the analysis of the Andreev reflection data between the superconductor and the ferromagnet, we found the evidence of a high degree of transport spin-polarization approaching 45% in $EuTi_{0.85}Nb_{0.15}O_3$. For regular ferromagnetic compounds the spin polarization is of the same order as found in $EuTiNbO_3$. It should be noted here that ferromagnets with transport spin-polarization approaching 50% are potential candidates as spin source

in spintronic devices. However, as it has been discussed that $EuTiNbO_3$ is possibly a complex material with strong correlations. The key aspect of this chapter is not only the measurement of the transport spin polarization in $EuTiNbO_3$ but also to show how generically the spin polarization evolves with temperature proportionately with the bulk magnetization even for a complex material with strong correlations. To note, such a proportional dependence is trivial for strictly parabolic bands without correlations. In that respect, the understanding that is derived from our results is of course useful for employing novel materials in variable temperature spintronic applications.

5 Evolution of spin polarization in Bi_2Se_3 with Mn doping

As it was discussed in section 1.3 that three-dimensional topological insulators (TIs) experience an unconventional electronic phase driven by strong spin-orbit interaction (SOI): "Bulk band inversion" occurs as a result of strong spin orbit coupling. The striking feature of these heavy-element materials is the emergence of conducting surface states comprising of massless Dirac fermions on their surface [26, 29, 130–132]. These surface states are characterized by an intrinsic spin helicity: the wave vector of the electron determines its spin state (spin-momentum locking). A net spin density is thus produced upon driving a charge current at the surface of a TI $i.e.$ this spin momentum locking leads to a large transport spin-polarization of the surface states [127, 133, 134]. Thus, Spin-momentum locked topological surface states provide exotic properties for spintronics applications. These surface states are also protected by time reversal symmetry. If the time reversal symmetry (Topological protection of the system) is either broken by applying an external magnetic field or by doping the topological insulator with dopants in a controlled fashion, it may be possible to control the transport spin-polarization of the surface states. From theoretical calculations it is also known that magnetic dopants can lead to opening of a gap at the Dirac point in 3D TIs and with such doping, the TIs may exhibit ferromagnetic order with perpendicular magnetic anisotropy facilitated by Ruderman-Kittel-KasuyaYosida (RKKY) exchange [133–139]. Ferromagnetism in TIs may lead to wider variety of exotic physical phenomena, such as the anomalous quantum Hall effect and magneto-electric effects [140, 141]. The quest for efficient generation and control of spin has motivated the search for such materials. A_2B_3 type chalcogenides like Bi_2Se_3 is a well known topological insulator having a very large magnitude of spin-polarization. On doping Bi_2Se_3 with Mn dopants, time reversal symmetry of topological surface states, is broken and effective spin-polarization of the material is reduced. This is accompanied by an increasing ferromagnetic order of the crystals with Mn doping. The suppression

in spin polarization with magnetic doping can be attributed to a competition between the spin polarization originating from the spin momentum locked surface states, which is lowered in the doped system and the emerging magnetization of the system that increases with doping. In this chapter, I will present scanning tunnelling spectroscopy and spin polarized Andreev reflection spectroscopy and show how we can tune spin-polarization in a topological insulator by lowering the spin momentum locked surface states and enhancing the emerged magnetization with magnetic doping. The experiments, using scanning tunneling microscope were done in collaboration with Anshu Sirohi and Shekhar Das. Before going into detailed discussion of spin-polarization of Mn doped Bi_2Se_3, we will first check the crystal quality. The synthesis of Mn doped Bi_2Se_3 was done in collaboration with Vishal K. Maurya and Satyabrata Patnaik.

5.1 Crystal quality

First we confirmed the surface quality of the Bi_2Se_3 crystals using a low temperature and ultra-high-vacuum scanning tunneling microscope (STM) working down to 300 mK. The crystals $Mn_xBi_{2-x}Se_3$ ($x = 0, 0.03, 0.05, 0.1$) were cleaved $in-situ$ at 80 K under ultrahigh vacuum (10^{-11} mbar) and Low Energy Electron Diffraction(LEED) was carried out on the crystals $in-situ$. All the crystals show hexagonal LEED pattern(Figure 5.1). Also long range ordering of atoms in the crystals remains unaltered with x. High quality of single crystals can be seen in LEED pattern. There are no extra features present due to any other impurities or clusters in the LEED patterns. The absence of any other impurity phase was also confirmed by XRD analysis.

After confirming the high quality of the crystals, they were then transferred to the STM measurement head kept at low temperatures (Unisoku system with RHK R9 controller, working down to 300 mK). Figure 5.2 (left) is a large area STM image of the Bi_2Se_3 surface at 17 K, which shows clover shaped or triangular defects. The triangular defects are randomly distributed throughout the crystal surface. Figure 5.2 (bottom right) shows the enlarged view of one such triangular defect state. The triangular defects are known to

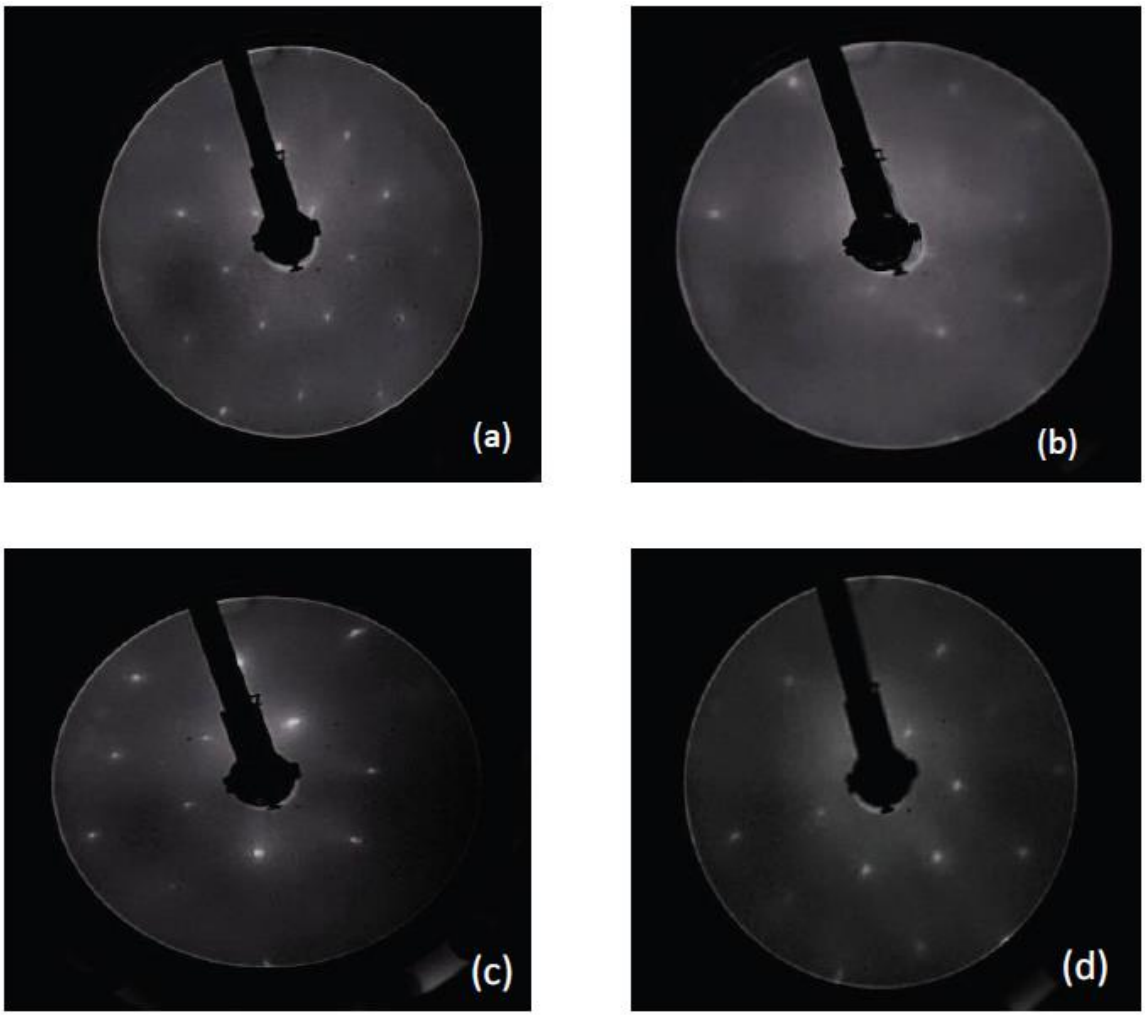

Figure 5.1: LEED pattern of $Mn_xBi_{2-x}Se_3$, (a) $x=0$, (b) $x=0.03$, (c) $x=0.05$ and (d) $x=0.1$ show hexagonal lattice structure.

be associated with Se vacancy in the binary selenide family of materials [142,143]. Figure 5.2 (top right) shows the zoomed in view of a small defect free area in the undoped Bi_2Se_3 sample taken at 17 K exhibiting periodic arrangement of atoms. Small area scans resolved atoms. After confirming the pristine nature of the surface of crystals, we performed local scanning tunneling spectroscopy (STS) at several points on the surface of the crystals using STM tip. Before discussing the STS spectra, we will first discuss about the magnetic characterization of Mn doped Bi_2Se_3.

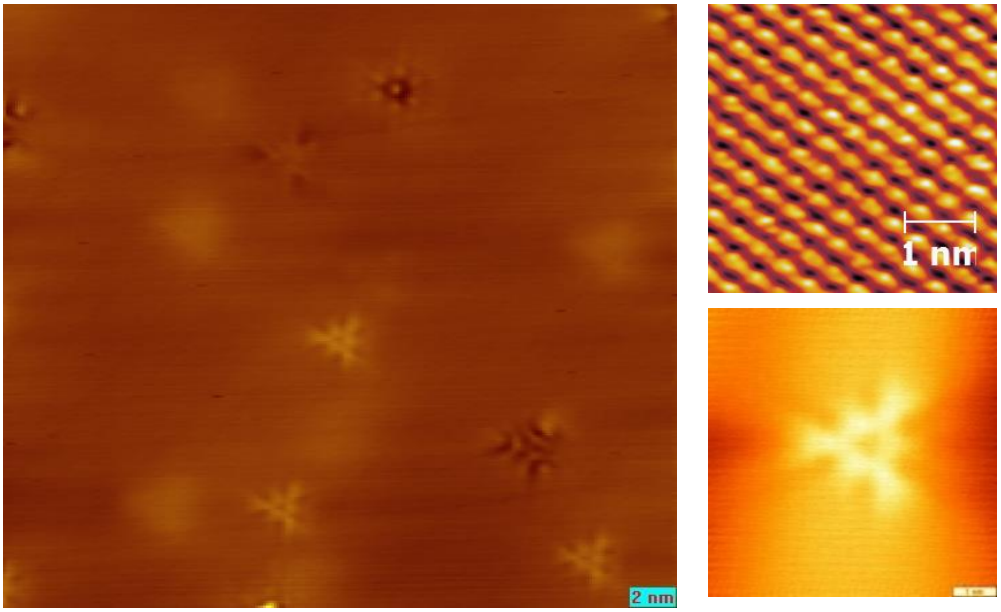

Figure 5.2: (left) Image of Bi_2Se_3 surface captured at 17 K where clover shaped/triangular defects are visible. (top right) Atomic resolution image of the cleaved surface of Bi_2Se_3. (bottom right) shows an enlarged view of one defect state.

5.2 Magnetic characterization of Mn doped Bi_2Se_3

Till now we intended to look at the crystal quality and surface quality of Bi_2Se_3 crystal. Now we will discuss Hall effect studies and what will be the effect of doping Mn in Bi_2Se_3 on its magnetic behaviour. In recent times various studies involving characterization of Mn doped $Bi_{2-x}Se_3$ have been carried out [144–146]. Hall effect studies showed that while the slope of Hall voltage is negative for undoped and 3% doped crystals, it changes to positive for higher dopings of Mn [147]. This was attributed to a change in carrier type (from n-type to p-type).

Further magnetization measurements on $Mn_xBi_{2-x}Se_3$ exhibit emergence of ferromagnetic character with Mn doping [147]. Figure 5.3 shows that no hysteresis loop has been observed for 3 % Mn doping, while a hysteresis loop can be clearly seen for 10 % Mn doped Bi_2Se_3 crystals. Thus on doping Mn in Bi_2Se_3, emergence of magnetism at $x = 0.03$ or higher is found, which is interesting in a system having strong spin-orbit coupling induced topologically ordered surface states.

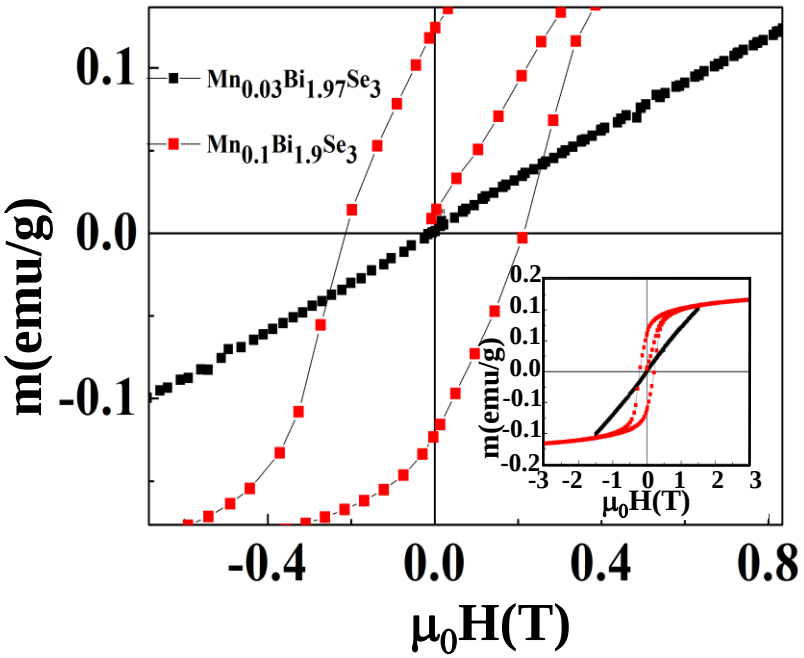

Figure 5.3: Magnetic field-dependent magnetization of crystals for $Mn_xBi_{2-x}Se_3$ ($x = 0.03$ and 0.1). The M-H curve is linear for $x = 0.03$ but for $x = 0.1$, the hysteresis loop opens up. Inset shows the complete cycle of the loop. Figure ref [147]

5.3 Disappearance of "V-shape" spectral feature

After looking at the magnetic characterization of Mn doped Bi_2Se_3, we performed local scanning tunneling spectroscopy (STS) on the surface of undoped and Mn doped Bi_2Se_3 crystals using STM tip.

A Dirac cone can be clearly seen in STS spectrum on Bi_2Se_3 in Figure 5.4(a). The Dirac point is at -100 meV i.e. 100 meV below the Fermi energy. Mn doping in the Bi_2Se_3 resulted in the disappearance of the "V-shape" spectral feature and a gap like spectrum is originated with the top of the valence band at -400 meV and bottom of the conduction band at 200 meV (Figure 5.4(b)). This gap opening indicates a gradual suppression of topological protection. This gap has been observed to exist over a larger span of energy with increasing Mn doping (Figure 5.4(c)). The large bulk band gap opening and disappearance of "V-shape" spectral feature suggests semiconducting behavior for all Mn doped samples. According to earlier reports, temperature dependence of resistivity for Mn doped Bi_2Se_3 exhibited semi-metallic behaviour. Nevertheless, this kind of resistivity behavior is commonly expected in doped semiconductors [147]. One of the possible

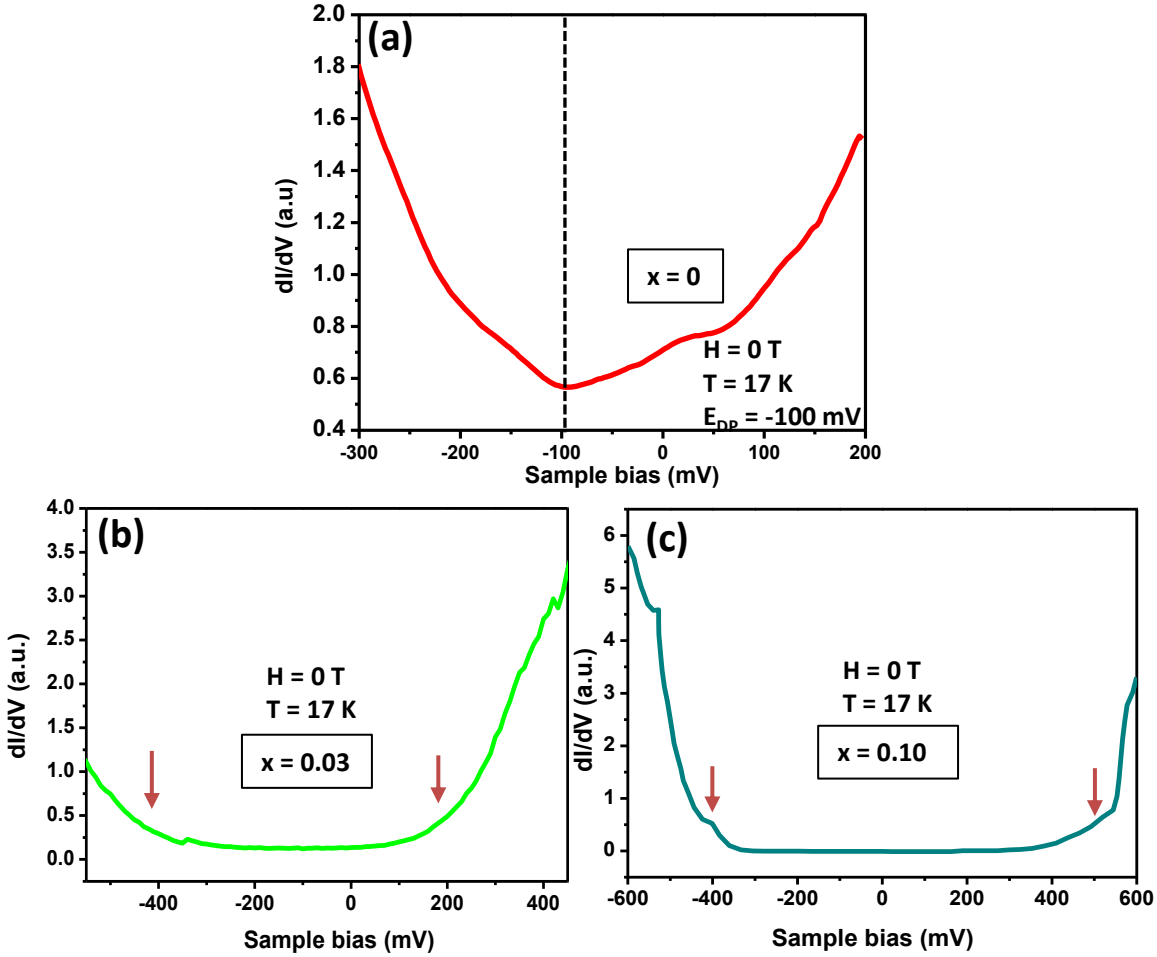

Figure 5.4: (a) A differential conductance spectrum measured by STS at 17 K. The Dirac point is at -100 mV. STS conductance spectrum for the $Mn_xBi_{2-x}Se_3$ sample with (b) $x = 0.03$ and (c) $x = 0.10$. The arrows indicate the bottom of conduction band (right) and the top of valence band (left), respectively.

reasons of disappearance of "V-shape" spectral feature can be attributed to destruction of topological protection due to enhanched contribution of the bulk Mn with doping. Furthermore, enhanced contribution from the bulk may also lead to opening of gap in STS spectra.

5.4 Spin polarization in Bi_2Se_3

In the previous chapter, we discussed that point contact Andreev reflection(PCAR) spectroscopy can be used to measure the spin polarization in a ferromgnetic compound [48–50]. Recently it was shown PCAR spectroscopy can also be used to find the spin polarization in topological insulators [52, 148]. Here also we are going to employ PCAR spectroscopy to detect spin-polarization in a topological insulator (Bi_2Se_3), which emerges

owing to the spin momentum locking [52]. In a transport experiment like PCAR, the relevant quantity is not the absolute spin polarization but the so called "transport spin polarization" which is defined as: $P_t = (\langle N_\uparrow v_{F\uparrow}\rangle_{FS} - \langle N_\downarrow v_{F\downarrow}\rangle_{FS})/(\langle N_\uparrow v_{F\uparrow}\rangle_{FS} + \langle N_\downarrow v_{F\downarrow}\rangle_{FS})$, where $N_\uparrow$ and $N_\downarrow$ are the density of states (DOS) of the up and down spin channels respectively at the Fermi level and $v_{F\uparrow}$ and $v_{F\downarrow}$ are the respective Fermi velocities. The average is taken over the entire Fermi surface. Andreev reflection at an interface between a conventional superconductor and a topological material should be analyzed carefully as the coupling between the two phases may be complex because here the topological phase has a non-trivial spin texture unlike in ferromagnets where a well defined order parameter exists. The PCAR spectra on topological insulators were successfully analyzed by Borisov et al. using a modified Blonder-Tinkham-Klapwijk (BTK) model including the role of spin-polarization developed by Strijkers et. al., [128].

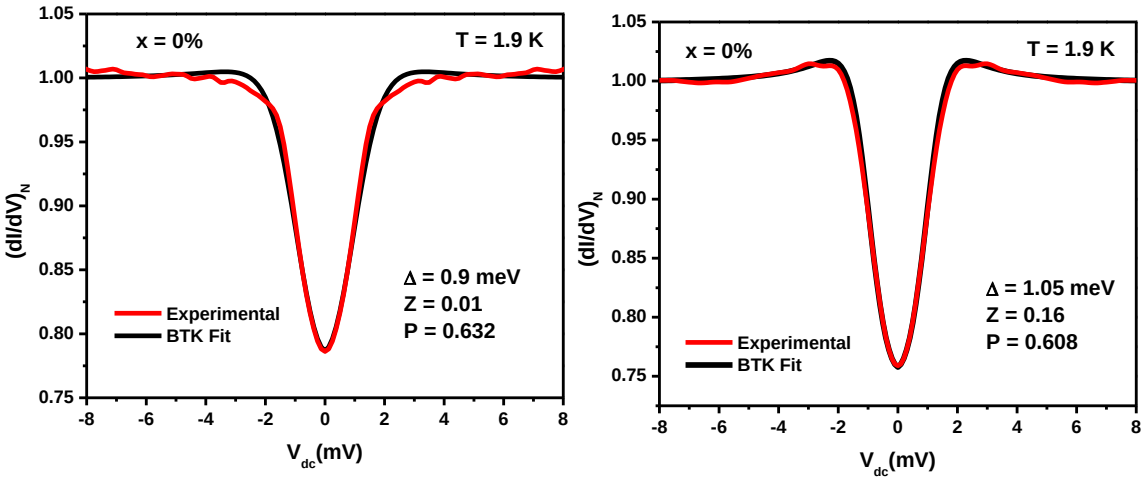

Figure 5.5: Normalized dI/dV spectra for point-contacts on $Mn_xBi_{2-x}Se_3$ with $x = 0$ using a Nb tip. The black lines show BTK fits with spin-polarization included.

Point-contact Andreev reflection spectroscopy measurements on Bi_2Se_3 crystals were performed using sharp tip of conventional superconductor Nb. The point-contacts between the sample and the tip were fabricated in ballistic regime, by moving the tip up and down by rotating a differential screw-based head assembly manually. The measurements involved to have the point contact spectra ($i.e.$ differential conductance dI/dV vs. V curves) for different contacts with different values of Z, the interface transparency as in the BTK theory [44, 56, 149, 150]. The spectra thus obtained were analyzed using BTK

theory modified to incorporate the effect of spin polarized bands [44,52,127,128]. In Figure 5.5 , we show two representative PCAR spectra (red points). The point-contact spectra show clear signatures of Andreev reflection. The overall spectral features indicate that the point contacts belong to the ballistic or diffusive regime of transport where the two peaks symmetric about V = 0 appear due to Andreev reflection across a superconducting interface with finite transparency (Z). A dip in the zero-bias conductance can be seen when junction impedance is in ballistic regime. The black lines show the fit to the experimentally obtained spectra using Blonder-Tinkham-Klapwijk (BTK) theory modified for the finite spin-polarization of the system following Strijkers et al.'s model [44, 128, 129]. The extracted values of spin polarization P and other parameters are also shown in the Figure 5.5. The superconducting gap Δ ranges between 0.7-1.5 meV for different contacts. For low values of Z, the spin polarization of undoped Bi_2Se_3 is measured to be almost 63%, which is consistent with theoretically expected value repoted in the past [151].

As we discussed in the previous chapter, while analyzing the PCAR spectrum, we should keep one thing in our mind, if the Z of the point-contact is large, the spin-flip scattering starts at the interface. Therefore, the spin polarization measured for a finite Z is less than the intrinsic spin polarization (Z = 0 for intrinsic spin plarization). So, to find intrinsic transport spin polarization by PCAR technique, we record a large number of spectra for different point-contacts. Thus, there will be a statistical distribution of the Z values for these contacts $i.e.$, some of the contacts will have very high Z while some will have very small Z. All the point contacts are analyzed and extracted value of the transport spin polarization P_t is plotted against the Z. The extracted value of P_t is seen to decrease with increasing Z, as expected. It depends linearly on Z as shown in Figure 5.9. This curve is extrapolated to Z = 0 to obtain the intrinsic transport spin polarization. The solid lines in Figure 5.9 show linear extrapolation of the Z-dependence of P to Z = 0. This gives the expected intrinsic value of the spin-polarization (for Z = 0). The intrinsic spin-polarization of undoped Bi_2Se_3 is found to be approximately 63% which is significantly large compared to some of the strong elemental ferromagnetic metals like Fe (P = 40%),

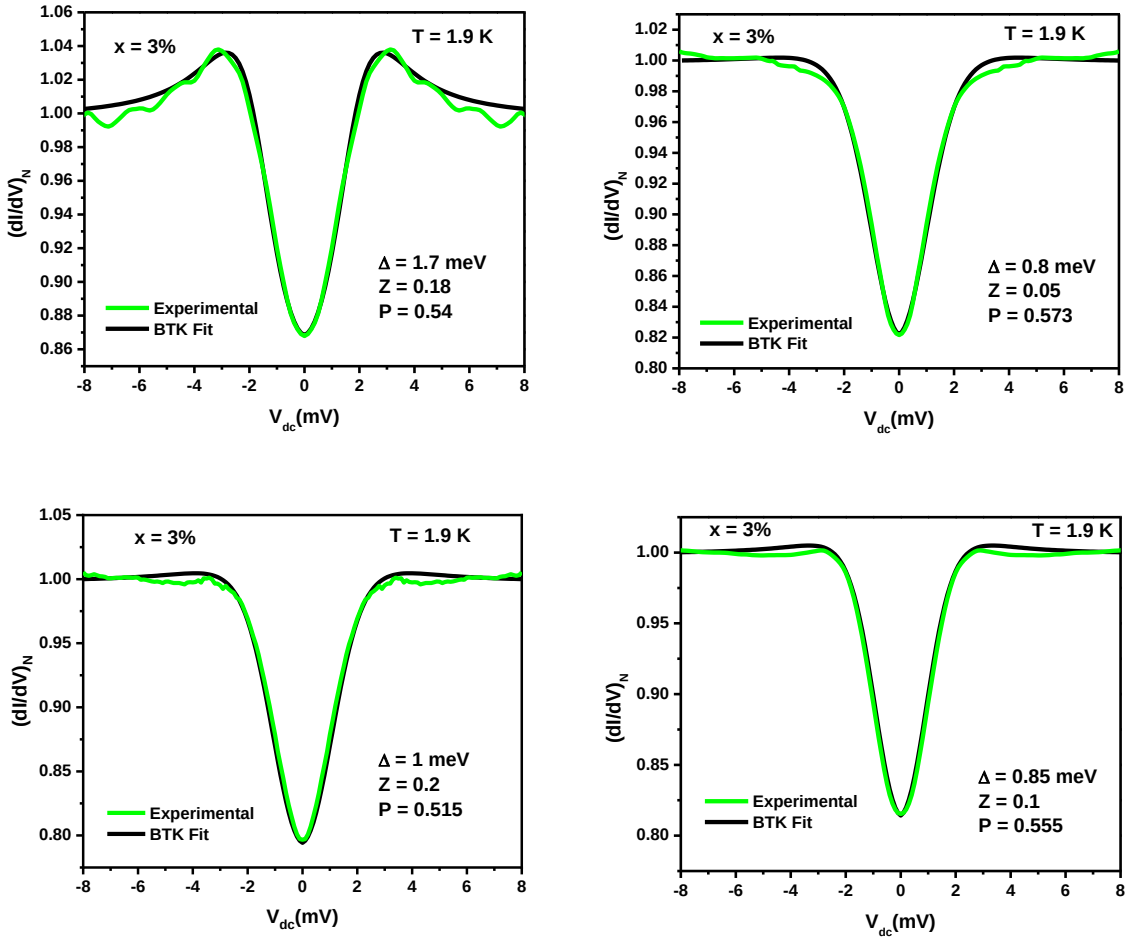

Figure 5.6: Normalized dI/dV spectra for point-contacts on $Mn_xBi_{2-x}Se_3$ with $x = 0.03$ using a Nb tip. The black lines show BTK fits with spin-polarization included.

Co (P = 42%) and Nickel (P = 39%) [48] and is comparable to the spin-plarization of other members of the binary chalcogenide family like Bi_2Te_3 where a spin polarization of 70% has been observed [52].

5.5 Spin polarization in Mn-doped Bi_2Se_3

The representative PCAR spectra obtained on $Mn_xBi_{2-x}Se_3$ crystals with x= 0.03, 0.05 and 0.1 doping are shown in Figure 5.6, 5.7 and 5.8 respectively.

The spin-polarization is approximately 58 % for x=0.03 Mn doping as shown in Figure 5.9. The transport spin-polarization is reduced to 51.9 % with increase of Mn doping to x=0.05 and further increase in doping results in suppression of transport spin-polarization to an approximate value of 48% (can be seen in Figure 5.9). Dependence of intrinsic spin-polarization on the concentration of magnetic doping (Mn) is shown in Figure 5.10.

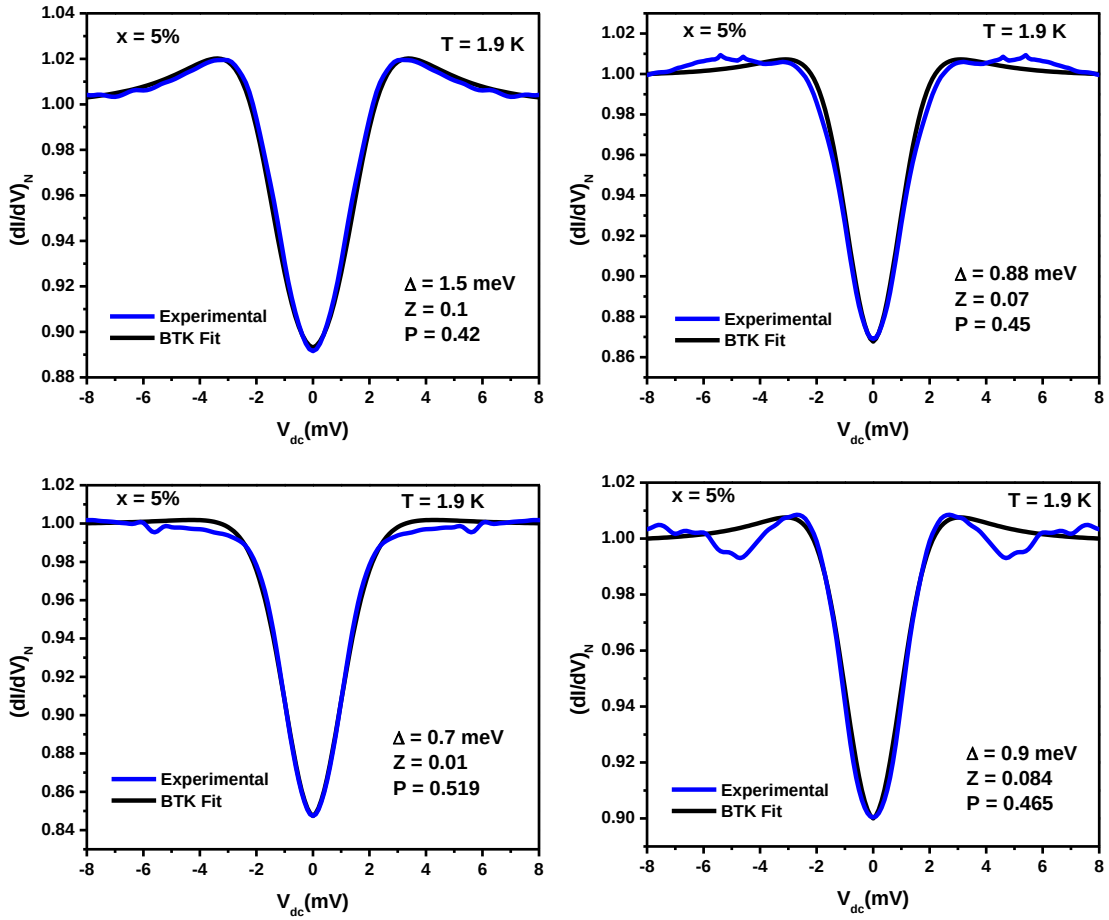

Figure 5.7: Normalized dI/dV spectra for point-contacts on $Mn_xBi_{2-x}Se_3$ with $x = 0.05$ using a Nb tip. The black lines show BTK fits with spin-polarization included.

With doping of magnetic atoms (Mn), as a ferromagnetic phase emerges, the topological protection of the system breaks down and the effective transport spin polarization at the surface decreases. With doping of Mn topological nature of the surface states get systematically suppressed possibly due to breakdown of time reversal symmetry. Therefore, doping causes reduction of transport spin polarization of the topological fraction of surface states. This is parallelly accompanied by increasing magnetization due to Mn doping leading to a competitive effect. Thus, this decrease in spin polarization with magnetic doping can be attributed to a competition between the spin polarization originating from the spin momentum locked surface states, which is lowered in the doped system and the emerging magnetization of the system that increases with doping.The resultant transport spin polarization is a net effect of two competing processes.

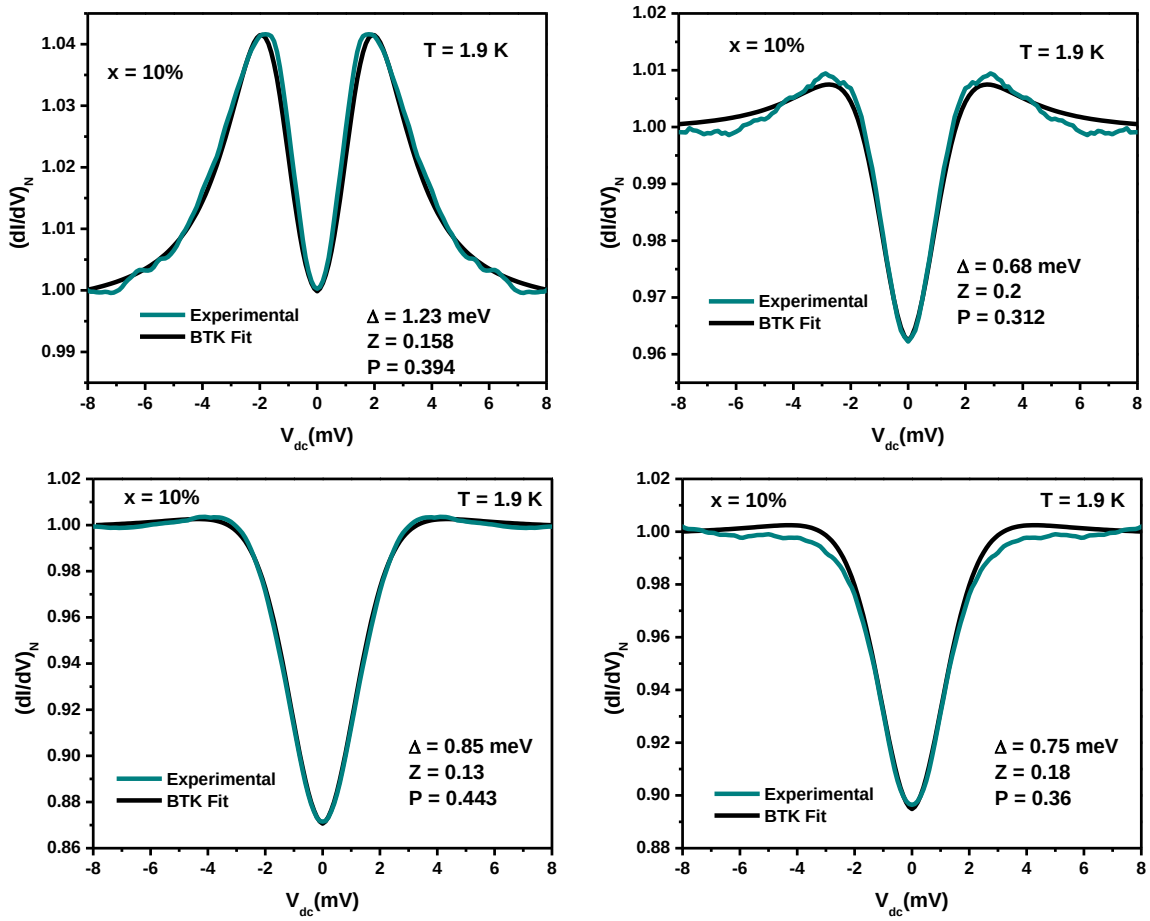

Figure 5.8: Normalized dI/dV spectra for point-contacts on $Mn_xBi_{2-x}Se_3$ with $x = 0.1$ using a Nb tip. The black lines show BTK fits with spin-polarization included.

5.6 Conclusion

In this chapter, we have presented scanning tunneling spectroscopy and spin-polarized PCAR spectroscopic studies on single crystals of $Mn_xBi_{2-x}Se_3$ ($x = 0, 0.03, 0.05, 0.1$) in order to probe the evolution of spin dependent transport properties of Bi_2Se_3 with incorporation of magnetic doping. The parent compound Bi_2Se_3 is found to exhibit a high transport spin-polarization of approximately 63 % whereas crystals with 10% Mn doping show transport spin polarization of about 48%. This reduction in transport spin-polarization can be attributed to the breakdown of time reversal symmetry in the doped system with emergence of ferromagnetism. The break down of time reversal symmetry in doped systems has been revealed in the STS measurements. In STS measurements, a Dirac cone with a Dirac point at - 100 mV (100 mV below the Fermi energy) in the differential conductance

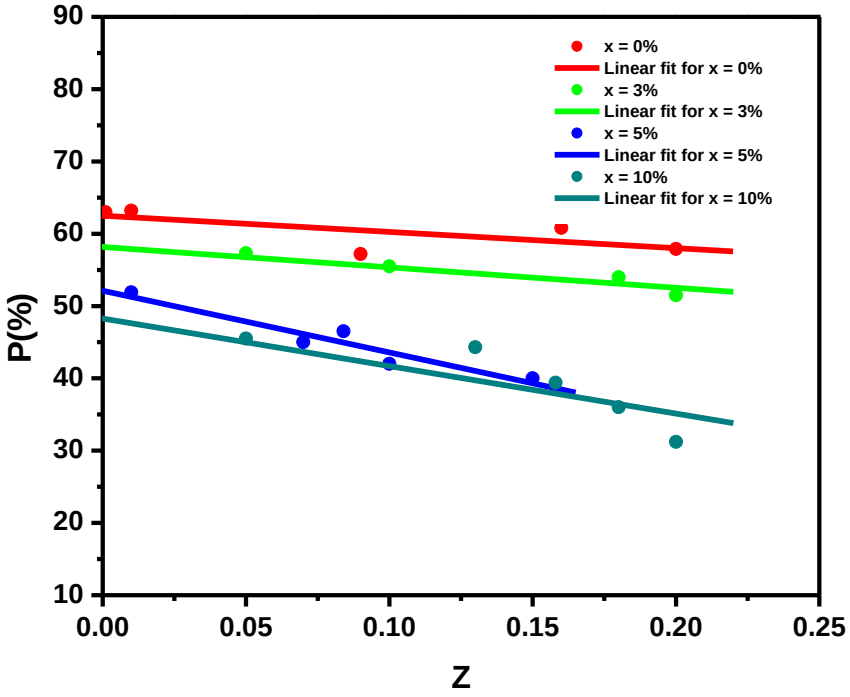

Figure 5.9: Spin-polarization (P) vs. barrier strength (Z) plot. The solid lines show extrapolation to Z = 0 where the spin-polarization approaches 63 % for the parent sample Bi_2Se_3 and gets suppressed in the doped samples $Mn_xBi_{2-x}Se_3$ ($x = 0.03, 0.05, 0.1$).

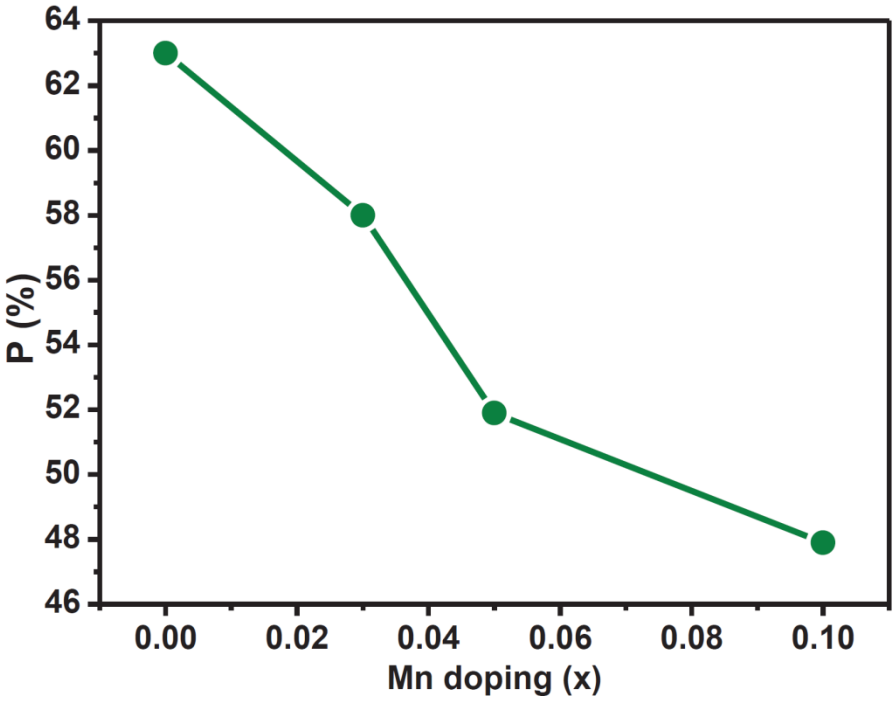

Figure 5.10: Change in intrinsic spin-polarization with change in Mn concentration (x), where $x = 0, 0.03, 0.05, 0.1$. The lines are guide to the eye.

(dI/dV *vs.* V) spectra in Bi_2Se_3 disappears and a semiconducting gap opens up on Mn doping in Bi_2Se_3. The resulting spin-polarization of 48% in 10% Mn doped Bi_2Se_3 is due

to the spin-polarization of the ferromagnetic phase after complete disappearance of the topological protection of the surface states. Extension of the current investigations using other magnetic dopants in this and various other families of topological insulators might lead to better understanding of the magnetically doped TIs for unlocking further novel quantum phenomena to pave the way for future applications for example, in spintronics and quantum computation.

5.7 Appendix

5.7.1 Temperature dependence

The temperature dependence of differential conductance spectra for Bi_2Se_3 are shown here. We have used the normal state (9.5 K) data to normalize the spectra.

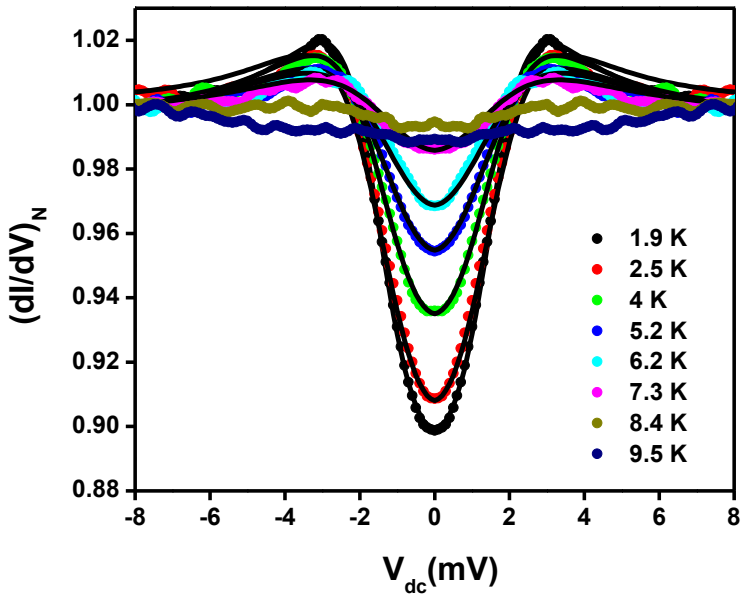

Figure 5.11: Temperature dependence of differential conductance spectra for Bi_2Se_3

From the temperature dependence, it was confirmed that the dI/dV spectra indeed exhibit signatures of Andreev reflection as all the spectral features disappear around 9.5 K which is the critical temperature of bulk niobium tip.

7 Summary

We explored some fundamental material properties of some novel quantum materials by using transport spectroscopy in tunneling regime and in metallic regime. I have employed scanning tunneling microscopy and point contact spectroscopy for transport spectroscopy in tunneling and metallic regime respectively. By using scanning tunneling microscope I showed experimental evidence of the emergence of a pseudo-magnetic field in a strained type-II Weyl semimetal Re-$MoTe_2$. I have shown clear oscillation of the density of states with energy due to the formation of Landau levels created by the strain-induced pseudo-magnetic field. The experiments as well as the theoretical analysis reveal the strength of the strain-induced pseudo-magnetic field to be $\sim 3T$.

Some part of the dissertation is devoted to point contact studies, with the help of which I measured spin-polarization of two novel quantum materials (i) a strongly correlated ferromagnet $EuTi_{1-x}Nb_xO_3$ (ii) a series of Mn doped topological insulators(Bi_2Se_3). I used our home made point contact system, to acquire the spectra using superconducting niobium tip in the ballistic transport regime. I showed, $EuTi_{1-x}Nb_xO_3$ possesses a high degree of transport spin-polarization approaching 45%. Also, I have shown that the spin polarization evolves with temperature proportionately with the bulk magnetization even for a complex material with strong correlations. In this respect, the understanding that is derived from our results is of course useful for employing novel materials in variable temperature spintronic applications.

For a series of Mn doped topological insulators(Bi_2Se_3), I showed that there is suppression of transport spin-polarization due to the breakdown of time reversal symmetry in the doped system with emergence of ferromagnetism. The break down of time reversal symmetry in doped systems has been revealed in the scanning tunneling spectroscopy measurements. Extension of such investigations might lead to better understanding of the magnetically doped TIs for unlocking further novel quantum phenomena to pave the way for future applications for example, in spintronics and quantum computation.

BIBLIOGRAPHY

[1] Joseph D. Martin, Physics Today **72**, 1-30 (2019).

[2] Dirac, P. A. M. Dirac, *Proceedings of the Royal Society A: Mathematical, Physical and Engineering Sciences*, **117** 778 (1928).

[3] H. Weyl, *Proc. Natl. Acad. Sci. U.S.A.* **15**, 323 (1929).

[4] H. Weyl, *I. Z. Phys.* **56**, 330 (1929).

[5] B. P. Palash, *American Journal of Physics* **79**, 485 (2011).

[6] Frank Wilczek, Nature Physics **5**, 618 (2009)

[7] X. Wan, A. M. Turner, A. Vishwanath, and S. Y. Savrasov, *Phys. Rev. B* **83**, 205101, (2011).

[8] M. V. Berry, *Aspects of Degeneracy (Springer US, Boston, MA)*, p. 123–140 (1985).

[9] Bohm-Jung Yang and Naoto Nagaosa *Nature Communications* **5**, 4898 (2014).

[10] T. Sato, et al. *Nat. Phys.* **7**, 840 (2011).

[11] J. A. Steinberg, et al. *Phys. Rev. Lett.* **112**, 036403 (2014).

[12] N. Levy, S. A. Burke, K. L. Meaker, M. Panlasigui, A. Zettl, F. Guinea, A. H. C. Castro Neto, and M. F. Crommie, *Science* **329**, 544 (2010).

[13] Neil W. Ashcroft and N. David Mermin, *Solid State Physics*, (1976).

[14] K. P. Klitzing, G. Dorda, and M. Pepper, *Phys. Rev. L* **46**, 6 (1980).

[15] K.V. Klitzing, *Philos. Trans. R. Soc. A*, **363**, 2211 (2005).

[16] M. I. D'yakonov and V. I. Perel', *JETP Lett.* **13**, 467 (1971).

[17] J. E. Hirsch, *Phys. Rev. Lett.* **83**, 1834 (1999).

[18] S. Zhang *Phys. Rev. Lett*. **85**, 393 (2000).

[19] S. Murakami, N. Nagaosa, and S. C. Zhang, *Science* **301**, 1948 (2003).

[20] J. Sinova, D. Culcer, Q. Niu, N. A. Sinitsyn, T. Jungwirth, and A. H. MacDonald, *Phys. Rev. Lett.* **92**, 126606 (2004)

[21] S. Murakami, *New Journal of Physics* **9**, 356 (2007).

[22] J. E. Moore and L. Balents, *Phys. Rev. B* **75**, 121306(R) (2007).

[23] L. Fu, C. L. Kane, and E. J. Mele, *Phys. Rev. Lett.* **98**, 106803 (2007).

[24] R. Roy, *Phys. Rev. B* **79**, 195322 (2009).

[25] L. Fu, C. L. Kane, *Phys. Rev. B* **76**, 045302 (2007).

[26] H. Zhang, C. -X. Liu, X. -L. Qi, X. Dai, Z. Fang, and S. -C. Zhang, *Nat. Phys.* **5**, 438–442 (2009).

[27] Y. Xia et al., *Nat. Phys.* **5**, 398 (2009).

[28] Y. L. Chen et al., *Science* **325**, 178 (2009).

[29] M. Z. Hasan and C. L. Kane, *Rev. Mod. Phys.* **82**, 3045, (2010)

[30] X.-L. Qi and S.-C. Zhang, *Rev. Mod. Phys.* **83**, 1057, (2011).

[31] D. J. Thouless, M. Kohmoto, M. P. Nightingale, and M. den Nijs, *Phys. Rev. Lett.* **49**, 405 (1982).

[32] Y. Ando, *Journal of the Physical Society of Japan*, **82**, 102001 (2013).

[33] Kramers, H. A., Proc. Amsterdam Acad. 33, 959 (1930).

[34] J. Stöhr and H. C. Siegmann, In Magnetism: From Fundamentals to Nanoscale Dynamics 1st edn, *Springer* **152**, 175–203 (2006).

[35] W.H. Wang, M. Przybylski, W. Kuch, L. I. Chelaru, J. Wang, Y. F. Lu, J. Barthel, H. Meyerheim and J. Kirschner, *Phys. Rev. B* **71**, 144416 (2005).

[36] K. Miyamoto, A. Kimura, Y. Miura, M. Shirai, M. Ye, Y. Cui, K. Shimada, H. Namatame, M. Taniguchi, Y. Takeda, Y. Saitoh, E. Ikenga, S. Ueda, K. Kobayashi, T. Kanomata, *Phys. Rev. B* **79**, 100405(R) 2009.

[37] S. Ouardi, G.H. Fecher, X. Kozina, G. Stryganyuk, B. Balke, C. Felser, E. Ikenga, T. Sugiyama, N. Kawamura, M. Suzuki, K. Kobayashi, *Phys. Rev. Lett.* **107** 036402 (2011).

[38] R. Meservey and P. M. Tedrow, *Phys. Rev. Lett.* **26**, 192 (1971).

[39] R. Meservey, P. M. Tedrow, *Phys. Rep.* **238**, 173 (1994).

[40] M. Julliere, *Phys. Lett. A* **54**, 225 (1975).

[41] A. Andreev, *Sov. Phys. JETP* **19**, 1228 (1964)

[42] A. Wexler, *Proc* **89**, 927 (1966).

[43] J. M. V. Ruitenbeek, Conductance quantisation in metallic point contacts, Springer Berlin Heidelberg (2000).

[44] G.E. Blonder, M.Tinkham, amd T.M. Klapwijk, *Phys. Rev. B* **25**, 4515 (1982).

[45] L. Janson, M. Klein, H. Lewis, A. Lucas, A. Marantan & K. Luna, *Am. J. Phys.* **80**, 133 (2012).

[46] I. Giacver, *Phys. Rev. Lett.* **5**, 147 (1960)

[47] M. Tinkham, Introduction to Superconductivity, McGrawhill (1996).

[48] R. J. Soulen et. al., *Science* **282**, 85 (1998).

[49] A. Sirohi, C. K. Singh, G. S. Thakur, P. Saha, S. Gayen, A. Gaurav, S. Jyotsna, Z. Haque, L. C. Gupta, M. Kabir, A. K. Ganguli, and G. Sheet, Appl. Phys. Lett. **108**, 242411 (2016).

[50] P. Raychaudhuri, A. P. Mackenzie, J. W. Reiner and M.R. Beasley, *Phys. Rev. B* **67**, 020411(R) (2003).

[51] G. T. Woods et al., *Phys. Rev. B* **70**, 054416 (2004).

[52] K. Borisov, C.-Z. Chang, J. S. Moodera, and P. Stamenov, *Phys. Rev. B* **94**, 094415 (2016).

[53] Yu. A. Bychkov and E. I. Rashba, *Sov. Phys. JETP Lett.* **39**, 78-81 (1984)

[54] G. Binnig, H. Rohrer, Ch. Gerbe, E. Weibe, *Physical Review Letters* **49** 57 (1982).

[55] Matthias Hunstig, *Actuators* 6 (2017).

[56] Yu. G. Naidyuk, I. K. Yanson, Point-contact Spectroscopy, Springer- Verlag New York (2005).

[57] A G M Jansen, A P van Gelder and P Wyder, Journal of Physics C: Solid State Physics 13, 33, (1980).

[58] S. K. Upadhyay et. al., *Phys. Rev. Lett.* **81**, 3247 (1998).

[59] Goutam Sheet, et. al., *Phys. Rev. B* **72**, 180407(R) (2005).

[60] A. G. M. Jansen, F. M. Mueller and P. Wyder, *Phys. Rev. B* **16**, 1325 (1977).

[61] P. N. Chubov, I. K. Yanson and A. I. Akimenko, *Sov. J. Low Temp. Phys.* **8**, 32 (1982).

[62] K. S. Ralls and R. A. Buhrman, *Phys. Lett.* **55**, (1989).

[63] B. Yan, and C. Felser, *Annu. Rev. Condens. Matter Phys.* **8**, 337-54 (2017).

[64] M. Z. Hasan, S. -Y. Xu, and G. Bian, *Phys. Scripta* **164**, 014001 (2015).

[65] X. Wan, A. M. Turner, A. Vishwanath, and S. Y. Savrasov, *Phys. Rev. B* **83**, 205101 (2011).

[66] A. A.Burkov, M. D. Hook,and L. Balents, *Phys. Rev. B* **84**, 235126 (2011).

[67] H. Weyl, *PNAS* **15**, 323-34 (1929).

[68] O. Vafek,and A. Vishwanath,*Annu. Rev. Condens. Matt. Phys.* **5**, 83-112 (2014).

[69] W. W. -Krempa, G. Chen, Y. B. Kim, and L. Balents, *Annu. Rev. Condens. Matt. Phys.* **5**, 57-82 (2014).

[70] S. -Y. Xu et. al., *Science* **349**, 613 (2015).

[71] S. Jia, S. -Y. Xu, and M. Z. Hasan, Weyl semimetals, *Nature Materials* **15**, 1140 (2016).

[72] J. Xiong, S. K. Kushwaha, T. Liang, J. W. Krizan, M. Hirschberger, W. Wang, R. J. Cava, and N. P. Ong, *Science* **350**, 413-416 (2015).

[73] P. Kim, J. H. Ryoo, and C. -H. Park, *Phys. Rev. Lett.* **119**, 266401 (2017).

[74] D. I. Pikulin, A. Chen, and M. Franz, *Phys. Rev. X* **6**, 041021 (2016).

[75] M. A. Zubkov, *Annals of Physics* **360**, 655-678 (2015).

[76] C. -X. Liu, P. Ye, and X. -L. Qi, *Phys. Rev. B* **87**, 235306 (2013).

[77] A. Cortijo, Y. Ferreirós, K. Landsteiner, and M. A. H. Vozmediano, *Phys. Rev. Lett.* **115**, 177202 (2015).

[78] A. Cortijo, D. Kharzeev, K. Landsteiner, and M. A. H. Vozmediano, *Phys. Rev. B* **94**, 241405(R) (2016).

[79] T. Liu, D. I. Pikulin, and M. Franz, *Phys. Rev. B* **95**, 041201(R) (2017).

[80] V. Arjona, and M. A. H. Vozmediano, *Phys. Rev. B* **97**, 201404(R) (2018).

[81] A. G. Grushin, J. W. F. Venderbos, A. Vishwanath, and R. Ilan, *Phys. Rev. X* **6**, 041046 (2016).

[82] H. Sumiyoshi, and S. F. Fujimoto, *Phys. Rev. Lett.* **116**, 166601 (2016).

[83] F. Guinea, M. I. Katsnelson, and A. K. Geim, *Nat. Phys.* **6** 30 (2010).

[84] Y. Okada, W. Zhou, D. Walkup, C. Dhital, S. D. Wilson, and V. Madhavan, *Nature Communications* **3**, 1158 (2012).

[85] S. Tchoumakov, M. Civelli, and M. O. Goerbig, *Phys. Rev. Lett.* **117**, 086402 (2016).

[86] Y. Sun, S. C. Wu, M. N. Ali, C. Felser, and B. Yan, *Phys. Rev. B* **92** 161107(R) (2015).

[87] Z. Guguchia et al., *Nature Communications* **8** 1082 (2017).

[88] R. Clarke, E. Marseglia, and H. P. Hughes, *Philosophical Magazine B* **38** 121-126 (1978).

[89] Z. Wang, D. Gresch, A. A. Soluyanov, W. Xie, S. Kushwaha, and X. Dai, *Phys. Rev. Lett.* **117**, 056805 (2016).

[90] L. Huang, T. M. McCormick, M. Ochi, Z., M. -to Suzuki Zhao, R. Arita, Y. Wu, D. Mou, H. Cao, J. Yan, N. Trivedi, and A. Kaminski, *arXiv:1603.06482v1* (2016).

[91] Y. Qi et al., *Nature Communications* **7** 11038 (2016).

[92] M. Mandal, S. Marik, K. P. Sajilesh, Arushi, D. Singh, J. Chakraborty, N. Ganguli, and R. P. Singh, *Phys. Rev. Materials* **2** 094201 (2018).

[93] P. O. Sukhachov, E.V. Gorbar, I. A. Shovkovy, and V. A. Miransky, *Ann. Phys. (Berlin)* **530**, 1800219 (2018).

[94] A. Cortijoa, and M. A. Zubkov, *Annals of Physics* **366**, 45-56 (2016).

[95] H. M. Guo, H. W. Liu, Y. L. Wang, H. J. Gao, H. X. Shang, Z. W. Liu, H. M. Xie, and F. I. Dai, *Nanotechnology* **15**, 991 (2004).

[96] P. Cheng et al., *Phys. Rev. Lett.* **105**, 076801 (2010).

[97] M. Jung et al., *Nano Lett.* **18** 1863 (2018).

[98] Z. Wang et al., *Phys. Rev. Lett.* **117**, 056805 (2016).

[99] D. Rhodes et al., *Phys. Rev. B* **96**, 165134 (2017).

[100] H. Shapourian, T. L. Hughes, and S. Ryu, *Phys. Rev. B* **92**, 165131 (2015).

[101] T. Liu, D. I. Pikulin, and M. Franz, *Phys. Rev. B* **95**, 041201(R) (2017).

[102] V. Lukose, R. Shankar, and G. Baskaran, *Phys. Rev. Lett.* **98**, 116802 (2007).

[103] I. M. Lifshitz, and A. M. Kosevich, *Sov. Phys. JETP* **2**, 636 (1956).

[104] I. M. Lifshitz, M. Ia. Azbel, M. I. Kaganov, *Sov. Phys. JETP* **4**, 41 (1957).

[105] I. Zutic, J. Fabian, and S. Das Sarma, Rev. Mod. Phys. **76**, 323 (2004).

[106] G. A. Prinz, Phys. Today **48**, 58 (1995).

[107] J. M. Daughton, A. V. Pohm, R. T. Fayfield, and C. H. Smith, J. Phys. D **32**, R169 (1999).

[108] S. Roy, N. Khan, and P. Mandal, *Phys. Rev. B* **98**, 134428 (2018).

[109] Z. Y. Zhao, O. Khosravani, M. Lee, L. Balicas, X. F. Sun, J. G. Cheng, J. Brooks, H. D. Zhou, and E. S. Choi, Phys. Rev.B **91**, 161106(R) (2015).

[110] G. Khaullin and S. Okamoto, Phys. rev. lett. **89**,167201 (2002).

[111] J.Hemberger, H.-A. Krug von Nidda, V. Fritsch, J. Deisenhofer, S. Lobina, T. Rudolf, P. Lunkenheimer, F. Lichtenberg, A.Loidl, D. Bruns, and B. Büchner, Phys. Rev. Lett. **91**, 066403 (2003).

[112] C. Ulrich, A. Gössling, M. Grüninger, M. Guennou, H. Roth,M. Cwik, T. Lorenz, G. Khaliullin, and B. Keimer,Phys. Rev.Lett. **97**,157401 (2006)

[113] T. Katsufuji and Y. Tokura,Phys.Rev.B **60**,R15021 (1999).

[114] T. Katsufuji and H. Takagi,Phys.Rev.B **64**,054415 (2001).

[115] K. S. Takahashi, M. Onoda, M. Kawasaki, N. Nagaosa, and Y.Tokura, Phys.Rev.Lett. **103**,057204 (2009).

[116] S. Roy, N. Khan, and P. Mandal,APL Mater.**4**,026102 (2016).

[117] L. Li, J. R. Morris, M. R. Koehler, Z. Dun, H. Zhou, J. Yan, D.Mandrus, and V. Keppens,Phys. Rev. B **92**,024109 (2015).

[118] L. Li, H. Zhou, J. Yan, D. Mandrus, and V. Keppens,APLMater. **2**,110701 (2014).

[119] S. Mukhopadhyay, P. Raychaudhuri, *Phys. Rev. B* **75**, 014504 (2007).

[120] Y. Ji, G. J. Strijkers, F. Y. Yang, C. L. Chien, J. M. Byers, A.Anguelouch, G. Xiao, and A. Gupta, Phys. Rev. Lett. **86**, 5585 (2001).

[121] J. M. Valentine and C. L. Chien, J. Appl. Phys. **99**, 08P902 (2006).

[122] L. Wang, K. Umemoto, R. M. Wentzcovitch, T. Y. Chen, C. L.Chien, J. G. Checkelsky, J. C. Eckert, E. D. Dahlberg, and C.Leighton, Phys. Rev. Lett. **94**, 056602 (2005).

[123] S. K. Clowes, Y. Miyoshi, Y. Bugoslavsky, W. R. Branford, C.Grigorescu, S. A. Manea, O. Monnereau, and L. F. Cohen, Phys.Rev. B **69**, 214425 (2004).

[124] R. Panguluri, G. Tsoi, B. Nadgorny, S. H. Chun, N. Samarth, andI. I. Mazin, Phys. Rev. B **68**, 201307(R) (2003).

[125] S. Singh, G. Sheet, P. Raychaudhuri, and S. K. Dhar, Appl. Phys.Lett. **88**, 022506 (2006).

[126] G. Sheet, H. Rosner, S. Wirth, A.Leithe-Jasper, W. Schnelle, U. Burkhardt, J. A. Mydosh, P. Ray-chaudhuri, and Y. Grin, Phys. Rev. B **72**, 180407 (R) (2005).

[127] I. I. Mazin,Phys. Rev. Lett. **83**, 1427 (1999).

[128] G. J. Strijkers, Y. Ji, F. Y. Yang, C. L. Chien, and J. M.Byers, Phys. Rev. B**63**, 104510 (2001).

[129] I. I. Mazin, A. A. Golubov, and B. Nadgorny, J. Appl. Phys. **89**, 7576 (2001).

[130] J. E. Moore, Nature **464**, 194-198, (2010).

[131] L. Fu, C. L. Kane, and E. J. Mele, Phys. Rev. Lett. **98**, 106803 (2007).

[132] D. Hsieh, Y. Xia, D. Qian, L. Wray, J. H. Dil, F. Meier, J. Osterwalder, L. Patthey, J. G. Checkelsky,N. P. Ong, A. V. Fedorov, H. Lin, A. Bansil, D. Grauer, Y. S. Hor, R. J. Cava, and M. Z. Hasan, Nature **460**, 1101–1105 (2009).

[133] J. -J. Zhu, D. -X. Yao, S. -C. Zhang, and K. Chang, Phys. Rev. Lett. **106**, 097201 (2011).

[134] A. A. Zyuzin and D. Loss , Phys. Rev. B **90**, 125443 (2014).

[135] R. R. Biswas and A. V. Balatsky, Phys. Rev. B **81**, 233405 (2010).

[136] Q. Liu, C. X. Liu, C. K. Xu, X. L. Qi, S. C. Zhang, Phys. Rev. Lett. **102**, 156603 (2009).

[137] Y. L. Chen, J.-H. Chu, J. G. Analytis, Z. K. Liu, K. Igarashi, H.-H. Kuo, X. L. Qi, S. K. Mo, R. G. Moore, D. H. Lu, M. Hashimoto, T. Sasagawa, S. C. Zhang, I. R. Fisher, Z. Hussain, Z. X. Shen, Science **329**, 659-662 (2010).

[138] F. Katmis, V. Lauter, F. S. Nogueira, B. A. Assaf, M. E. Jamer, P. Wei, B. Satpati, J. W. Freeland, I. Eremin, D. Heiman, P. J. -Herrero and J. S. Moodera, Nature **533**, 513–516 (2016).

[139] P. P. J. Haazen, J. B. Laloë, T. J. Nummy, H. J. M. Swagten, P. J. Herrero, D. Heiman, and J. S. Moodera, Appl. Phys. Lett. **100**, 082404 (2012).

[140] C. Z. Chang, J. Zhang, X. Feng, J. Shen, Z. Zhang, M. Guo, K. Li, Y. Ou, P. Wei, L. L. Wang, Z. Q. Ji, Y. Feng, S. Ji, X. Chen, J. Jia, X. Dai, Z. Fang, S. C. Zhang, K. He, Y. Wang, L. Lu, X. C. Ma, Q. K. Xue, Science **340**, 167-170 (2013).

[141] X. L. Qi, T. L. Hughes, and S. C. Zhang, Phys. Rev. B **78**, 195424 (2008).

[142] T. Hanaguri, K. Igarashi, M. Kawamura, H. Takagi, and T. Sasagawa, Phys. Rev. B **82**, 081305(R) (2010).

[143] P. Cheng, C. Song, T. Zhang, Y. Zhang, Y. Wang, J. -F. Jia, J. Wang, Y. Wang, B. -F. Zhu, X. Chen, X. Ma, K. He, L. Wang, X. Dai, Z. Fang, X. Xie, X. -L. Qi, C. -X. Liu, S. -C. Zhang, and Q. -K. Xue, Phys. Rev. Lett. **105**, 076801 (2010).

[144] A.S. Panfilov, G.E. Grechnev, A.V. Fedorchenko, K. Conder, and E.V. Pomjakushina, J. Phys.: Condens. Matter **27**, 456002 (2015).

[145] L. J. Collins-McIntyre, M. D. Watson, A. A. Baker, S. L. Zhang, A. I. Coldea, S. E. Harrison, A. Pushp, A. J. Kellock, S. S. P. Parkin, G. van der Laan, and T. Hesjedal, AIP Advances **4**, 127136 (2014).

[146] Y. D. Glinka, S. Babakiray, M.B. Holcomb, and D. Lederman, J. Phys.: Condens. Matter **28**, 165601 (2016).

[147] V.K. Maurya, C.L. Dong, C.L. Chen, K. Asokan, S. Patnaik, J. Magn. Magn. Mater. **456**, 1-5 (2018).

Jyotsna, Z. Haque, L. C. Gupta, M. Kabir, A. K. Ganguli, and G. Sheet, Appl. Phys. Lett. **108**, 242411 (2016).

[148] S. Das, A. Sirohi, G. K. Gupta, S. Kamboj, A. Vasdev, S. Gayen, P. Guptasarma, T. Das and G. Sheet, *Phys. Rev. B* **97**, 235306 (2018).

[149] G. Sheet , S. Mukhopadhyay , and P. Raychaudhuri , Phys. Rev. B **69**, 134507 (2004).

[150] L. Aggarwal, A. Gaurav, G. S. Thakur, Z. Haque, A. K. Ganguli, G. Sheet, Nature materials **15**, 32-37 (2016).

[151] O. V. Yazyev, J. E. Moore, and S. G. Louie, Phys. Rev. Lett. **105**, 266806 (2010)